DISSERTATION

ORIGINS AND IMPACTS OF TROPOPAUSE LAYER COOLING IN TROPICAL CYCLONES

Submitted by

Louis Rivoire

Department of Atmospheric Science

In partial fulfillment of the requirements

For the Degree of Doctor of Philosophy

Colorado State University

Fort Collins, Colorado

Spring 2020

Doctoral Committee:

Advisor: Thomas Birner
Co-Advisor: John A. Knaff

Michael M. Bell
Christopher A. Davis
Christian D. Kummerow
Subhas K. Venayagamoorthy

ABSTRACT

ORIGINS AND IMPACTS OF TROPOPAUSE LAYER COOLING IN TROPICAL CYCLONES

Remote sensing data from GPS radio occultation reveal temperatures lower than climatological average over a layer several kilometers deep near the tropopause above tropical cyclones (TCs). This signal, here referred to as tropopause layer cooling (TLC), occurs primarily during TC intensification and on spatial scales of the order of 1000 km. TLC has been hypothesized to be the result of:

1) Adiabatic expansion in cloud tops that overshoot the local level of neutral buoyancy.

2) Long wave radiative effects near the cloud top.

3) Adiabatic expansion in the TC secondary circulation.

The relative role of these mechanism has not been quantified yet, perhaps pertaining to the large uncertainties and relative lack of vertical resolution of observational data sets and numerical modeling studies near the tropopause. Given the complex relationships between the thermal structure of the upper troposphere and the TC secondary circulation, determining which mechanisms are at play is paramount. TLC is also expected to destabilize the upper troposphere to convection and allow clouds to reach higher altitudes, likely leading to subtle but consequential changes in the secondary circulation and associated latent heating vertical distribution. Low temperatures near the tropopause can lead to in situ formation of cirrus clouds, which impact the radiative budget in the tropical tropopause layer. Lastly, low temperatures above convective systems have been linked to dehydration of the stratosphere, prompting the question of the role of TCs on the climate.

Mechanism 1 is discussed in light of existing literature and suggested to be of marginal importance. Mechanisms 2 and 3 are examined using a combination of observational and theoretical analysis, and numerical modeling. Radiative heating rates calculated using cloud properties retrieved by the A-train suggest that mechanism 2 may explain up to half of TLC in the inner core,

but only marginal amounts of TLC at larger radii. While reanalysis data sets suggest that mechanism 3 may explain TLC, numerical simulations of TCs with higher resolution suggest that mechanism 3 does not act in a way consistent with the secondary circulation as is typically pictured, and may need to be revisited. Other mechanisms involving processes which violate gradient wind balance near the tropopause need to be formulated.

Finally, feedbacks between TLC, cloud structure, and TC dynamics are examined using parcel theory and idealized simulations. Parcel theory predicts that the TC thermal structure exerts a positive feedback on cloud top height during intensification, especially when convective entrainment is taken into account. While idealized simulations capture this general behavior, they exhibit other complex, transient behaviors which indicate breaking points in the interaction between clouds and their thermal environment.

ACKNOWLEDGEMENTS

This dissertation is the fruit of a five-year joint effort between my advisors, committee members, myself, and many others. I have had the immense privilege of working closely with Thomas Birner and John Knaff, two mentors who strike a powerful balance in their expertise, advising style, and personality. Thomas, John, I thank you for guiding my research while letting me discover my strengths and refine my interests over the years. I am especially grateful for your availability, kindness, patience, and ability to offer critical feedback—no matter the topic or time of day.

I would like to thank my committee members, Michael Bell, Christopher Davis, Christian Kummerow, and Karan Venayagamoorthy, for their guidance, encouragements, and hard questions. Special thanks go to Christian for hosting me at the Cooperative Institute for Research in the Atmosphere (CIRA) and supporting my research through CIRA's Education and Outreach Program.

I also thank Wayne Schubert, Sue van den Heever, Peter Hitchcock, Aaron Piña, Christopher Slocum, and past and current fellow students in the E. Barnes, E. Maloney, and D. Thompson research groups for fruitful interactions throughout the years. I have thoroughly enjoyed corridor conversations and group meeting discussions, which have on more than one occasion influenced my research. Heartfelt thanks go to Marie McGraw for her presence in the more difficult times. My appreciation also goes to the administrative staff of the Department of Atmospheric Science, CIRA, and of the International Student and Scholar Services, who have consistently made travel planning, tax filing, and other complex immigration-related paperwork seemingly effortless.

To my parents, Laurence and Jean-Michel, whose unrelenting support I have relied upon, and who have managed to stay present despite living an ocean away—merci. You have made it incredibly difficult for your children to choose one path in life, because you have made an incredible effort to open their eyes to all paths of life, and for that, I am eternally grateful. To my grandmother Geneviève and my family at large, who have always expressed genuine interest in my research, often provided wise life advice, and overall been part of the most rewarding part of my research—thank you. Special thanks to John Martin and Kayann Short, farmers at Stonebridge Farm in Lyons, CO, and to Michael Sommers, Julie Smith, Timothy Oakes, and barterers of Stonebridge Farm for their support, generosity, and friendship over the years.

This work has been financially supported by Colorado State University's Program of Research and Scholarly Excellence, and by the Education and Outreach Program of the Cooperative Institute for Research in the Atmosphere.

DEDICATION

“A l’amour, toujours !”

TABLE OF CONTENTS

LIST OF TABLES

LIST OF FIGURES

Introduction

Motivation for this work

The region between the tropical troposphere and stratosphere is best described as a transition layer, usually referred to as the tropical tropopause layer (TTL). The TTL is defined by Fueglistaler et al. (2009) between ~ 14 and $18.5\,\mathrm{km}$ above sea level (~ 150 to $70\,\mathrm{hPa}$), with the climatological cold point tropical tropopause located near $17\,\mathrm{km}$ (Seidel, Ross, Angell, & Reid, 2001). Due to its nature, the TTL is subject to influences from both tropospheric and stratospheric processes. From above, planetary-scale circulations in the stratosphere influence the TTL on intraseasonal to interannual time scales (Angell & Korshover, 1964; Reid & Gage, 1985). From below, mesoscale deep convective systems produce large temperature anomalies in the TTL (Holloway & Neelin, 2007; Johnson & Kriete, 1982; Jordan, 1960; Kim, Randel, & Birner, 2018; Paulik & Birner, 2012; Randel, Wu, & Rivera Ríos, 2003), alter its chemical composition (e.g., Danielsen, 1993; E. Jensen, Ackerman, & Smith, 2007) and its radiative flux balance (Gettelman, Salby, & Sassi, 2002; Kuang & Bretherton, 2004; Thuburn & Craig, 2002) by lofting air from the boundary layer into the TTL on time scales of a few hours. As a result of the above influences, the energy budget in the TTL is complex and each contribution needs to be quantified.

In this work, we seek to elucidate the origins and impacts of anomalous temperature signals found in the TTL above tropical cyclones (TCs). Specifically, Arakawa (1951), Koteswaram (1967), Biondi, Ho, Randel, Syndergaard, and Neubert (2013), and Rivoire, Birner, and Knaff (2016) have identified cooling within a layer a few kilometers deep surrounding the tropopause above TCs. We will refer to this ubiquitous signal as tropopause layer cooling (TLC hereafter). The primary motivation for this study is the limited understanding of plausible feedbacks between TLC and the structure and dynamics of underlying TCs. Anomalously low temperatures near the tropopause decrease the static stability (i.e., the resistance to vertical displacements) in the TTL, implying stronger updrafts in the upper troposphere and greater cloud top heights. Potential impacts include vertical advection of angular momentum by convective bursts and a corresponding upper-tropospheric cyclonic circulation and warm core, which Ohno and Satoh (2015) described inside the eyewall, and which translated to abrupt intensity changes in numerical simulations (Chen & Zhang, 2013; D.-L. Zhang & Chen, 2012). The destabilization of the upper troposphere may also modulate the stratification and vertical extent of the TC outflow layer, thereby impacting TC motion (Flatau & Stevens, 1993), structure (Holland & Merrill, 1984), and intensity (Doyle et al., 2017). An improved characterization of upper-level processes in TCs is needed in order to establish better understanding of these feedbacks.

Several mechanisms have been proposed to explain TLC. Koteswaram (1967) was one of the first studies suggesting overshooting cloud tops as a mechanism for the generation of cold air masses near the tropopause, saying that "the cold air would have a tendency to sink to lower levels and warm up, but as long as intense convection was maintained, it would be replenished almost continuously." Results in Johnson and Kriete (1982) and Fritsch and Brown (1982) later gave a new perspective on the matter, suggesting that even in intense deep convective events, overshooting may not be sufficient to explain net cooling on mesoscales. Other mechanisms have been proposed, namely, adiabatic expansion in the upward and outward branch of the TC secondary circulation, and diabatic cooling via longwave radiative cooling near the top of the cloud canopy. Despite the skepticism expressed about the latter in, e.g., Johnson and Kriete (1982) suggesting that clouds do not occur at high enough altitude and with large enough frequency to significantly affect the tropopause, results in Romps and Kuang (2009) provide renewed traction for this idea, which will be further tested in Chapter 2. The other mechanism (the effect of the secondary circulation) is predicted by the balanced vortex model (e.g., Schubert & McNoldy, 2010) for an intensifying vortex: the in, up, and out circulation may expand into the lower stratosphere, bringing ascent in a region where very little water vapor is available for latent heat release through condensation, i.e., a region where modest ascent may generate cooling. Testing this mechanism using observations is challenging given the overall lack thereof, and given the absence of direct observations of vertical velocities. A primary goal of this work is to test these mechanisms and determine their partition within TCs.

Scope of this work

Chapter 1 provides a high-resolution, updated description of the thermal structure in TCs using high-resolution temperature retrievals from the Constellation Observing System for Meteorology, Ionosphere, and Climate (COSMIC). A composite approach is chosen so as to isolate robust structures that are the tell-tale of universal underlying mechanisms, rather than anecdotal structures responding to storm-to-storm variability. The composited observations are then compared to reanalysis data, in an attempt to provide additional meteorological context to the presence of cold air masses near the tropopause.

Chapter 2 tests the validity of the mechanisms involving cloud radiative effects and the secondary circulation. The radiative impact of clouds on the TTL is evaluated using unique, vertically-resolved radiative heating rates calculated from liquid and ice water content estimates from the CloudSat Profiling Radar (CPR), CALIPSO's Cloud-Aerosol Lidar with Orthogonal Polarization (CALIOP), and the Moderate Resolution imaging Spectrometers (MODIS) onboard Terra and Aqua. These heating rates are compared to temperature tendencies derived from COSMIC in order to determine the contribution of cloud radiation to TLC. The effect of the secondary circulation is evaluated using reanalysis data as in Chapter 1, as well as numerical simulations of TCs using the Cloud Model 1 (CM1, Bryan & Rotunno, 2009).

Chapter 3 makes predictions for TLC-cloud feedbacks using parcel theory applied to a pseudo-adiabatic moist updraft. These predictions, which are mainly qualitative and idealized, are then tested with a very simple numerical framework in principle relevant to parcel theory: simulations of atmospheric warm bubbles. These simulations are also run using CM1, and are meant as a first step towards understanding the complex response of clouds to TC-induced perturbations in their thermodynamic environment.

Section 1.1 of Chapter 1 is published in Rivoire et al. (2016). Work in Chapter 2 Section 2.1 is published in Rivoire, Birner, Knaff, and Tourville (2020). A manuscript for the work on reanalysis data sets (Chapter 1 Section 1.2 and Chapter 2 Section 2.2) is being prepared, as well as a manuscript for the work using numerical simulations (Chapter 2 Section 2.2.2).

Chapter 1

Characterization of tropopause layer cooling

1.1 Using GPS radio occultation temperature retrievals

This section includes results which were published in Rivoire et al. (2016). Temperature retrievals from the Constellation Observing System for Ionosphere, Meteorology, and Climate (COSMIC) are composited globally in the vicinity of TC best tracks to describe the average thermal structure of TCs in the upper troposphere and lower stratosphere. The results are compared with composites from two other data sources: geostationary infrared imagery and microwave imagery, both from sensors onboard operational satellites.

1.1.1 Methods

COSMIC Radio occultation uses Doppler shifts in GPS radio signals detected by low-orbiting satellites to retrieve bending angle profiles in the atmosphere. Radio waves emitted by the Global Positioning System (GPS) satellites are detected by COSMIC satellites in low Earth orbit. When the line of sight between GPS and COSMIC satellites passes through the atmosphere, radio waves are refracted depending on the state of the atmosphere—primarily its temperature, pressure, and water vapor content, see E. Kursinski, Hajj, Schofield, Linfield, and Hardy (1997). Bending angle is primarily related to the temperature, pressure, and water vapor content of the atmosphere. The COSMIC Data Analysis and Archival Center (CDAAC) processes bending angle data to provide temperature profiles with high accuracy, precision, and vertical resolution, especially between 5 and $25\,\mathrm{km}$ height (Kuo et al., 2004). COSMIC profiles are available for all weather conditions, and have a global distribution that peaks in the subtropics and midlatitudes (e.g., Son, Tandon, & Polvani, 2011). In the upper troposphere and lower stratosphere (UTLS), these measurements are the only source of space-based data unaffected by clouds and their precision was estimated near $0.05\,\mathrm{K}$ by comparing colocated retrievals (Anthes et al., 2008). The accuracy of COSMIC refractivity retrievals was estimated as a departure from other independent data sets near 0.1–$0.5\,\%$, yielding temperature errors of order 0.1–$1\,\mathrm{K}$ assuming a dry atmosphere (Anthes et al., 2008; Kuo et al., 2004). Biondi, Randel, Ho, Neubert, and Syndergaard (2012) demonstrated that GPS-RO data can be used to detect vertical thermal structures in strong convective systems. The contribution of the water content to the bending angle is considered negligible for temperatures less than $250\,\mathrm{K}$ (E. Kursinski, Hajj, Bertiger, Leroy, et al., 1996), directly allowing retrieval of the temperature and pressure at upper levels (these profiles are referred to as "dry retrievals"). In the lower troposphere where the water content affects the bending angle, temperature estimates from 1D-var analysis using the European Centre for Medium-range Weather Forecasting (ECMWF) low-resolution analysis data are used to retrieve profiles of temperature, pressure, and water vapor (referred to as "wet retrievals"). However, such estimates can be of poor quality in regions of large horizontal gradients (Davis & Birner, 2016). TCs can be expected to be misrepresented in meteorological analyses and are therefore likely to be misrepresented in the wet retrievals. This study therefore focuses on the UTLS region where temperature profiles are most accurate. Wet retrievals will be used as a qualitative complement to dry retrievals below $10\,\mathrm{km}$.

COSMIC profiles are collected near six-hourly TC best-track locations from the Automated Tropical Cyclone Forecast (ATCF) (Sampson & Schrader, 2000) system archive (ATCF data is from the National Hurricane Center and the Joint Typhoon Warning Center). Best track uncertainty estimates are typically 15–40 nautical miles (28–$74\,\mathrm{km}$) in terms of location and 8–12 kt (4–$6\,\mathrm{m\,s^{-1}}$) in terms of intensity (Knaff, Brown, Courtney, Gallina, & Beven, 2010; Torn & Snyder, 2012). These uncertainties are small for the purpose of compositing at large distances from the TC center. Closer to the TC center, these uncertainties produce smoothing comparable to that introduced by varying TC size and by the choice of horizontal resolution of the composites. COSMIC profiles are then positioned about the time of first Lifetime Maximum Intensity (LMI) determined using intensities from the ATCF database. Intensities are based on 1-minute sustained wind speeds. Intensities equal to the LMI can be reached several times during the lifetime of one TC; here, LMI will refer only to the first such maximum for each TC. Individual temperature profiles are linearly interpolated onto a regular 200 m vertical grid, corresponding to the typical vertical resolution of GPS-RO data near the tropopause (E. R. Kursinski, Hajj, Leroy, & Herman, 2001). Profiles are assigned to the nearest neighboring best-track point (in space), allowing a maximum time offset of 5 hours. This time offset was chosen after careful consideration in order to improve statistics, and each COSMIC profile is used only once. Profiles are collected up to 1500 km away from the storm center, although it should be noted that the convective region in TCs has a typical radius of 400–700 km (Frank, 1977). Data collected outside TC systems provides background information and gives insights into the horizontal extent of temperature anomalies associated with TCs. This sampling process is repeated for the hurricane-strength TCs (LMI $\geq 64\,\mathrm{kt}$ or $33\,\mathrm{m\,s^{-1}}$) occurring within $\pm 35°$ of latitude in 2007–2014, allowing the collection of over 33000 radio occultation profiles near 322 storms around the globe. This large amount of data is required to overcome the substantial variability in the vertical structure of TCs and draw robust conclusions (Stern & Nolan, 2009). Note that profiles collected over land are included in the study as their impact on the results were found to be small. Finally, profiles collected poleward of $\pm 35°$ of latitude are not included to avoid sampling poleward of the subtropical jets.

Composites of temperature anomalies are built based on the time of LMI to reveal the evolution of the thermal structure in TCs. Anomalies are displayed relative to two backgrounds: the monthly climatological background from the COSMIC dataset, interpolated to each COSMIC profile (referred to as "local climatology") and the area average between 1300–1500 km away from the storm center (referred to as the "far-field background"). Using the local climatology emphasizes temporal anomalies, whereas using the far-field background emphasizes spatial anomalies. Radial composites are also constructed to unveil horizontal structures.

Microwave imagery

TC microwave temperature analyses are byproducts of an operational procedure that provides intensity and surface wind estimates for TCs as described in Demuth, DeMaria, and Knaff (2006). Temperature from the Advanced Microwave Sounding Unit-A (AMSU-A), along with real-time operational estimates of TC locations, are the primary inputs for this product. The temperature retrieval uses limb corrections for scan position and viewing angle (Goldberg, Crosby, & Zhou, 2001) and a linear retrieval operator derived from collocated rawindsonde data (Knaff, Zehr, Goldberg, & Kidder, 2000) that provides temperature as a function of pressure at 40 levels from 1000 to $0.1\,\mathrm{mbar}$, up to $600\,\mathrm{km}$ away from the storm center. Composites of temperature anomalies are constructed based on the time of LMI using the same TC tracks as with COSMIC.

Infrared imagery

Brightness temperature (T_b) provides information about the temperature of cloud tops found in TCs and is a proxy for convective vigor. The analyses of IR T_b used are derived from data collected by the constellation of geostationary satellites. The central wavelength of these data is located in the IR window near $11\,\mu\mathrm{m}$, where T_b is within a few degrees of the emitting surface conditions in the absence of clouds. The Cooperative Institute for Research in the Atmosphere (CIRA) archives T_b analyses within $600\,\mathrm{km}$ of TCs with at least an hourly temporal resolution and a precision of $0.5 - 1\,\mathrm{K}$. Additional information appears in Knaff, Longmore, and Molenar (2014). These analyses are composited hourly about the time of LMI using the same TC tracks as with COSMIC.

1.1.2 Results

Figure 1.1 shows the azimuthally averaged horizontal temperature structure in TCs inferred from AMSU-A data at LMI with a horizontal resolution of $\sim 70\,\mathrm{km}$ and a vertical resolution of $1 - 3\,\mathrm{km}$. The upper-tropospheric warming bulges upward near the storm center where the convective activity is strongest. Tropopause-level cooling occurs at $17\,\mathrm{km}$ above sea level ($\sim 100\,\mathrm{mbar}$, above the core of the outflow layer) as shown in Koteswaram (1967) and peaks at $\sim 200\,\mathrm{km}$ away from the storm center, which is well outside the typical radius of the eye ($15 - 30\,\mathrm{km}$, Weatherford & Gray, 1988) and the associated warm subsidence region. The amplitudes of the anomalies ($3.7\,\mathrm{K}$, $-0.7\,\mathrm{K}$) are smaller than those found by case studies (10 to $13\,\mathrm{K}$, -8 to $-10\,\mathrm{K}$, e.g., Koteswaram, 1967). This may be caused by the large variability in the vertical structure of the

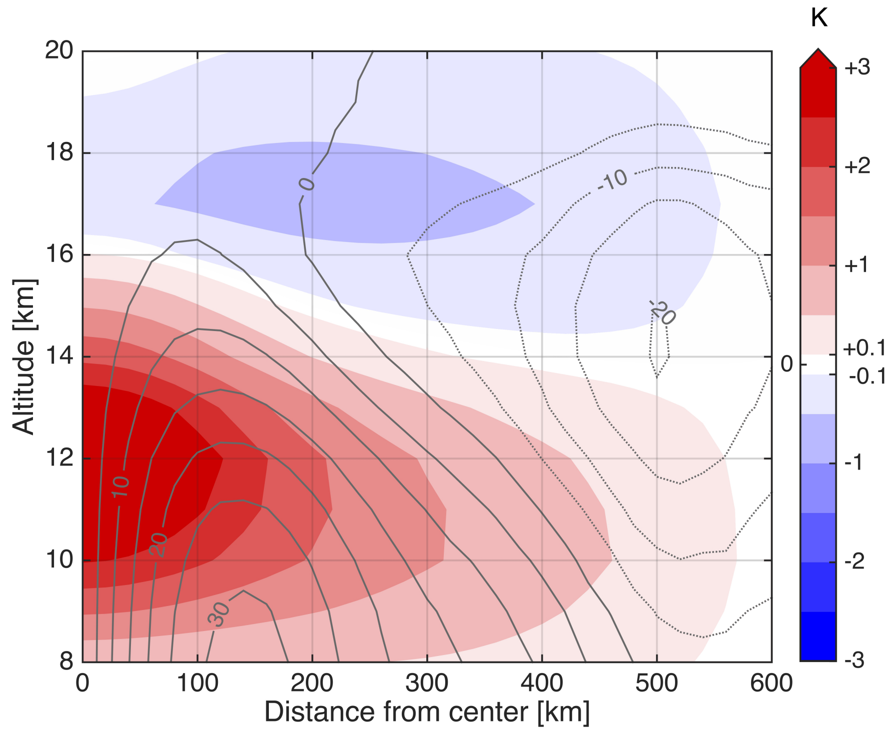

Figure 1.1: Temperature anomaly from AMSU-A within 3 hours of LMI as a function of radius and altitude (above 8 km). Shaded contours show the temperature anomaly, grey contours show the tangential wind in m s^{-1} estimated from the height gradients calculated from AMSU-A temperatures using GFS boundary conditions as in Demuth et al. (2004), assuming 1D gradient balance. Anomalies are relative to the temperature at 600 km. Solid (dotted) wind contours show the cyclonic (anticyclonic) flow.

TCs that are composited (Stern & Nolan, 2009), and by the relatively limited vertical resolution of AMSU compared to the relatively small vertical extent of the tropopause layer cooling (Figure 1.3).

Figure Figure 1.2 shows the evolution of the azimuthally averaged T_b in TCs inferred from IR images, and of TC intensity, relative to LMI. IR data show that the coldest cloud tops occur before LMI; in other words, the convective structure evolves asymmetrically about LMI. In comparison, the intensity of TCs evolves with a much weaker degree of asymmetry. Between –4 and –2 days, low T_b is associated with the presence of deep convective outbursts within a few hundred kilometers of the storm center. Between –2 and 0 days, T_b is consistent with the formation of a sustained ring of deep convective clouds between the outer edge of the eye and 100 km away from the storm center (e.g., Buontempo, Flentje, & Kiemle, 2006; Heymsfield, Halverson, Simpson, Tian, & Bui, 2001). As TCs move towards latitudes with lower sea surface temperatures, both their intensity

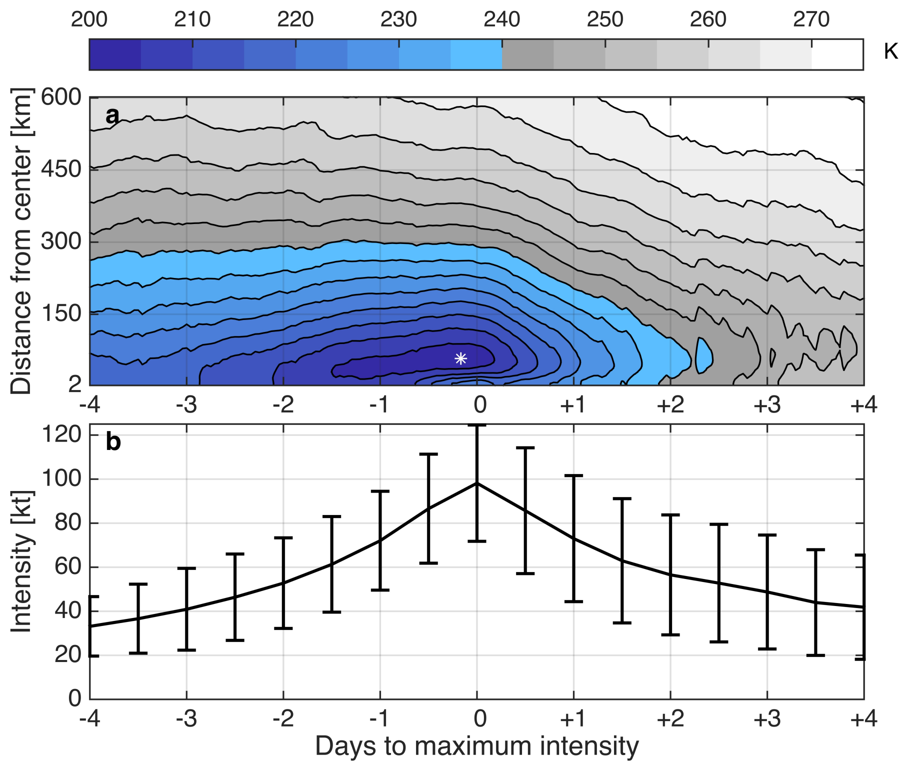

Figure 1.2: a) Azimuthally averaged brightness temperature in TCs contoured as a function of time relative to LMI and radius. The temporal resolution is hourly and the radial resolution is $4\,\mathrm{km}$. The white asterisk indicates the minimum value of T_b ($202\,\mathrm{K}$). **b)** Average intensity of hurricane-strength storms between $\pm 35°$ of latitude in ATCF, as a function of time relative to LMI. Error bars indicate ± 1 standard deviation every 12 hours.

and the heights reached by deep convection decrease rapidly, which translates to greater T_b after LMI. Within 30 km of the storm center at LMI, greater T_b offers evidence of eyes with relatively clearer air due to subsidence.

Temperature anomalies inferred from GPS-RO measurements are shown in Figure 1.3. Anomalies within 600 km of the storm center and 24 hours of LMI are shown relative to both the local climatology and far-field background. In the upper troposphere, water vapor amounts are small enough that moist and dry adiabats are essentially the same ($\sim 9.8\,\mathrm{K\,km^{-1}}$). The climatological lapse rate is close to $8\,\mathrm{K\,km^{-1}}$ (Gettelman et al., 2011), and the anomalous thermal structure shown in Figure 1.3 increases this lapse rate by almost $1\,\mathrm{K\,km^{-1}}$, which is about halfway towards

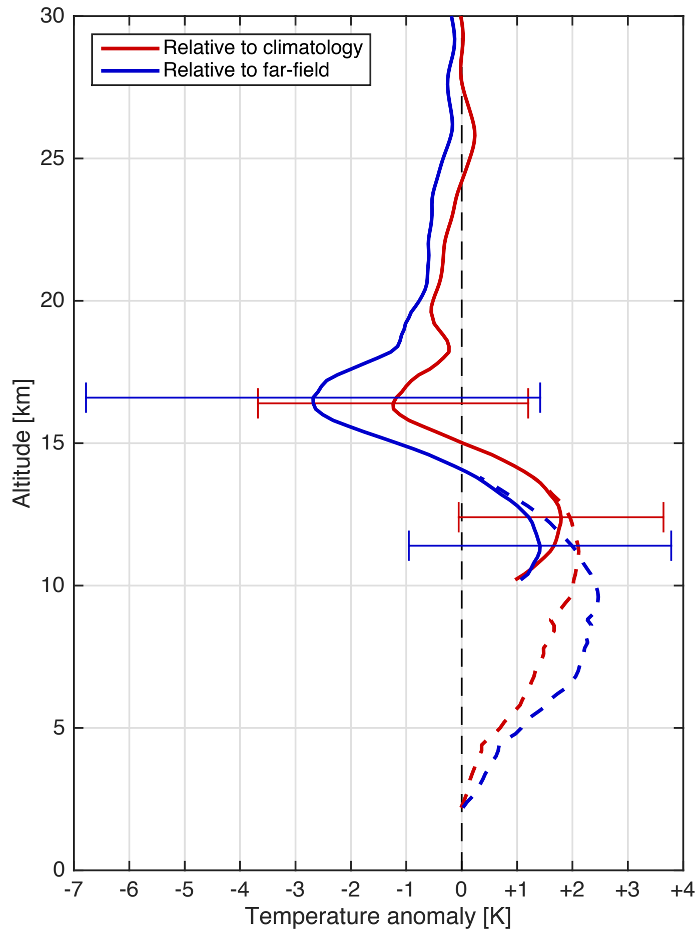

Figure 1.3: Average temperature anomaly for all COSMIC profiles collected within 600 km and 24 hours of LMI. Solid (dashed) lines are the dry (wet) retrievals. Error bars show ± 1 standard deviation at the location of the largest anomalies in the dry retrievals.

the dry adiabat. The altitude of the largest anomalies is consistent with Biondi et al. (2013). Wet retrievals have a significant warm bias above $15\,\mathrm{km}$ (not shown). The difference between the two curves indicates that the far-field upper troposphere (above $11\,\mathrm{km}$) is on average warmer than the climatological upper troposphere near the storm center.

Figure 1.4 shows temperature anomalies contoured as a function of distance from the storm center and altitude for 48 hours-wide temporal bins centered on -2, 0, 2, and 4 days from LMI, with a $200-\mathrm{km}$ radial resolution. Anomalies are defined with respect to the far-field background. At LMI, the horizontal extent of the tropopause-level cooling reaches a peak, while that of the

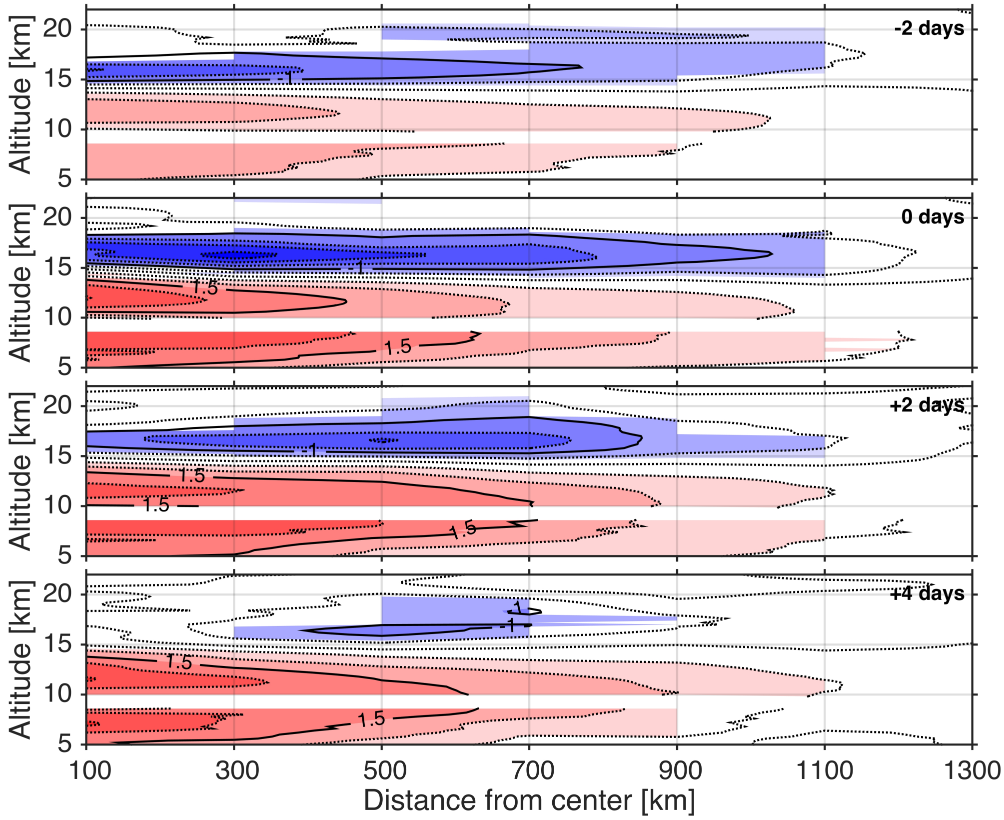

Figure 1.4: Temperature anomaly from COSMIC contoured for various times before and after LMI as a function of the distance from the center of storms and altitude. Solid contours are at -1 and $1.5\,\mathrm{K}$, dotted contours are every $0.5\,\mathrm{K}$. Anomalies exceeding the t-test 95% significance level are shaded. Anomalies are relative to the area average between $1300-1500\,\mathrm{km}$ away from the storm center at each height. The composite includes data from –3 to +5 days, and TC tracks that cover at least the period from –2 days to +4 days are used. The white horizontal band just below $10\,\mathrm{km}$ separates dry and wet retrievals. Each panel corresponds to a 48-hour-wide window, and the radial resolution is $200\,\mathrm{km}$.

upper-tropospheric warming is still expanding. Upper-tropospheric warming bulges upward near the storm center like in Figure 1.1, although not as noticeably. At +2 days, the upper-tropospheric warming reaches its maximum radial extent while the tropopause layer cooling weakens and clearly dissociates itself from the storm center. At +4 days, a faint tropopause layer cooling is still evident between $400-700\,\mathrm{km}$. The upper-tropospheric warming remains as strong as it was at LMI, either indicating stabilization of the storm or a bias due to the under-sampling of the inner core region.

Figure 1.5 compares the evolution of the vertical structure of temperature anomalies in TCs relative to the local, climatological background (top panel), with anomalies relative to the far-field background (bottom panel). Relative to the local climatology (top panel), both the warm and cold signals become stronger and deeper as TCs develop. The warm core weakens beyond +4 days, although fewer data points are included in the composite after that time. The tropopause-level signal deepens after LMI, when TCs are at a latitude of $20°\pm6°$ on average—where the climatological tropopause warms when moving poleward (Seidel et al., 2001). Tropopause-level anomalies extend far outside the $500\,\mathrm{km}$ radius (not shown) and indicate large-scale poleward transport of cold, dry air.

The far-field background (bottom panel) reveals an anomalously cold tropopause several days before LMI, analogous to the development of the coldest cloud tops in Figure 1.2. The cooling quickly decays after +1 days, in agreement with tropopause-level anomalies moving away from the storm center (Figure 1.4). This decay coincides with rapidly increasing T_b near the storm center (Figure 1.2). Upper-tropospheric warming persists after LMI, although it should be noted that a few days after LMI, the weaker storms have dissipated and are therefore not included in the sample.

The differences between the two panels for the dry retrievals indicate that the far-field upper troposphere is warmer than the climatological upper troposphere near the storm center (as in Figure 1.3) during the lifetime of TCs. The far-field UTLS is warmer than the climatological UTLS at the location of the storm during tropical cyclogenesis. For both backgrounds, the larger the LMI the larger the amplitude of the anomalous thermal structures (not shown).

1.1.3 Discussion and conclusions

Leveraging the 200-m vertical resolution of GPS-RO, the $\sim$70 km horizontal resolution of AMSU-A data, and the $\sim$4 km horizontal resolution of geostationary IR images, the composite fine-scale thermal and convective structure in TCs was analyzed. The composite analyses presented here show the expected qualitative behavior of mid to upper-tropospheric warming and tropopause layer cooling. They also reveal that the tropopause layer cooling precedes the warm core signal when measured relative to the far-field structure around storms. This is consistent with the presence

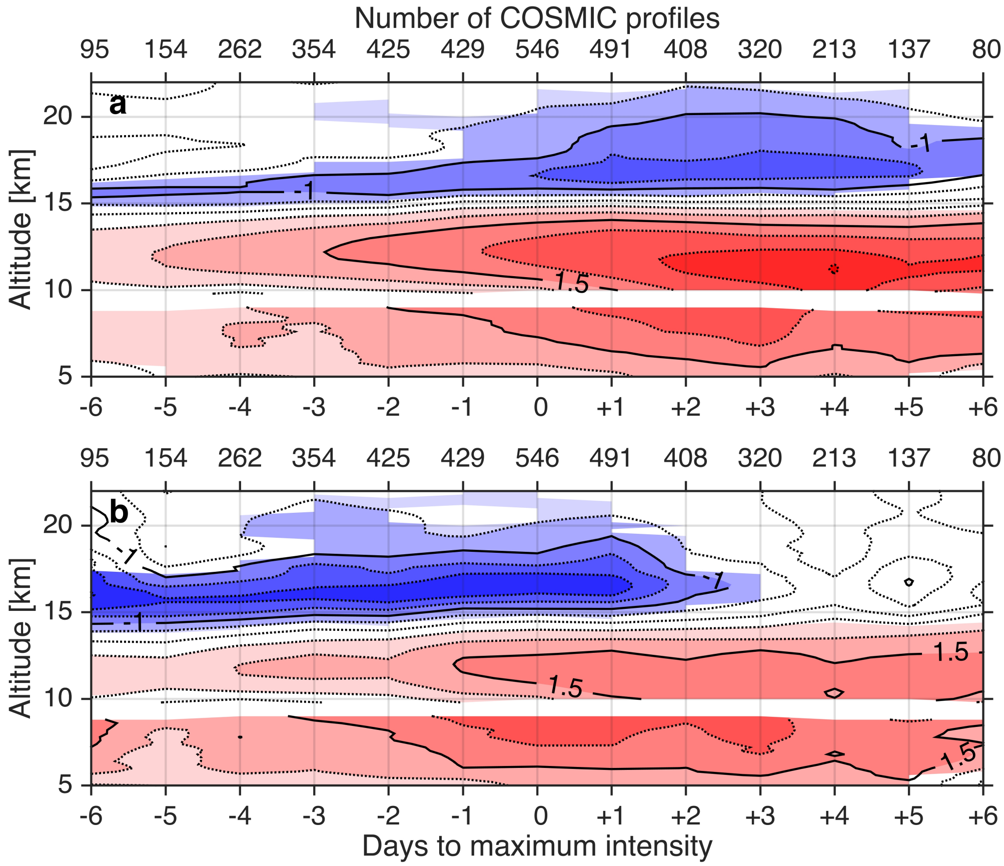

Figure 1.5: Temperature anomaly from COSMIC within 500 km of TCs contoured as a function of time relative to the time of LMI and altitude. Solid contours are at –1 and 1.5 K, dotted contours are every 0.5 K. Anomalies exceeding the t-test 95% significance level are shaded. Anomalies in (a) are relative to the local climatology, in (b) are relative to the area average between 1300–1500 km away from the storm center. Horizontal labels apply to both panels. The white horizontal band just below 10 km separates dry and wet retrievals. The temporal resolution is 1 day.

of cold cloud tops near the storm center during the intensification period found in IR data, the convective bursts that Rogers, Reasor, and Lorsolo (2013) found in intensifying TCs, and the lag between the convective intensification and the response of the vortex (Steranka, Rodgers, & Gentry, 1986).

Cold anomalies at the tropopause locally destabilize the atmosphere to convection, which may exert a feedback on the depth of existing convection. Since cold anomalies precede the establishment of a warm core, the upper-level destabilization might play a role in priming the eyewall updraft that Willoughby (1998) described as a “heat pump”. This might reinforce the diabatically-driven secondary circulation and indirectly stiffen the vortex to vertical wind shear (Reasor, Montgomery, & Grasso, 2004), which is of particular importance during tropical cyclogenesis.

The dissociation of tropopause-level anomalies from the storm center and their dissipation after LMI indicate radial outward transport near the tropopause (above the core of the outflow layer) and a decrease in the upper-level adiabatic cooling near the storm center, respectively. The latter can be understood as a decrease in the height reached by the eyewall branches of the secondary circulation: idealized experiments by Schubert and McNoldy (2010) showed horizontally elongated, vertically compressed secondary circulations for weak vortices, and vice versa for strong vortices. Remains of cold air masses lie near the tropopause at $400-700\,\mathrm{km}$, essentially inward of the radius of maximum tangential anticyclonic winds in the UTLS (Frank, 1977). Integrating the hydrostatic relation, cold air ($-1\,\mathrm{K}$) sitting above the edge of a deep warm core ($1.5\,\mathrm{K}$) is found to increase the near-surface pressure difference between the inner and outer regions of TCs by $3-4\,\mathrm{mbar}$, potentially increasing the maximum winds in a typical hurricane by $4-10\,\mathrm{kt}$ (using an empirical relationship from Courtney & Knaff, 2009).

At maximum intensity, cold air masses extend as far as $1000\,\mathrm{km}$ away from the storm center. This may be significant for meridional heat and moisture transport: while the warm core transports heat and water vapor poleward in the troposphere, there may be a significant poleward transport of cold, dry air in the UTLS originating in the tropics.

1.2 Using reanalysis data sets

With the temperature composites in Section 1.1 providing an updated and high-resolution picture of TLC over the average TC, the representation of TLC in global models should be evaluated. This will help determine whether global models can be used to study the mechanisms responsible for TLC in Chapter 2. To this end, reanalysis data sets are used which incorporate a global model and data assimilation (including assimilation of temperature retrievals from COSMIC). A distinct advantage of using reanalysis data sets is their continuous coverage in both time and space, which may be leveraged to answer questions that the COSMIC data set may not answer. However, given the coarse resolution of reanalysis data sets and their inability to explicitly resolve processes such as convection, the representation of TCs in reanalysis data must be evaluated with care. These aspects are discussed in this section. A tracking algorithm is developed in Section 1.2.1, and temperature composites are compared against observations in Section 1.2.2.

1.2.1 Tropical cyclone tracks in reanalysis data sets

When it comes to detecting TC in reanalysis data sets, one should first acknowledge that reanalyses do not realistically produce the fast-rotating, eye-bearing storms that are TCs. This incapacity comes from the generally coarse spatial resolution of reanalyses—resolution which is often too large to properly capture the TC main rainband, let alone the eye. Rather, reanalyses produce relatively slow and wide vortices which exhibit TC-like features (low-level cyclonic inflow, upper-level anticyclonic outflow, circular cloud field, etc) and which move about in a way similar to real TCs. Although these modeled vortices should perhaps be referred to as TC-like vortices, they will be referred to as TCs for the sake of concision.

Methods for tracking TCs in model output already exist (e.g., Bengtsson, Botzet, & Esch, 1995; Camargo, Barnston, & Zebiak, 2005; Hodges, Cobb, & Vidale, 2017; Horn et al., 2014; Manganello et al., 2012; Murakami, 2014; Vitart, Anderson, & Stern, 1997; Walsh, Fiorino, Landsea, & McInnes, 2007), so why develop a new one? Existing methods use a variety of dynamic and thermodynamic thresholds (e.g., minima in mean sea-level pressure, maxima in wind speeds, vorticity, or upper-tropospheric temperature) and geographic criteria (track duration, latitude of genesis) applied either globally or as model- or basin-dependent parameters, sometimes based on spatial resolution to account for inter-model differences, and sometimes even chosen so as to minimize the statistical distance between model tracks and best tracks. While most methods are relatively simple (detection based on meteorological variables or metrics exceeding their climatological value), the thresholds used are most often chosen subjectively (judiciously, but subjectively). Some methods, for instance Hodges et al. (2017, based on Hodges (1994, 1995, 1999)) are complex enough to involve spectral filtering of model output with adaptive constraints on track smoothness, in order to track model features which are dynamically consistent with a complex definition of the center of a TC and produce tracks which are least susceptible to excursions due to small-scale features or vertical variability. All methods are as diverse as the applications they were developed for, but they share a common characteristic: they produce TC tracks with spatial and temporal distributions in good agreement with those of real TCs. This suggests that global models and reanalysis data sets are skilled enough to represent TCs in the vicinity of their best tracks, and with correlated intensity. Instead of choosing or modifying one existing method (besides the fact that reproducing existing methods can prove difficult, even when their full description is available) the skill of the reanalysis data sets is exploited to design a new, extremely simple method. If reanalysis data sets capture TCs in their general, real-world vicinity, using the best tracks as a first guess to track model TCs seems reasonable. The goal here is not to develop a method that is very accurate for individual TCs or that is operationally capable. Rather, it is to find the simplest possible approach that produces TC tracks with comparable quality to existing ones, and with the less large use of subjectively defined identification thresholds (which are a large source of variability between existing methods according to Horn et al., 2014). The method is formulated as follows:

A model TC track location is defined as that of the local minimum in mean sea-level pressure closest to the corresponding best track location and no farther than $500\,\mathrm{km}$.

The best track locations are used as a first guess, and the TC center is defined as the closest minimum mean sea-level pressure. In the case where no local minimum is found ($1-5\,\%$ of the time in practice), the model TC track is assigned the best track and flagged as such. The distance threshold for track detection ($500\,\mathrm{km}$) was chosen as a middle ground between larger thresholds which lead to larger fluctuations in track position, and smaller thresholds which increasingly prevent detecting sea-level pressure minima. Mean sea-level pressure was chosen because it exhibits less small-scale features which may correspond to features other than TCs. In a sense, part of the work around the choice of detection thresholds is relieved by the use mean sea-level pressure. As stated earlier, this method is developed with the statistical quality of the output in mind. The output for individual systems may not be of much value to applications that focus on individual systems. For the purpose of this study, the method described here (referred to as "GEM", for good enough method) trades individual track quality against simplicity and reproducibility.

Once track locations are established, TC intensity may be determined. For simplicity, and for the sake of comparison with some results presented in Hodges et al. (2017, referred to as H17), the intensity is defined in the GEM as the magnitude of the longest wind vector with a non-zero cyclonic component at the $925\,\mathrm{hPa}$ level, within $400\,\mathrm{km}$ of each track location. The $400\,\mathrm{km}$ threshold was chosen a posteriori and informed by results from Section 1.2.2; it reflects the fact that the radius of maximum wind is oftentimes located at large radii from the track location in reanalyses ($250 - 500\,\mathrm{km}$). Note that generally speaking, TC intensity in reanalysis data sets is based on the $10 - \mathrm{m}$ wind field, which is not a model prognostic and is calculated by extrapolation of the wind field from the model's lowest vertical level down to the surface. While wind velocities so calculated may be closer in magnitude to their real-world counterparts, this technique is not adopted in the GEM. How discrepancies between best track intensity and reanalysis intensity are mitigated is discussed in Section 1.2.2.

The performance of the GEM for individual systems is shown in Figure 1.6, and its statistical performance compared to that of H17 in Figure 1.7. Two reanalysis data sets are chosen for this study: the European Centre for Medium-Range Weather Forecasts (ECMWF) interim reanalysis (ERA-Interim, hereinafter ERAi) (Dee et al., 2011) and the National Aeronautics and Space Administration (NASA) Modern-Era Retrospective Analysis for Research and Applications Version 2 (MERRA-2, Bosilovich & Coauthors, 2015; Molod, Takacs, Suarez, & Bacmeister, 2015). These two data sets were chosen because MERRA-2 performs relatively well and ERAi relatively poorly when it comes to TC occurrence, size, and intensity (Hodges et al., 2017). Severe Tropical Storm Jade illustrates cases where the GEM performs poorly, primarily when systems are poorly organized or weak, with less well-defined features in the mean sea-level pressure. Despite the reanalysis tracks displaying unrealistic features in MERRA-2, the intensity evolution is captured quite well. Hurricane Ophelia illustrates cases where the GEM performs the best; often, corresponding to intense, well-defined systems. In this case, despite the proximity in the reanalysis and best tracks, the GEM captures underestimated intensities. The increase in reanalyzed intensity at long time leads (after April 5 for Jade, after September 21 for Ophelia) is linked to larger horizontal wind shear at higher latitudes; the GEM is unable to differentiate between TC-related winds and environmental winds. This is not a concern for studying tropical processes. The overall (statistical) performance of the GEM as shown in Figure 1.7 shows that the GEM performs similarly to H17 for both reanalyses. What is most remarkable about the GEM is that it captures intensities very similar to H17 despite its simplicity. In a sense, estimating TC intensity in reanalyses does not seem to require more than locating the maximum wind velocity magnitude—regardless of its direction—in the vicinity of the best track.

The wind-pressure relationship, representative of the conversion of latent heating into kinetic energy, is shown in Figure 1.8 to further test the performance of the GEM. The method in H17 yields more consistent results across the two reanalyses, while the GEM yields large differences between them. The GEM produces a wind-pressure relationship for ERA-i that is similar to those from H17. For MERRA-2, the wind-pressure relationship is closer to that of the best track records. Overall, the GEM yields relationships that are closer to those from the best track record than the method from H17. This puts in perspective the results of a complex method and those of a simple one.

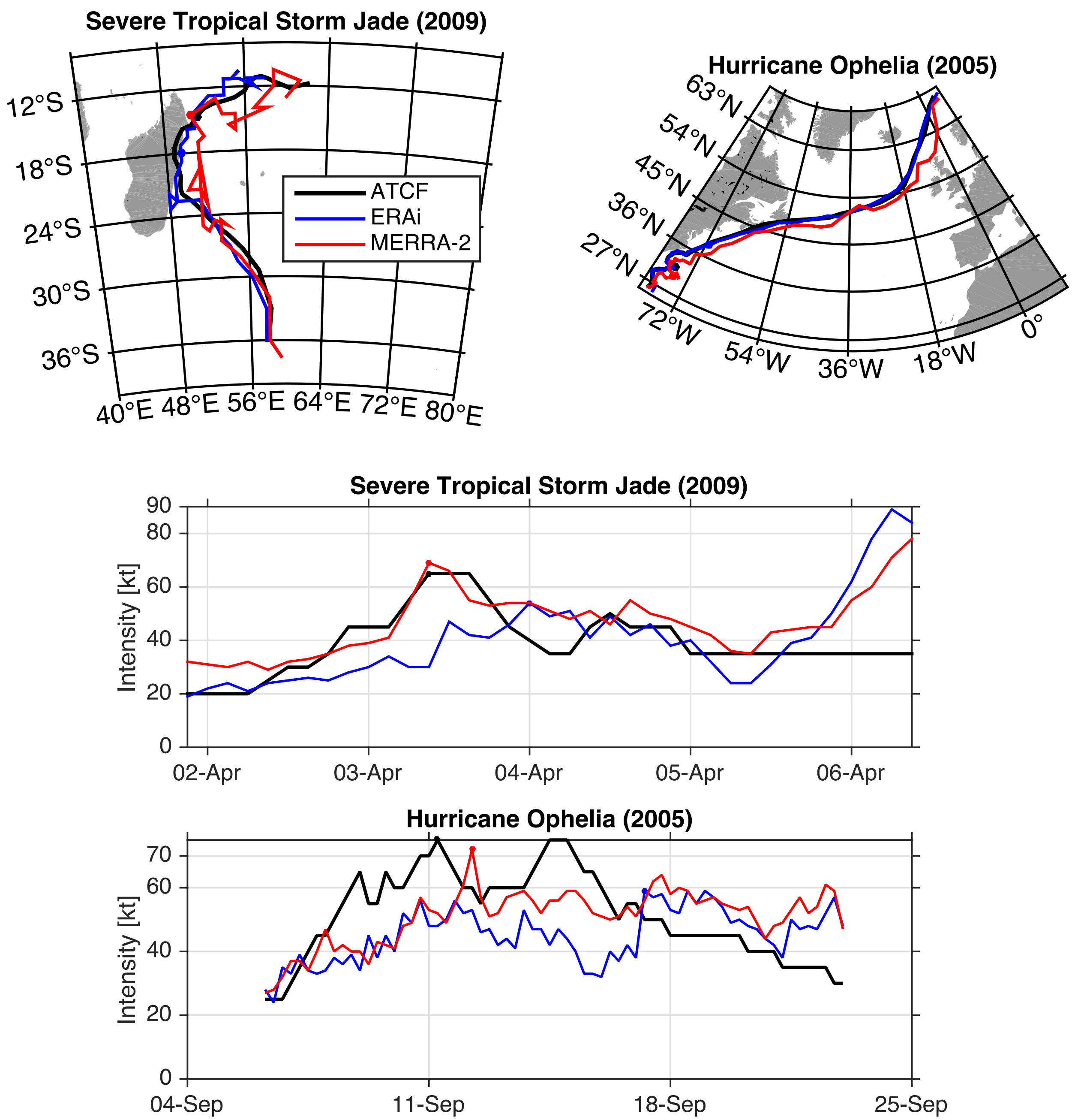

Figure 1.6: Maps and intensity evolution for a system for which the average distance between the best track (black) and the reanalysis tracks (colors) is large (Severe Tropical Storm Jade of 2009) and small (Hurricane Ophelia of 2005). The time and location of Lifetime Maximum Intensity are indicated by small colored circles.

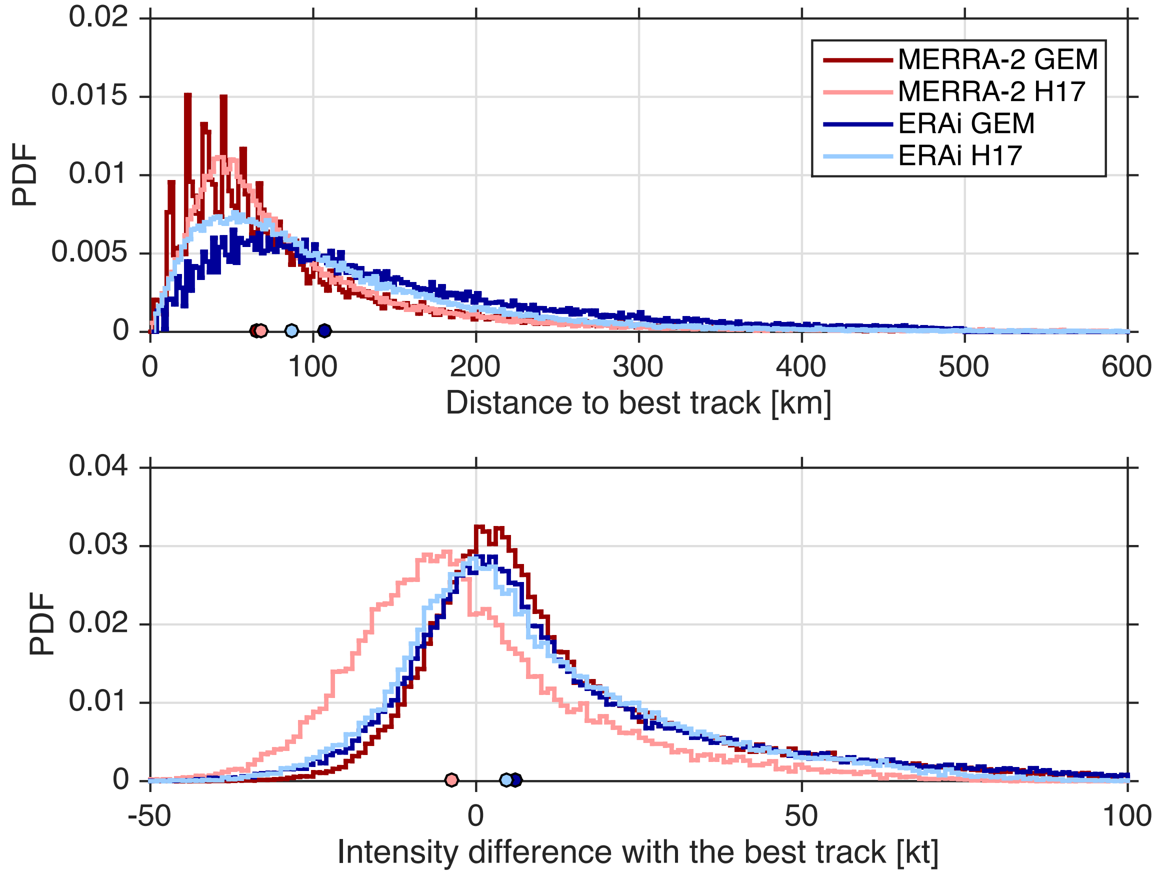

Figure 1.7: Probability distribution for the distance (top) and intensity differences (bottom, positive values indicating underestimation in the reanalysis) between the best tracks and reanalysis tracks, for all systems between $1990 - 2014$ globally. Intensity is defined on the $925\,\mathrm{hPa}$ level. The colored circles indicate the median for each distribution.

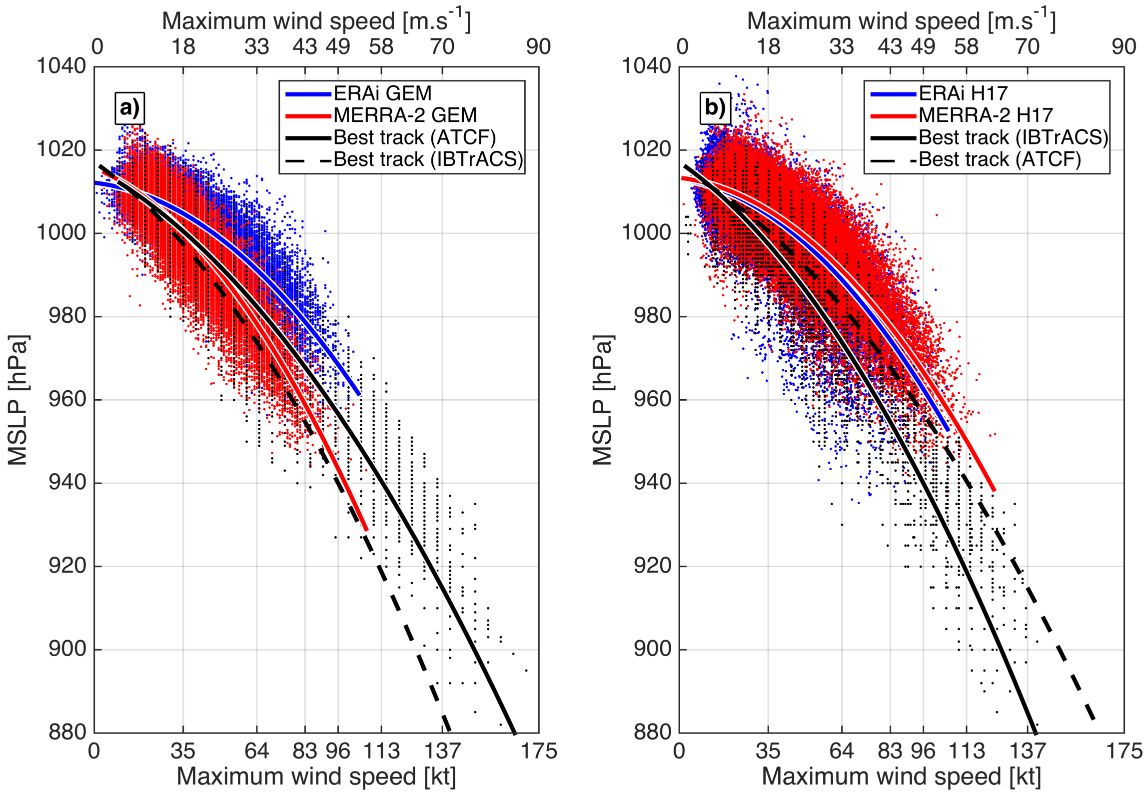

Figure 1.8: Wind-pressure relationship for **a)** the GEM and **b)** for H17. Intensity is defined on the $925\,\mathrm{hPa}$ level in **a)** and **b)**.

1.2.2 Comparison with observations

Since the separation distance between best tracks and reanalysis tracks is non-zero on average and exhibits a heavily skewed distribution, using the best tracks directly to composite reanalysis data (as in Ditchek, Molinari, & Vollaro, 2017) is not ideal. Composited data can in this case be systematically shifted by $50 - 150\,\mathrm{km}$, likely resulting in further smoothing of the average TC structure. Although, given the horizontal resolution of the available reanalyses, $50 - 150\,\mathrm{km}$ only equates to 1–2 grid points. The tracks from the GEM are used to composite reanalysis data and analyze the structure of the UTLS within them. As in Section 1.1, only hurricane-strength systems are used (that is, systems which maximum intensity exceeds $64\,\mathrm{kt}$). Since the intensity of reanalysis tracks can be largely underestimated (Figure 1.7), and especially their maximum intensity (not shown), the $64\,\mathrm{kt}$ threshold is adapted for each reanalysis. $64\,\mathrm{kt}$ is roughly the 55th percentile of maximum intensity in the best track data set of reference for the GEM (the ATCF data set). The 55th percentile of maximum intensity is therefore used as the threshold to define "hurricane strength" in the reanalyses: $48\,\mathrm{kt}$ for ERAi, $60\,\mathrm{kt}$ for MERRA-2. Figure 1.9 compares the average temperature anomaly profile within TCs for COSMIC and the reanalyses. Overall good agreement is found, including in the variability of the temperature near the tropopause $(100\,\mathrm{hPa})$. The anomalies in Figure 1.9 represent large scale radial temperature gradients, and it is reassuring to see that they are properly captured in reanalyses. Since reanalyses use data assimilation, it is conceivable that the representation of the average thermal structure may not be the product of the model formulation alone. Bending angles from GPS radio occultation and infrared and microwave radiances are assimilated in the reanalyses used here. However, in the vicinity of TC-like systems, it is possible that satellite retrievals and analyses differ too much for these data to be assimilated. For this reason, the impact of data assimilation on the thermal structure in Figure 1.9 is expected to be small. As a simple check, the thermal structure before 2007 and after 2007 (before and COSMIC was available) were compared, and no significant differences were found, i.e., changes in the data assimilation scheme did not impact the results shown here.

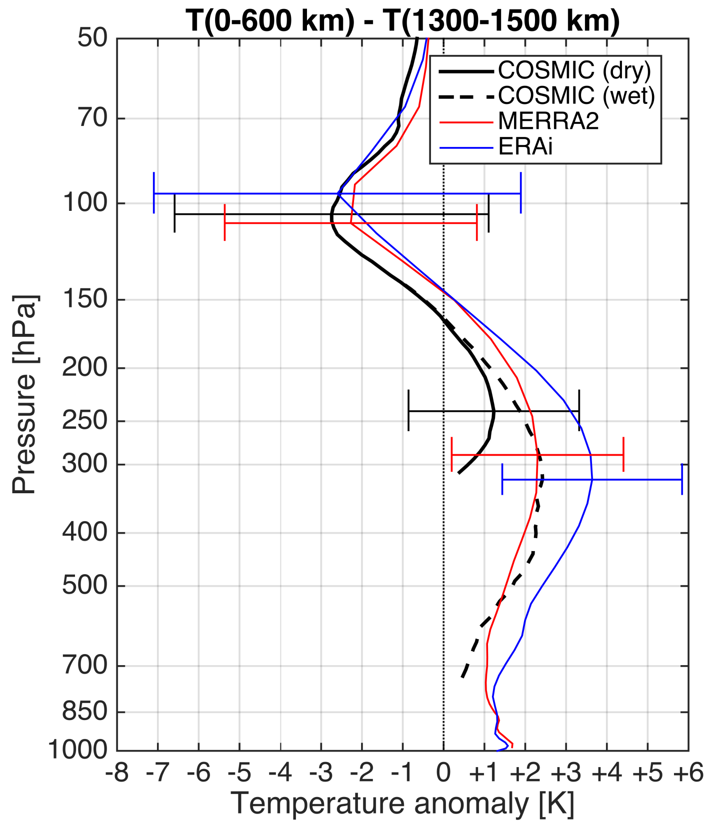

Figure 1.9: Average temperature anomaly inside the $600\,\mathrm{km}$ radius relative to the $1300-1500\,\mathrm{km}$ average, as a function of pressure. The error bars show $\pm$ 1 standard deviation of the mean at the levels where the largest absolute anomalies occur.

Figure 1.10 shows the thermal structure of TCs as observed from COSMIC and as captured by ERAi and MERRA-2. Notable differences include the magnitude of the tropospheric warm core, which is too large in reanalyses (especially in ERAi) and the extent of the tropopause layer cooling, which is too great in reanalyses after maximum intensity. The evolution of the thermal structure is further quantified in Figure 1.11. For the time being, the overall agreement between observations and reanalyses for the time period leading to maximum intensity is noted. Further discussion pertaining to these results will be laid out in Chapter 2. A remark about the average magnitude of the warm core and TC intensity: the warm core is on average more pronounced in ERAi than in MERRA-2, while TC intensities tend to be smaller in ERAi than they are in MERRA-2. This could be explained either by the near-surface wind field being wider in ERAi than in MERRA-2, or by the two reanalyses producing maximum horizontal winds on different pressure levels on average (in this case, determining intensity on a pressure level other than $925\,\mathrm{hPa}$ may be useful).

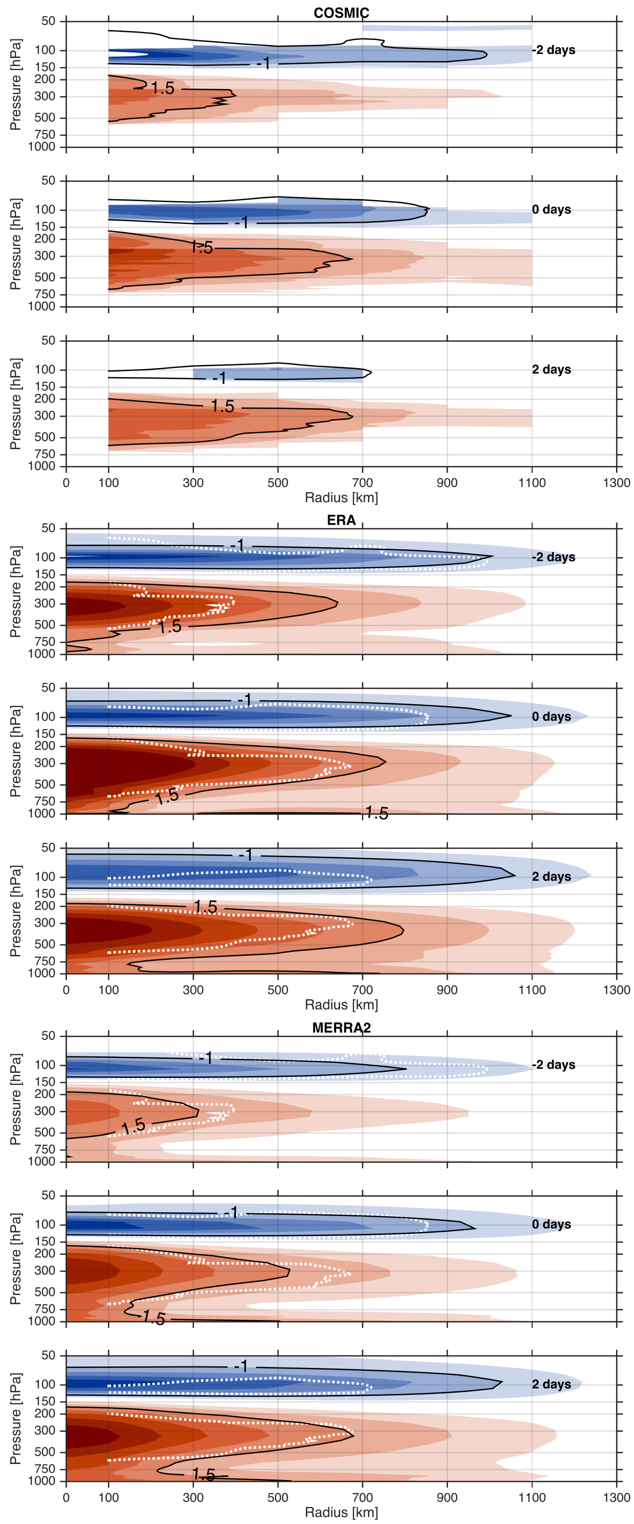

Figure 1.10: Average temperature anomaly as a function of radius and pressure for the 1-day time period centered 2 days before, at, and 2 days after maximum intensity. Anomaly is defined relative to the $1300 - 1500\,\mathrm{km}$ average. The $-1\,\mathrm{K}$ and $1.5\,\mathrm{K}$ anomaly contours from COSMIC are overlaid on the anomalies from ERAi and MERRA-2 as white dashed lines. Anomalies not significant to the 95% level (*t*-test) are shaded white.

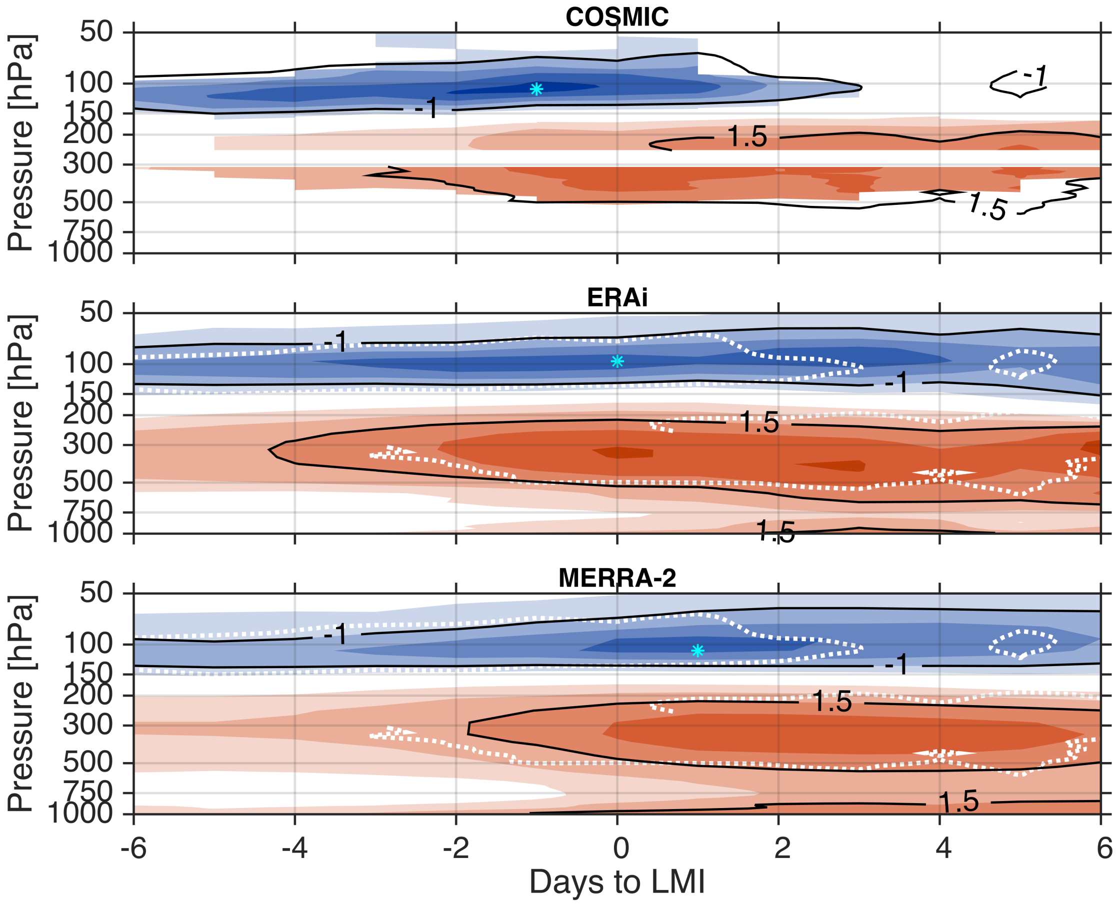

Figure 1.11: Average temperature anomaly as a function of time relative to maximum intensity and pressure. Anomaly is defined as the difference of the $0-600\,\mathrm{km}$ and the $1300-1500\,\mathrm{km}$ averages. The $-1\,\mathrm{K}$ and $1.5\,\mathrm{K}$ anomaly contours from COSMIC are overlaid on the anomalies from ERAi and MERRA-2 as white dashed lines. Anomalies not significant to the 95% level (t-test) are shaded white. Cyan asterisks locate the largest negative anomalies.

Chapter 2

Mechanisms for tropopause layer cooling

The observations of Chapter 1 lay out a path for analyzing the potential mechanisms causing tropopause layer cooling above TCs. First, the diabatic effect of clouds in the UTLS is considered (Section 2.1). The effect of the TC secondary circulation associated with the primary circulation is explored in Section 2.2.

Other mechanisms may generate cooling near the tropopause. One mechanism includes the adiabatic effect of updrafts that overshoot their level of neutral buoyancy. This mechanism is often put forward to explain TLC in the literature, however, there are several indications that this mechanism may only play a marginal role. Cooling of the tropopause is observed at large distances from TCs ($1000\,\mathrm{km}$). At these distances, overshooting deep convection is sparse, i.e., if cooling is indeed generated by overshooting, it must occur closer towards the TC center and be transported outwards. This goes against the typical wind field found in TCs (see Figure 2.18). Additionally, overshooting is relatively rare and weak in TCs, and should be expected to be compensated by turbulent mixing and subsidence warming on mesoscales. A modeling study by Fritsch and Brown (1982) shows that cooling from overshooting clouds generates subsidence above the cloud top, supporting the view that overshooting is an unlikely mechanism for mesoscale cooling of the tropopause layer. Lastly, overshooting cloud tops are difficult to observe due to their small size and ephemeral nature.

Another mechanism involves adiabatic expansion within gravity waves. This mechanism corresponds to a hydrostatic response to the tropospheric warm core: in order to fulfill the constraint that isobars be unperturbed at sufficiently large altitude above TCs, a compensating cooling must occur somewhere in the atmospheric column. Gravity waves generated by fast latent heat release propagate upward and outward from the convective source, triggering a wave-like response aloft. The temperature perturbations associated with these waves have previously been observed to locally maximize and produce cooling near the tropopause directly above deep convection. While individual gravity waves produce cooling and warming in alternation, gravity wave packets may interact and leave behind a residual circulation which has a net cooling effect. In order to determine the importance of this mechanism in TCs, the simulations in Section 2.2.2 may be used to quantify eddy terms (associated with gravity waves) in the equations of motion.

2.1 Diabatic cooling via cloud radiative processes

This section contains work that is under review (pending revisions) at *J. Clim.* The expected citation is Rivoire et al. (2020).

While the occurrence frequency of convective clouds decays with height nearly exponentially above 12 to $14\,\mathrm{km}$ in the tropics (Gettelman et al., 2002), convective regions greatly impact the radiative flux balance of the TTL (Thuburn & Craig, 2002; Q. Yang, Fu, & Hu, 2010). Additionally, deep convection within TCs has been described by proxy to reach the uppermost troposphere and penetrate the stratosphere more frequently than isolated convection (Romps & Kuang, 2009), particularly in the western North Pacific Ocean. It is therefore a reasonable expectation that sustained deep convection in TCs—among all marine deep convective systems—can have a disproportionately large impact on the chemical composition of the TTL (see Ray & Rosenlof, 2007) and therefore on the radiative flux balance of the TTL. Deep convective clouds exhibit longwave cooling near their top and shortwave heating below, which could also impact the radiative flux balance of the TTL. Closely associated with deep convection and TCs are cirrus clouds, which can detrain from the top of cumulonimbus as extensive anvils or form in situ via turbulent mixing (E. J. Jensen, Toon, Selkirk, Spinhirne, & Schoeberl, 1996). The longwave radiative impacts of cirrus occurring near the tropopause depend on the underlying atmosphere (Ackerman, Liou, Valero, & Pfister, 1988; Hartmann, Holton, & Fu, 2001): when the troposphere is clear, cirrus are generally expected to lead to warming by absorbing more upwelling longwave radiation from the surface than they emit near their top. When the troposphere is populated with stratiform, stratocumuliform, low, or thin clouds, the same is generally true and cirrus warm the tropopause. When the troposphere is populated with deep convective clouds, cirrus can cool the tropopause by emitting more longwave

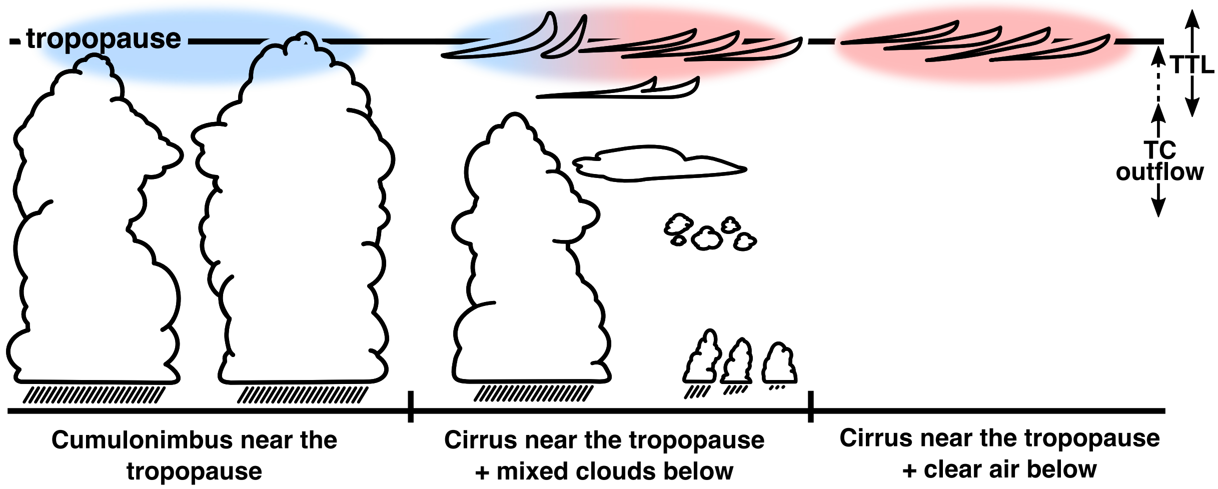

Figure 2.1: Schematic illustration of three typical cloud scenarios and associated qualitative longwave radiative flux divergence expected near the tropopause: blue for divergence (cooling), red for convergence (warming). Cumulonimbus are represented as tall, billowy shapes. Cumulus are represented as shallower billowy shapes. Cirrus are represented as upper-level, horizontally elongated shapes. Other shapes represent mid-level clouds (altostratus, nimbostratus, stratocumulus, stratus, altocumulus). The double arrows indicate approximate locations for the TTL and TC outflow layer.

radiation near their top than they absorb from the cold cloud tops below (see Hartmann et al., 2001). These effects are illustrated in Figure 2.1.

At present, quantitative knowledge of cloud vertical distribution in TCs remains limited, posing strong limitations for radiative computations (see Corti, Luo, Peter, Vömel, & Fu, 2005). Cloud boundaries are subject to large errors; for instance, cloud top heights estimated from infrared brightness temperature retrievals are subject to errors ~ 1 km due to varying cloud optical properties and to the presence of cirrus aloft that are difficult to distinguish from convective clouds using passive sensors alone (Hawkins, Turk, Lee, & Richardson, 2008). These caveats are alleviated by using the cloud classification product from Sassen, Wang, and Liu (2008) and radiative heating rates from Henderson, L'Ecuyer, Stephens, Partain, and Sekiguchi (2013), both of which are derived from the combination of CloudSat's radar and CALIPSO's[1] lidar retrievals, conferring their detection capability for optically thick as well as thin clouds (Sassen, Wang, & Liu, 2009). Data available near active TCs are compiled in the CloudSat TC overpass data set (Tourville, Stephens, DeMaria, & Vane, 2015). For the portion of the analysis relevant to quantifying TLC, high vertical resolution, high accuracy temperature retrievals from the Constellation Observing System for Meteorology, Ionosphere, and Climate (COSMIC) are used as in Rivoire et al. (2016, see Section 1.1).

The focus of the study is the tropical western North Pacific Ocean. Total temperature tendencies associated with TLC are first quantified using COSMIC data. Vertical profiles of longwave radiative heating associated with the cloud scenarios of interest (see Figure 2.1) are then characterized inside TCs. Lastly, the overall longwave radiative effect of clouds in TCs is quantified. A description of the compositing technique is provided in Section 2.1.1 along with further details about the data sets used. The results of the analysis are presented in Section 2.1.2 and discussed in Section 2.1.3.

2.1.1 Methods

Data come from two primary sources for this study: the CloudSat TC overpass data set, and the COSMIC Data and Archiving Center.

Cloud classification product

The cloud classification product (2B-CLDCLASS-LIDAR version R05) is derived from the combination of collocated spaceborne radar and lidar data, owing to CloudSat and CALIPSO flying the same orbit for extended periods of time with a separation time of only $\sim 8.5\,\mathrm{s}$. Data are given at the 240 m maximum vertical resolution of CloudSat's Cloud Profiling Radar (CPR) and with a $\sim 1.5\,\mathrm{km}$ horizontal resolution: to each radar volume corresponds one of eight cloud types determined using a fuzzy-logic-based algorithm. Generally speaking, cloud type (stratus, stratocumulus, altocumulus, cumulus, nimbostratus, altostratus, cumulonimbus, or cirrus) is determined using cloud features (reflectivity, water phase, temperature, height, vertical and horizontal extent,

[1]Cloud-Aerosol Lidar and Infrared Pathfinder Satellite Observations

homogeneity, precipitation) derived from the products listed in Section 2.1.1. Details of the method and algorithm are available in Sassen and Wang (2012) and in the algorithm release documentation (http://www.cloudsat.cira.colostate.edu).

Few data are available to evaluate the performance of the 2B-CLDCLASS-LIDAR product in terms of high, thin clouds detectable by lidar only. However, Sassen and Wang (2008) found their radar-only CloudSat cloud classification product (2B-CLDCLASS) to be in good agreement with cloud classification products created prior (from ground reports, see Hahn and Warren, 1999, and from the International Satellite Cloud Climatology Project, see Rossow and Schiffer, 1999). The radar-lidar cloud classification product is therefore expected to be in good agreement with other classification products, while improving the characterization of high, thin clouds.

The cloud scenarios described in Figure 2.1 are named CB (cumulonimbus reaching near the tropopause), MIX (cirrus near the tropopause and mixed clouds below), and CI (cirrus near the tropopause and clear air below). Cloud boundary heights from the 2B-CLDCLASS-LIDAR product are used proceeding as follows:

- The cloud top height of the uppermost cloud layer (cumulonimbus for CB, cirrus for CI and MIX) must be located within $1\,\mathrm{km}$ of the average height of the cold point tropopause, i.e., it must be located between $16\,\mathrm{km}$ and $18\,\mathrm{km}$ above sea level. All cases with clouds above $18\,\mathrm{km}$ are consequently excluded.

- For CB, there can only be cumulonimbus clouds in the column, and at least one cumulonimbus layer must be at least $10\,\mathrm{km}$ deep (this criterion is almost always met as cumulonimbus are classified as such according to their large vertical extent).

- For CI, there can only be cirrus clouds in the column, and cirrus must occur in one layer no thicker than $5\,\mathrm{km}$. Cases with thickness greater than $5\,\mathrm{km}$ are included in the MIX scenario.

- MIX includes all combinations of cloud types in any number of layers, as long as the uppermost cloud layer is classified as cirrus.

From a total of $264\,645$ retrievals located within $1000\,\mathrm{km}$ of active, intensifying TCs, $74\,067$ ($38\,\%$) contain no hydrometeors. Amongst the remaining $190\,578$ retrievals that do contain hydrometeors, the method classifies $6\,\%$ as CB, $30\,\%$ as MIX, and $2\,\%$ as CI. Approximately $9\,\%$ exhibit a cloud layer (of any cloud type) with its top between 16 and $18\,\mathrm{km}$ but which does not meet the criteria for either cloud scenarios. Less than $1\,\%$ of retrievals meet either cloud scenario criterion but are rejected because their uppermost cloud layer (cirrus or cumulonimbus that is) is located above $18\,\mathrm{km}$. Consequently, choosing a different near-tropopause layer than 16–$18\,\mathrm{km}$ has little effect on the results. The thickness criterion for the CI scenario ($5\,\mathrm{km}$) corresponds to the median geometric thickness of all isolated cirrus layers with their top between 16–$18\,\mathrm{km}$. Using this criterion allows to produce a large sample size and to eliminate the thickest cirrus layers for which the longwave radiative effects tend to maximize below the tropopause, i.e., cases that are not directly relevant to the impact of cloud radiative effects on the tropopause. Choosing a smaller thickness criterion (for instance $4\,\mathrm{km}$) does not impact the qualitative results and only reduces the size of the sample. The CI scenario could also be defined using a cloud optical thickness threshold for cirrus layers, instead of using a geometric thickness threshold. Doing so would confer the advantage of including in CI some cirrus layers that are optically thin but have varying geometric thickness. For the sake of compositing however, given the general correlation between geometric and optical thickness, this alternate method is not expected to impact the results. Additionally, the absence of comparable data sets for cloud optical thickness makes assessing uncertainties difficult.

Radiative heating rates

The "radar-lidar fluxes and heating rates" product (2B-FLXHR-LIDAR version R04) consists of vertically resolved radiative fluxes and heating rates derived from the combined CloudSat and CALIPSO data. Radiative fluxes and heating rates are given with the same resolution as the 2B-CLDCLASS-LIDAR product. Radiative fluxes are calculated using the Bugsrad radiative scheme (Fu & Liou, 1992; Stephens, Gabriel, & Partain, 2001) that models molecular scattering, gaseous absorption, and absorption and scattering by liquid water and ice water. Inputs to the radiative transfer model are:

- **Cloud locations** from the "radar-lidar cloud geometric profile" product (2B-GEOPROF-LIDAR, Mace et al. 2009), which is derived from radar reflectivity and lidar backscatter data.

- **Cloud properties** (ice and liquid water content, equivalent mass sphere effective radius of hydrometeors) determined using the "cloud water content (radar only)" product (2B-CWC-RO, Austin, Heymsfield, and Stephens, 2009) for clouds detectable by the CPR, the MODIS[2]-based "optical depth" product (2B-TAU) and colocated CALIPSO products (Trepte, Minnis, Trepte, Sun-Mack, & Brown, 2010) for clouds detectable by lidar only, and the "precipitation column" product (2C-PRECIP-COLUMN, Haynes et al., 2009).

- **Temperature, humidity, and ozone concentration profiles** from the European Centre for Medium-Range Weather Forecasts (ECMWF) analyses (ECMWF-AUX product).

- **Surface albedo and emissivity** data from the International Geosphere-Biosphere Programme global land surface classification (Townshend, 1992).

Longwave radiative fluxes alone are used for this study, leaving the shortwave radiative fluxes aside as they are known to suffer larger uncertainties (Henderson et al., 2013) and are not directly relevant to explaining the presence of cooling in the atmosphere.

The 2B-FLXHR-LIDAR product is an improvement of the 2B-FLXHR product (L'Ecuyer, Wood, Haladay, Stephens, & Stackhouse Jr, 2008), which did not include lidar data. Estimating uncertainties for the vertically resolved radiative flux products is difficult due to the lack of a similar data set. However, comparisons of top-of-atmosphere fluxes between the 2B-FLXHR-LIDAR and 2B-FLXHR products and the CERES[3] product show close correlation and show an improvement from 2B-FLXHR algorithm to the 2B-FLXHR-LIDAR algorithm (Henderson et al., 2013) due to the improved characterization of high, thin clouds undetectable with CloudSat's CPR alone. Global mean uncertainties from the inputs to the algorithm listed above were estimated by introducing

[2]MODerate resolution Imaging Spectroradiometer

[3]Clouds and the Earth's Radiant Energy System

perturbations to each input (Henderson et al., 2013): assumptions made for the effective radius of hydrometeors introduce errors of order 0.1 to $1\ \mathrm{W\,m^{-2}}$ to outgoing longwave radiation (OLR), which is comparable to uncertainties introduced by resolution related errors on cloud boundary (top and base) heights. For reference, mean OLR is $\sim 250\,\mathrm{W\,m^{-2}}$ above the western North Pacific Ocean, with $\sim 5\,\mathrm{W\,m^{-2}}$ contributed by high, thin clouds. Uncertainties on OLR introduced by errors in the tropospheric temperature and humidity profiles from the ECMWF-AUX products are estimated to be of order $1\,\mathrm{W\,m^{-2}}$. Although uncertainties associated with errors in ozone concentration profiles have not yet been estimated for the CloudSat products, results in Gettelman et al. (2004) and Birner and Charlesworth (2017) show that ozone is not a primary contributor to heating rates in the TTL. Additionally, ozone concentrations can be especially low in the TTL over the western North Pacific when deep convection transports air from the ozone-poor marine boundary layer (Gettelman et al., 2004).

The contribution of clouds (hydrometeors) to the radiative heating rates is referred to as the "cloudy-sky" term and is calculated as the difference between the "all-sky" term (the overall heating rate) and the "clear-sky" term (the contribution from gases like water vapor). Since the clear-sky radiative heating rates are not directly provided in the CloudSat data set, they are calculated from the clear-sky radiative flux profiles using:

$$HR = \frac{g}{c_p}\frac{dF}{dp}$$

where HR is the heating rate in degrees Kelvin per second, g is the gravitational acceleration ($\sim 9.81\,\mathrm{m\,s^{-2}}$), c_p is the specific heat capacity of dry air at constant pressure ($\sim 1005\,\mathrm{J\,K^{-1}\,kg^{-1}}$), p is the atmospheric pressure in Pascals (from the ECMWF-AUX product), and F is the radiative flux in watts per meter squared (from the 2B-FLXHR-LIDAR product) defined as the difference between the upwelling and downwelling radiative fluxes at each vertical level. The pressure derivative of the radiative flux is estimated numerically using finite differences.

COSMIC temperature retrievals

The data set described in Section 1.1.1 is used. As additional remarks, the refraction of radio waves emitted by GPS satellites and detected by low-orbiting COSMIC satellites includes a small contribution from ice water. However, given the small ice water content in high-altitude clouds retrieved by CloudSat and CALIPSO (10^{-3} to $10^{-2}\,\mathrm{g\,m^{-3}}$), this ice water contribution is expected to be 5 to 6 orders of magnitude smaller than the contribution of temperature and pressure, and is therefore neglected. The GPS radio-occultation technique does not provide vertical atmospheric soundings; rather, temperature retrievals are inclined and typically span $\sim 100\,\mathrm{km}$ horizontally from their top ($\sim 60\,\mathrm{km}$ above sea level) to their bottom. Since the region of interest in this study (~ 12–$20\,\mathrm{km}$) is relatively shallow, horizontal drift is negligible and therefore not taken into account.

Compositing philosophy and method

In this study, processes are quantified that are tied to the structure of TCs—structure which varies significantly from storm to storm. In order to eliminate this variability and draw conclusions that are broadly relevant to the robust features found in TCs, observations are composited from a large number of events. Compositing data also allows to alleviate the sparse nature of the COSMIC and A-train data sets. No individual storm is sampled by either platform with coverage sufficient to provide meaningful information regarding cloud processes and tropopause heights. Since the features observed are prone to produce heavily skewed distributions (e.g., cloud top heights, see Figure 2.2), compositing data based on the mean would yield skewed results. Instead, statistics are provided as the median, a more robust measure of central tendency here. Whenever appropriate, the median is supplemented with a robust measure of statistical dispersion chosen as the interquartile range (the 25th through 75th percentiles).

The compositing time period is 1 January 2007 to 17 April 2011. Both COSMIC and A-train radar-lidar products are available for this period. Radar-lidar products are scarcely available after 17 April 2011 due to changes in CloudSat's orbit initially caused by a battery anomaly. During the compositing time period, since satellites on the A-train flew a sun-synchronous orbit with an equator local crossing time of 1:30 am/pm (Stephens et al., 2002), the A-train products are biased toward the local time of observation. However, this is not expected to be problematic for the interpretation of the results since the diurnal cycle of convection is a relatively small source of variability in the distribution of convection in TCs when compared to sources of variability such as TC size, intensity, and convective asymmetries that do not exhibit diurnal characteristics (Knaff, Longmore, DeMaria, & Molenar, 2015; Knaff, Slocum, & Musgrave, 2019). Additionally, the local times of A-train equator crossing reasonably sample the convective extrema, both in terms of area covered and heights reached (Liu & Zipser, 2008).

The compositing region is the tropical portion of the western North Pacific Ocean (0–$25°$N, 100–$180°$E). As mentioned earlier, the western North Pacific most frequently generates TCs with deep convective clouds reaching the TTL and penetrating the stratosphere (Romps & Kuang, 2009). The western North Pacific also accounts for roughly a third of TCs globally (Neumann, 1993) and is a good candidate for collecting a large data sample and produce robust composites. Indeed, a total of 102 TCs formed virtually year-round during the 2007–2011 time period, with January, February and March (August, September and October) being the months with lowest (highest) TC activity. In order to limit the influence of extratropical processes associated with large gradients of sea surface temperatures (Reynolds & Smith, 1995), ambiguous tropopause heights and large gradients of tropopause temperatures (Seidel et al., 2001), and large magnitudes of deep-layer wind shear, data are excluded when located poleward of $25°$N or when associated with TCs which center is located poleward of $25°$N. Data are also excluded when located over land.

Data are collected in the vicinity of intensifying TCs based on best track locations and intensities from the ATCF (Sampson & Schrader, 2000, see Section 1.1.1 for details). The radiative heating rates and cloud classification products are directly composited along the spatial dimensions (radius, altitude). Calculating temperature tendencies from COSMIC temperature retrievals requires the use of a time dimension; here time relative to the time of maximum intensity calculated from the ATCF best tracks for each TC. This time dimension preserves the chronology of TC life stages about maximum intensity, that is, intensification and weakening. Since the coldest clouds (highest, by proxy) occur during intensification and warm rapidly after maximum intensity (see Figure 1.2 or Rivoire et al., 2016), the study is focused on the intensification period of TCs. Since TCs reach their maximum intensity near $18°$–$20°$N in the western North Pacific, removing the weakening period from the composites also allows to reduce biases that occur where data are collected only on the equatorward side of the TC center when best tracks near the northern edge of the compositing region ($25°$N).

2.1.2 Results

Cloud distributions

The findings of Romps and Kuang (2009) about overshooting convection in TCs relied on reanalysis data sets and proxies available at the time, both of which suffer known biases and resolution limitations (which the authors discuss). Prior literature on the topic (e.g., Alcala & Dessler, 2002; Cairo et al., 2008) also suffers limitations in terms of hydrometeor detection above the oceans. It seems appropriate to provide updated statistics relevant to deep convective clouds, especially comparing cloud top heights for deep convective clouds that are associated with TCs versus those that are not. Figure 2.2 provides such a comparison using cloud top heights from the 2B-CLDCLASS-LIDAR product. Cloud top heights are collected within a subregion of the tropical western North Pacific climatologically encompassing most tracks and tropical cyclogenesis events. The difference between the two distributions clearly indicates that deep convection reaches higher altitudes when associated with TCs (i.e., within $200\,\mathrm{km}$ of TCs). The median deep convective cloud top height outside TCs is $1.5\,\mathrm{km}$ lower than inside TCs. Half of all clouds inside TCs reach above $17\,\mathrm{km}$, which happens to nearly correspond to the median height of the tropopause ($16.9\,\mathrm{km}$, see Section 2.1.2). One cannot say conclusively that these clouds penetrated the local tropopause; doing so would require colocated cloud top and tropopause height data. However, this result indicates that deep convective clouds have more potential to penetrate the stratosphere inside TCs than outside TCs, consistent with the results of Romps and Kuang (2009).

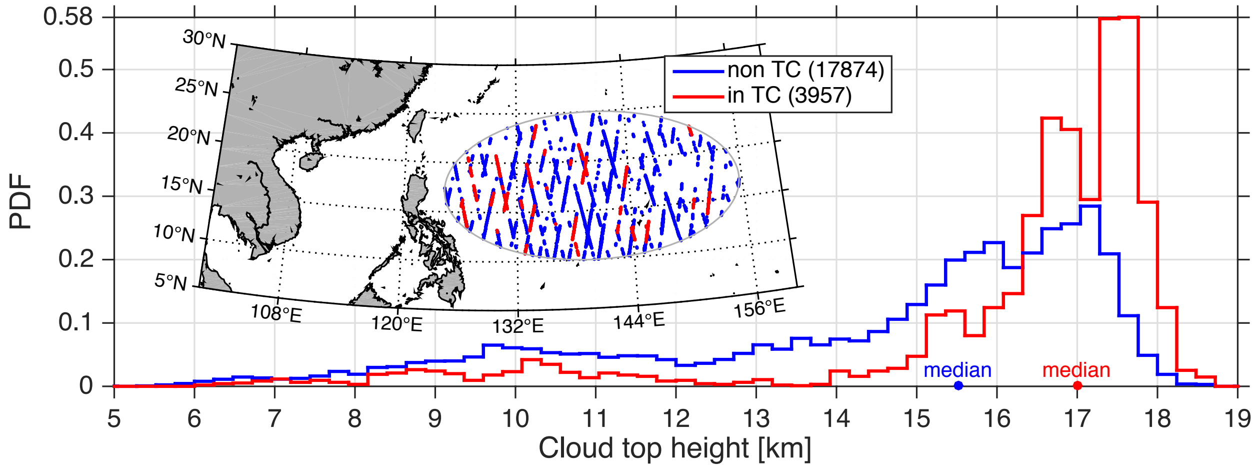

Figure 2.2: Histograms of deep convective cloud top heights in the region of the tropical west Pacific indicated on the map for 1 January 2007–17 April 2011. Retrievals located within $200\,\mathrm{km}$ of active TCs are indicated in red. Retrievals not associated with active TCs are indicated in blue. The number of samples is indicated in the legend.

As previously mentioned, knowledge of the vertical distribution of clouds is still lacking in TCs, especially in terms of individual cloud types. The 2B-CLDCLASS-LIDAR product from the TC overpass data set provides an opportunity to quantify the frequency of occurrence of cumulonimbus, cirrus, and other cloud types with unprecedented detail. These results are shown in Figure 2.3. Convective regimes broadly consistent with the known structure of TCs (see Frank, 1977) can be identified. The eyewall region corresponds to the local maximum of cumulonimbus occurrence frequency inside the 100-km radius, extending to near-tropopause altitudes and associated with a local minimum in cirrus occurrence frequency. Inner rainbands are visible between $100 - 225\,\mathrm{km}$ with median cloud top heights above $15\,\mathrm{km}$ and an interquartile range extending to lower altitudes than for the eyewall region. The outer spiral rainband region between $225 - 500\,\mathrm{km}$ is characterized by median cloud top heights above $14.5\,\mathrm{km}$ and a large interquartile range. Outside $500\,\mathrm{km}$, the median cloud top height varies significantly and the total cloud cover decreases, consistent with suppressed or sporadic convection.

In much of the TTL (14–$18.5\,\mathrm{km}$) and at all radii, cirrus and cumulonimbus account for over $80\,\%$ of the total cloud cover (Figure 2.3c). Qualitatively speaking (from Figure 2.1), it is reasonable to expect longwave cooling of the tropopause in the eyewall region due to the frequent

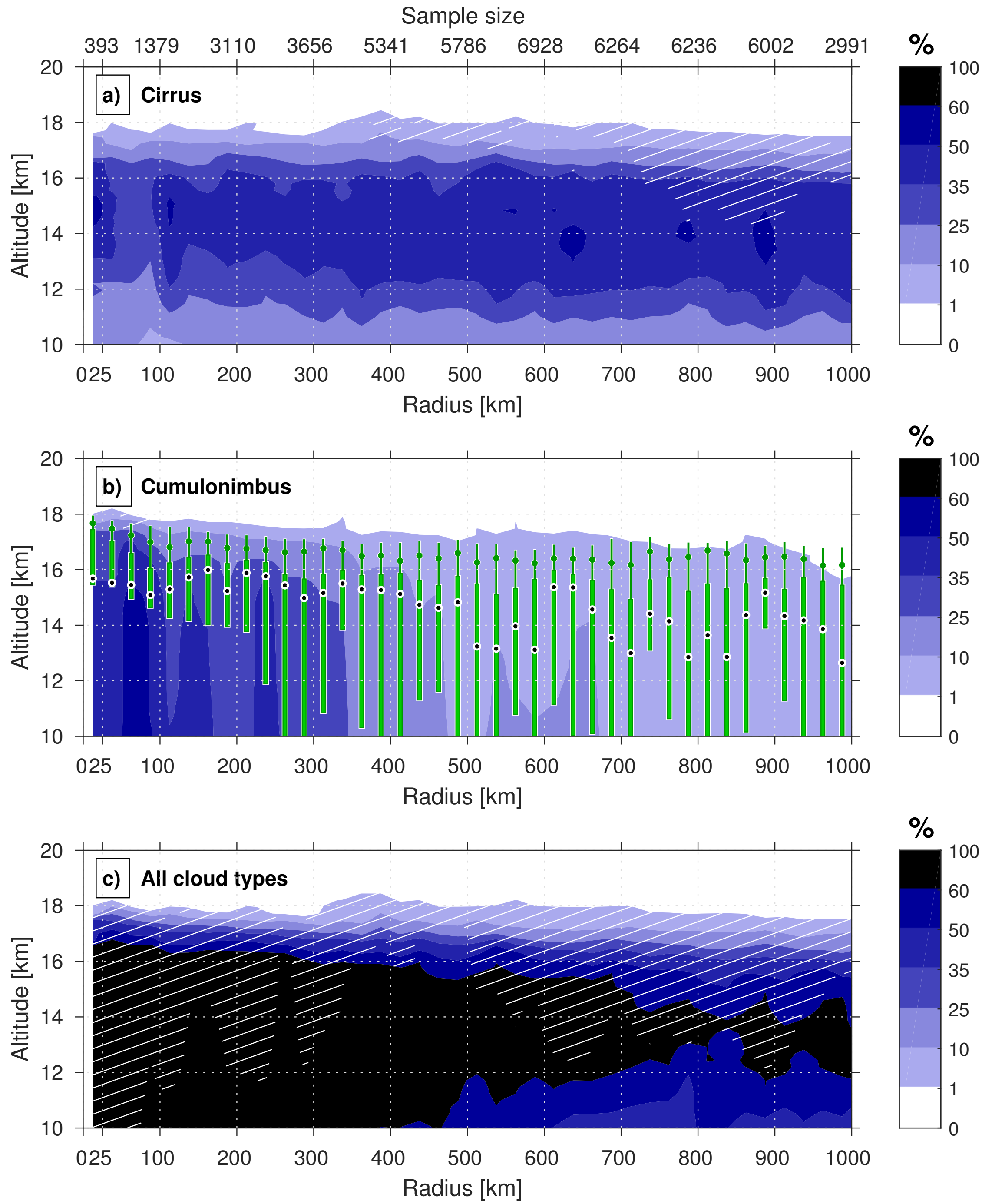

Figure 2.3: Frequency of occurrence of **a)** cirrus, **b)** cumulonimbus, and **c)** any cloud type, expressed at each radius and altitude as the percentage of all available 2B-CLDCLASS-LIDAR data that contain hydrometeors classified as either cloud type. The white hatching indicates where **a)** cirrus, **b)** cumulonimbus, **c)** cirrus and cumulonimbus account for at least $80\,\%$ of the total cloud fraction. Green boxplots show statistics of the cloud top height for cumulonimbus: the median (circled dots), the interquartile range (rectangles), and the 90th percentiles as small green circles on vertical lines that extend to the 99th percentile. The horizontal resolution is $25\,\mathrm{km}$. Sample size has been linearly interpolated to a regular grid for clarity.

presence of optically thick convective clouds. At larger radii, the presence of high-altitude cirrus above a rapidly decreasing cumulonimbus cover can also be qualitatively expected to produce longwave warming near the tropopause. Both these effects are quantified in Section 2.1.2.

Tropopause layer cooling derived from COSMIC temperature retrievals

Next, the temperature tendency corresponding to TLC is quantified. Figure 2.4a shows the total temperature tendency as a function of radius and altitude. The lower stratosphere exhibits a cooling rate of order $1\,\mathrm{K\,d^{-1}}$ on horizontal scales $\sim 1000\,\mathrm{km}$, with a maximum amplitude found just above the median tropopause inside the $250\,\mathrm{km}$ radius. The upper troposphere exhibits a warming of slightly smaller amplitude with a maximum amplitude at small radii near $15\,\mathrm{km}$ altitude. The median tropopause height varies by $\sim 300\,\mathrm{m}$ (16.7–$17\,\mathrm{km}$) over the range of radii shown, and its interquartile range extends from 16.3 to $17.4\mathrm{km}$. Its time dependency is of order $100\,\mathrm{m\,d^{-1}}$, associated with cooling $\sim 0.5\,\mathrm{K\,d^{-1}}$ (Figure 2.4b). The height of the tropopause within TCs is expectedly more variable than the height of the climatological tropopause (for which the interquartile range is 16.6–$17.2\,\mathrm{km}$). Tropopause heights are slightly smaller than the climatological median ($16.9\,\mathrm{km}$) except at small radii. Note that for the time period following maximum intensity, the median tropopause heights within TCs are slightly larger than the climatological median.

The determination coefficient (R^2; hatching in Figure 2.4a) gives a general idea of the robustness of the signal. Another way to quantify the statistical spread is to produce composites with random resampling of the data set (bootstrapping). This alternative method (not shown for concision) provides nearly identical results and shows that the spread is largest at small radii at all altitudes (due to smaller sample sizes) and at large radii in the lower stratosphere (likely due to the influence of the extratropical stratosphere near the edge of the domain of interest).

Radiative effect of the CB, MIX, and CI cloud scenarios

With total temperature tendency estimates in hand, the contributions of cloud radiative effects from the three cloud scenarios that impact the tropopause (CB, MIX, CI) are quantified. Figure 2.5 shows the typical cloud type profiles, cloudy-sky longwave heating rates, and clear-sky longwave

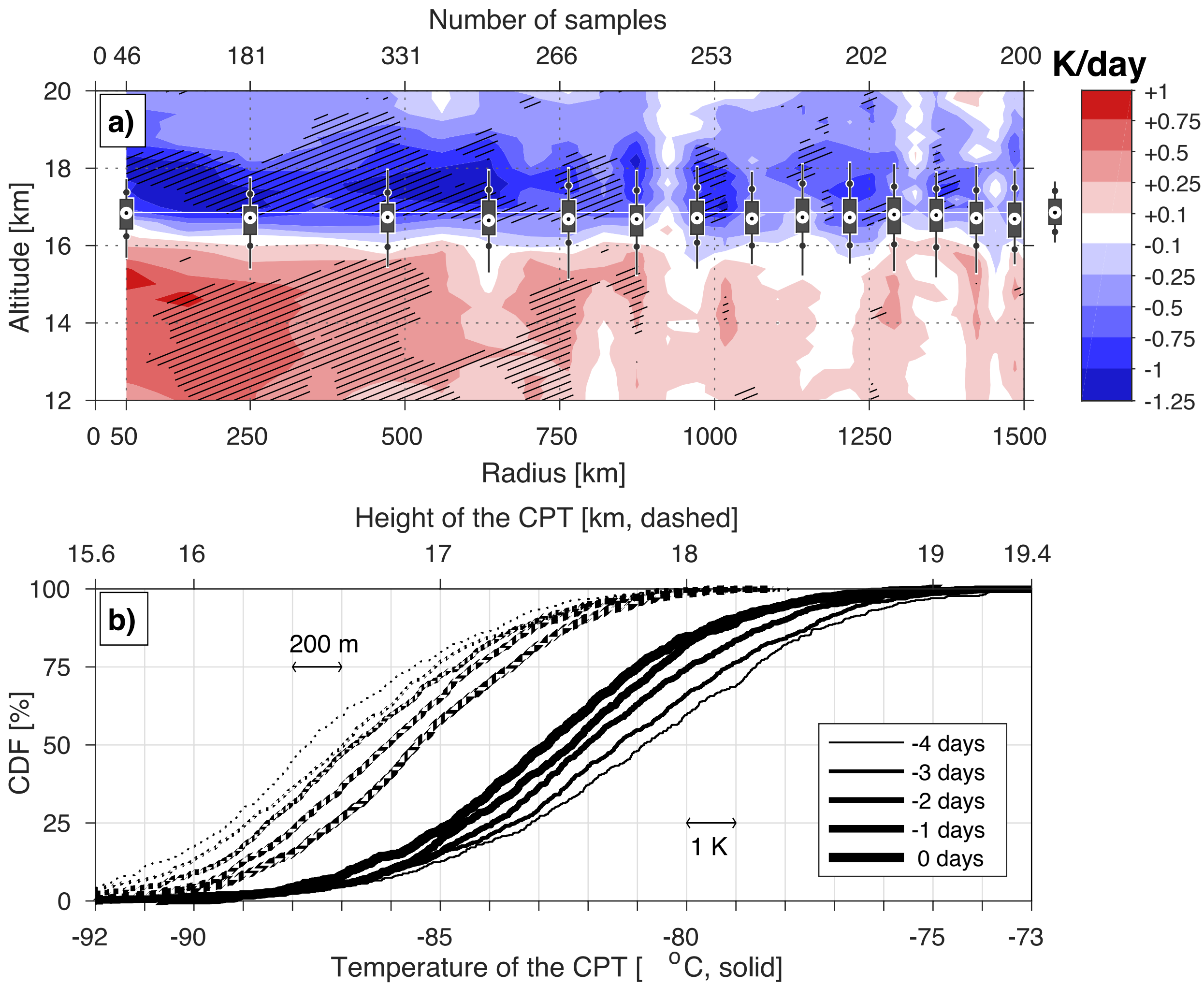

Figure 2.4: a) Temperature tendency in degrees Kelvin per day, defined at each radius and altitude as the slope of the linear regression between the median temperature and time (relative to maximum intensity). Hatching indicates tendencies for which the determination coefficient R^2 of the regression exceeds 0.9 in absolute value. Boxplots show the median height of the tropopause (circled dots) with rectangles showing the interquartile range, whiskers extending from the 1st to the 99th percentiles, and small circles indicating the 10th and 90th percentiles. The white, thin horizontal line emphasizes the median height of the climatological tropopause between 0–$1500\,\mathrm{km}$ $(16.9\,\mathrm{km})$, for which statistics are provided in the boxplot outside the main axis. The vertical resolution is $200\,\mathrm{m}$. The horizontal resolution is a function of radius so as to homogenize the sample size between radial bins and is $100\,\mathrm{km}$ $(30\,\mathrm{km})$ at the $250\,\mathrm{km}$ $(1500\,\mathrm{km})$ radius. Sample size has been linearly interpolated to a regular grid for clarity. **b)** Cumulative distribution functions of the height (dashed) and temperature (solid) of the cold point tropopause (CPT) between 0–$1000\,\mathrm{km}$, as a function of time relative to the time of maximum intensity.

heating rates corresponding to each cloud scenario. The MIX scenario is separated into MIX– and MIX+ depending on the average longwave heating rate between 16–$18\,\mathrm{km}$, see panel a). The expected qualitative longwave effects illustrated in Figure 2.1 are verified: within the $16-18\,\mathrm{km}$ layer, the CB scenario produces cooling, the CI scenario produces warming, and the MIX scenario produces cooling (MIX–) when clouds below are mostly deep convective and warming (MIX+) when clouds below are stratocumuliform or stratiform in nature. The vast majority of MIX cases are composed of cirrus above $10\,\mathrm{km}$ (over $80\,\%$ of them for MIX+). CB produces cooling of order 1–$2\,\mathrm{K\,d^{-1}}$ near the tropopause and $2-10\,\mathrm{K\,d^{-1}}$ just below. CI produces warming up to $\sim\!2.5\,\mathrm{K\,d^{-1}}$ below the tropopause. MIX– can produce cooling up to $\sim\!1\,\mathrm{K\,d^{-1}}$ and MIX+ warming up to $\sim\!2.5\,\mathrm{K\,d^{-1}}$ just below the tropopause.

The CB and MIX– scenarios produce radiative heating rates of the same order of magnitude as the total temperature tendencies seen at the tropopause and just below. However, neither scenario produces radiative heating rates that are large enough to explain the temperature tendencies seen above the tropopause. Considering the shortwave contribution (not shown), which is equal to or larger than zero, the net radiative effect of these cloud scenarios seems unlikely to explain TLC. One potential exception is the occurrence of the CB scenario during nighttime (when shortwave heating is zero). The clear-sky radiative heating rates (Figure 2.5c) change sign near $15\,\mathrm{km}$ and show a warming up to $0.5\,\mathrm{K\,d^{-1}}$ near the tropopause, consistent with previous results showing absorption of longwave radiation by elevated ozone concentrations in the lower stratosphere and a negligible contribution from water vapor (e.g., Gettelman et al., 2004). The rest of the troposphere displays the typical $\sim\!2\,\mathrm{K\,d^{-1}}$ clear-sky cooling rate.

As can be expected from the radial structure of cloud occurrence frequencies in Figure 2.3, different cloud scenarios tend to occur at different radii within TCs: the median radius of occurrence for the CB, MIX–, MIX+ , and CI scenarios is 328, 506, 608, and $637\,\mathrm{km}$, respectively. This has bearing on the overall effect of clouds near the tropopause (see Section 2.1.2).

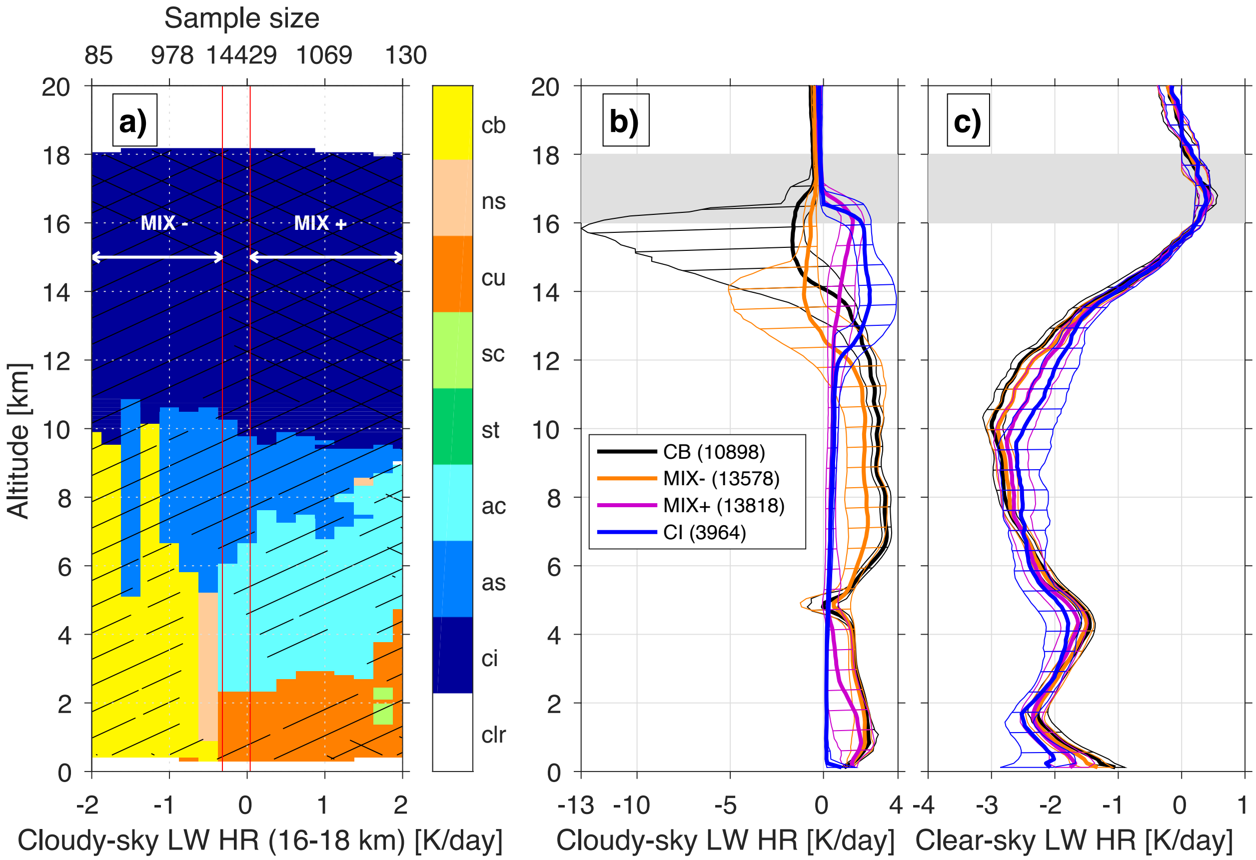

Figure 2.5: a) Most frequent cloud type encountered at each vertical level for the MIX scenario (clr: clear, ci: cirrus, as: altostratus, ac: altocumulus, st: stratus, sc: stratocumulus, cu: cumulus, ns: nimbostratus, cb: cumulonimbus). Black single hatching (double hatching) is used where the cloud type displayed is present at least $40\,\%$ ($80\,\%$) of the time. The abscissa is the cloudy-sky longwave heating rate averaged within the 16–$18\,\mathrm{km}$ layer; the 25th ($-0.31\,\mathrm{K\,d^{-1}}$) and 75th ($0.045\,\mathrm{K\,d^{-1}}$) percentiles are indicated by two vertical red lines. These two values are used to separate the MIX cases which produce cooling (MIX–) or warming (MIX+) between 16–$18\,\mathrm{km}$. Cases that lie outside $\pm 2\,\mathrm{K\,d^{-1}}$ are not included and represent less than $1\,\%$ of the data set. Sample size has been linearly interpolated to a regular grid for clarity. **b)** Median (thick lines) and interquartile range (hatched) cloudy-sky longwave heating rates, and **c)** clear-sky longwave heating rates for CB, CI, MIX–, and MIX+. The legend indicates the number of samples in each scenario. The 16–$18\,\mathrm{km}$ layer is shaded in gray.

Gross radiative effect of clouds in the TTL

Lastly, the overall effect of clouds is quantified in the TTL, i.e., the weighted effects of the cloud scenarios analyzed earlier, plus the contribution from other cloud scenarios that were not isolated due to their relatively low occurrence frequency or complex nature. Figure 2.6a shows the median all-sky longwave heating rates as a function of radius and altitude, and Figure 2.6.b shows the cloudy-sky contribution. Statistics of the tropopause height are overlaid, as well as total temperature tendency outlines to facilitate visual comparison with the results from Figure 2.4. The results are broadly consistent with the radial distribution of the cloud scenarios in Section 2.1.2; the strongest cooling occurs near the center of the storm where the CB and MIX– cases have most frequently been observed, and cooling of smaller amplitude occurs at larger radii where the MIX+ and CI cases are more frequent.

From Figure 2.6b it is clear that clouds associated with TCs have the potential to produce radiative cooling in the TTL. Inside the main convective region of TCs (i.e., inside $\sim 300\,\mathrm{km}$), longwave cloud radiative heating rates are dominated by the occurrence of cumulonimbus (including the CB scenario); warming within cloud occurs below $14\,\mathrm{km}$ and cloud top cooling is visible between 14 and $16\,\mathrm{km}$ exhibiting magnitudes of the same order as TLC. Outside the main convective region (and over $\sim 90\,\%$ of the area shown in the composites), longwave cloud radiative heating rates are about 5 times smaller than TLC around the tropopause. In this region, longwave warming occurs in much of the lower part of the TTL, in part corresponding to the occurrence of upper tropospheric cirrus as shown in Figure 2.3a. When adding to these features the clear-sky longwave contribution, the picture changes drastically (Figure 2.6a). Cloud top cooling is only strong enough above the main convective region to counteract the tendency of clear-sky radiation to warm the upper part of the TTL.

Since the shortwave contribution is essentially zero during the nighttime, Figure 2.6.a represents the net effect of radiation during the nighttime. During the daytime, one must account for the positive contribution of shortwave absorption by clouds and the atmosphere, which should be expected to be largest near the top of the main convective region. The shortwave heating rates

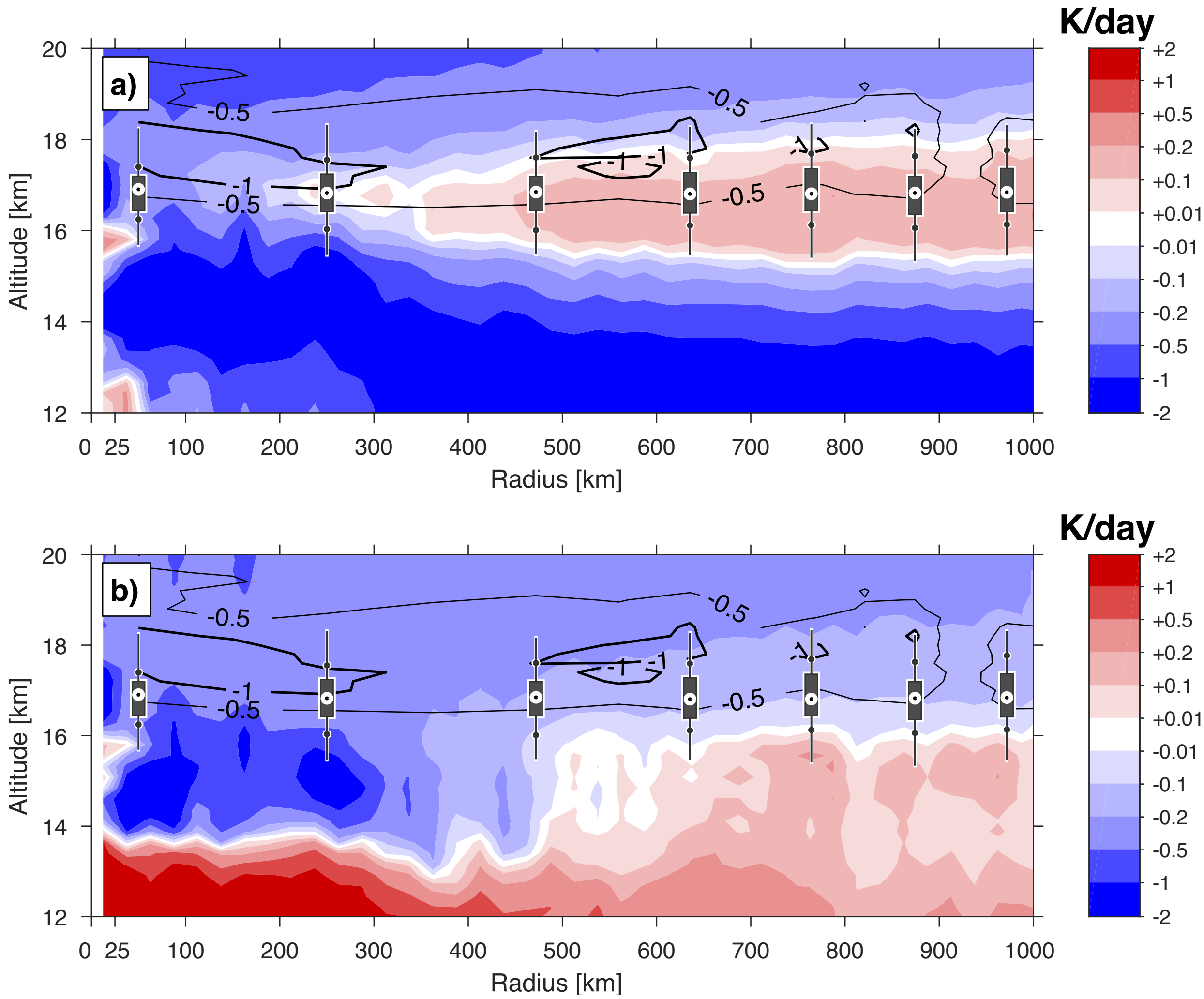

Figure 2.6: **a)** All-sky, median longwave heating rates and **b)** cloudy-sky contribution. The boxplots (tropopause heights) and -0.5 and $-1\,\mathrm{K\,d^{-1}}$ contours (temperature tendencies) are reproduced from Figure 2.4a. The sample size is the same as in Figure 2.3.

from the radar-lidar products (not shown) suggest that the absorption of shortwave radiation can largely offset longwave cooling and lead to net warming near the top of the main convective region, while a net cooling remains in the upper troposphere outside the main convective region. Near the tropopause, these heating rates suggest net daytime warming at all radii, i.e., it is possible that the diurnal cycle of insolation acts in turn to increase and decrease TLC above the main convective region. This raises the question of the impact of the diurnal cycle on cloud-TLC feedbacks.

2.1.3 Discussion and conclusions

This study addressed mesoscale processes that act in synergy with synoptic scale processes in TCs. Using the ability of A-train satellites to detect thick and thin clouds in the upper troposphere and lower stratosphere, cloud type and cloud top height distributions were produced within TCs (Figure 2.2 and Figure 2.3). Temperature retrievals from COSMIC were also used to derive tropopause height statistics within TCs (Figure 2.4). Lastly, radiative flux products from the A-train satellites were used to provide quantitative evidence supporting the view that longwave cloud radiative effects only account for a fraction of the negative temperature tendencies observed on synoptic scales near the tropopause above TCs. Results (Figure 2.5 and associated discussion) suggest that the all-sky, net (longwave and shortwave) radiative effect is a warming of the tropopause and upper TTL over much of the area covered by TLC. Given that the potential for convection to reach and penetrate the stratosphere is greatest in the western North Pacific (Romps & Kuang, 2009), this general finding is expected to hold for other oceanic basins (although this has not yet been verified). This finding is also expected to be valid for deep convection outside TCs, since deep convection does not reach near-tropopause altitudes outside TCs as often as it does inside TCs. While some cloud scenarios significantly affect the TTL below the tropopause, their effect above the tropopause is too small to explain the temperature tendencies there. It is suggested that other mechanisms must play a predominant role in producing TLC, particularly outside the main convective region of TCs.

A few nuances are worth mentioning that should be kept in mind when interpreting the results. The potential impact of cloud radiative effects on the TC outflow layer (in the upper troposphere below the tropopause) is to be interpreted carefully. Azimuthally averaged composites are only relevant to the symmetrical component of the TC structure, which can be rather small for the outflow where it is channeled in an asymmetric fashion by the large-scale environment (outside the $400\,\mathrm{km}$ radius, see Black and Anthes, 1971). Further data and higher sampling frequency are needed in order to alleviate this limitation. Other limitations related to the CloudSat data products include uncertainties in the heating rates linked to the assumption of hydrometeor sphericity (Z. Zhang et al., 2009) and inaccuracies in the estimates of meteorological variables and active species (ozone, water vapor). Resolving these limitations will require, broadly, better instrumentation and more accurate global analyses. Lastly, non sun-synchronous data will be needed in order to understand the effect of the diurnal cycle on convection and on the TTL.

2.2 Adiabatic cooling via the secondary circulation

This section considers the effect of the secondary circulation that develops in TCs under the constraint of gradient wind balance of the primary circulation. In theory, the TC secondary circulation for the balanced vortex may contract horizontally as a TC intensifies and expand vertically into the lower stratosphere. No observations (to my knowledge) are available that may demonstrate whether this occurs in nature. The approach is as follows: Section 2.2.1 provides first clues about the extent of the secondary circulation in TCs using reanalysis data sets as in Chapter 1. Section 2.2.2 expands on these first clues by using high-resolution TC simulations from CM1 to derive a heat budget in the UTLS.

2.2.1 Insight from reanalysis data

The same compositing technique as in Chapter 1 is used here. Since reanalysis data sets are able to capture TLC, they must capture processes through which lifting occurs near the tropopause that lead to adiabatic cooling. Given the nature of reanalyses, theses processes exclude any non-hydrostatic process which would be inconsistent with balanced dynamics. Note that cloud radiative processes in the UTLS were not evaluated in reanalysis data sets due to the poor representation of the cloud field and the fact that cloud occurrence frequency is near zero above $200\,\mathrm{hPa}$ in reanalyzed TC-like vortices.

Figure 2.7 and Figure 2.8 show the basic structure of TCs within reanalyses, including the horizontal and vertical wind fields. The features found in TCs are qualitatively represented, albeit stretched horizontally. The primary circulation has a radius of maximum winds near $250\,\mathrm{km}$, and the outflow layer extends well beyond $2000\,\mathrm{km}$. Maximum updrafts occur inside the radius of maximum wind, consistent with observations. The secondary circulation reaches above the tropopause ($\sim 100\,\mathrm{hPa}$) at all radii, suggesting that TLC in reanalyses is consistent with adiabatic cooling in the secondary circulation. However, some unrealistic features cast doubt as to the realism of this general picture: the low-level inflow layer deepens with radius and time, and is several kilometers deep after maximum intensity. The secondary circulation breaks down after maximum intensity, leaving behind a troposphere-wide weak outflow.

In order to further test whether TLC responds to the secondary circulation, a TLC metric is defined and reanalyzed meteorological fields are regressed onto it. The metric is defined as the difference in average temperature between the $0-200\,\mathrm{km}$ and the $1000-1500\,\mathrm{km}$ radius ranges, at the $100\,\mathrm{hPa}$ level. This definition captures a representative value for the large-scale radial gradient of tropopause-level temperature. Motivation for this simple analysis comes from the poor correlation that exists between simple metrics defined for the amplitude of the warm core and of TLC (see Figure 2.9). Poor correlation suggests that processes other than thermal wind balance modulate TLC. Figure 2.10 shows the regression of the vertical wind field onto the TLC metric, i.e., the change in the vertical wind field needed at each radius and pressure level to decrease the amplitude of TLC by $1\,\mathrm{K}$. Figure 2.11 shows the same regression, but onto the azimuthal wind field. Together these figures indicate that increasing TLC magnitudes are associated with increasing upward vertical motion and cyclonic tangential wind at small radii and increasing anticyclonic tangential wind in the outflow layer at large radii.

2.2.2 Tropical cyclone simulations

In order to assess the realism of the secondary circulation in the UTLS as captured by reanalyses, TC simulations with higher resolution may be run. Since reanalysis data sets are 3-dimensional, 3-dimensional simulations should ideally be ran. However, the features of interest being located near the tropopause, they are subject to incessant gravity wave activity from the convective sources in the troposphere below. Gravity waves produce oscillations in the density field of the stratosphere with amplitudes of order $1-10\,\mathrm{K}$, leading to large temperature variability in the

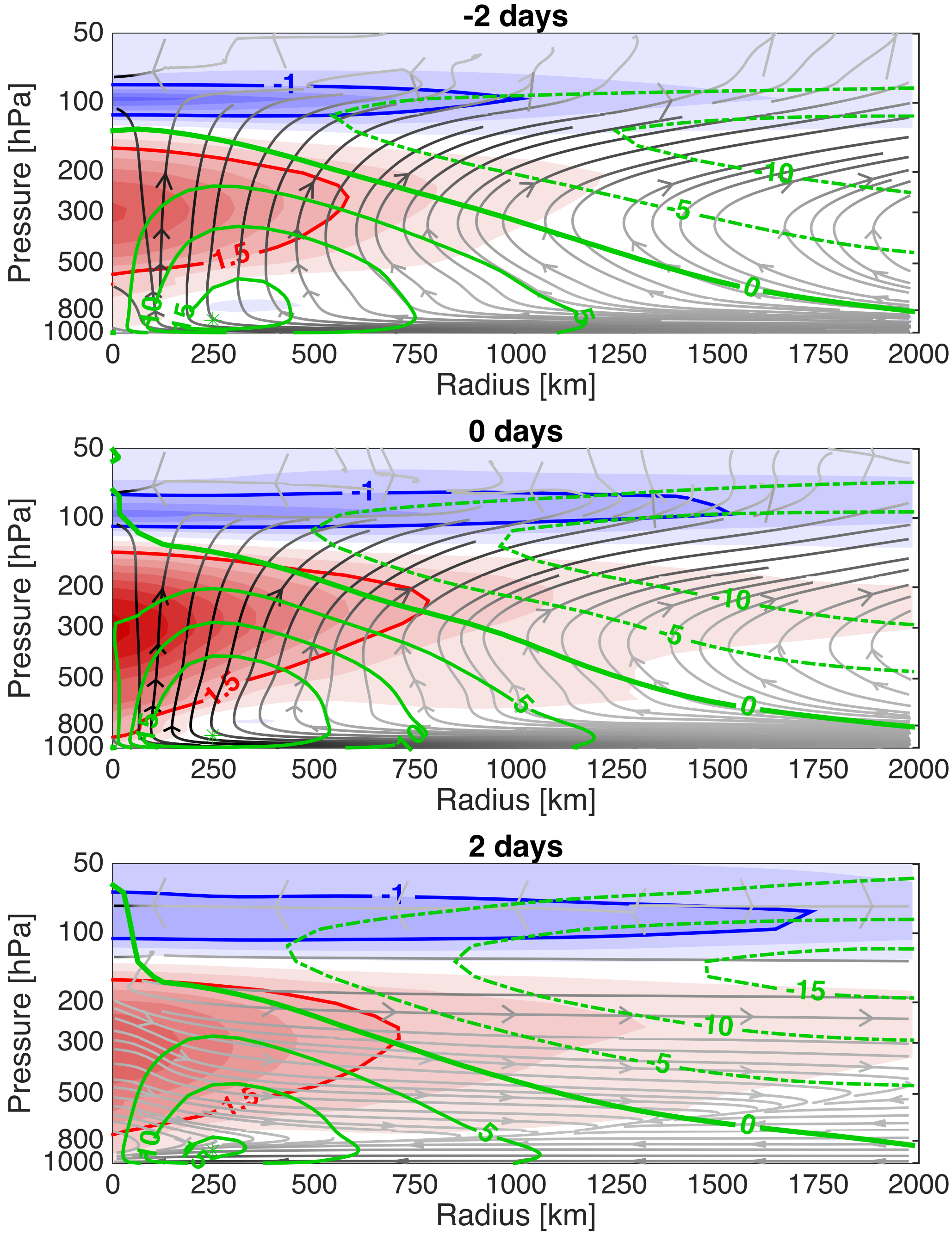

Figure 2.7: Average temperature anomalies relative to climatology (shading every $0.5\,\mathrm{K}$ with the $-1\,\mathrm{K}$ and $+1.5\,\mathrm{K}$ contours specified), secondary circulation (streamlines with arrows), and tangential wind (green contours every $5\,\mathrm{m\,s^{-1}}$, solid for cyclonic winds and dashed for anticyclonic winds) as a function of radius and pressure at -2, 0, and +2 days from lifetime maximum intensity. Data from ERAi. The streamlines are color coded to reflect the magnitude of the secondary circulation (gray for small magnitudes and black for the largest magnitudes).

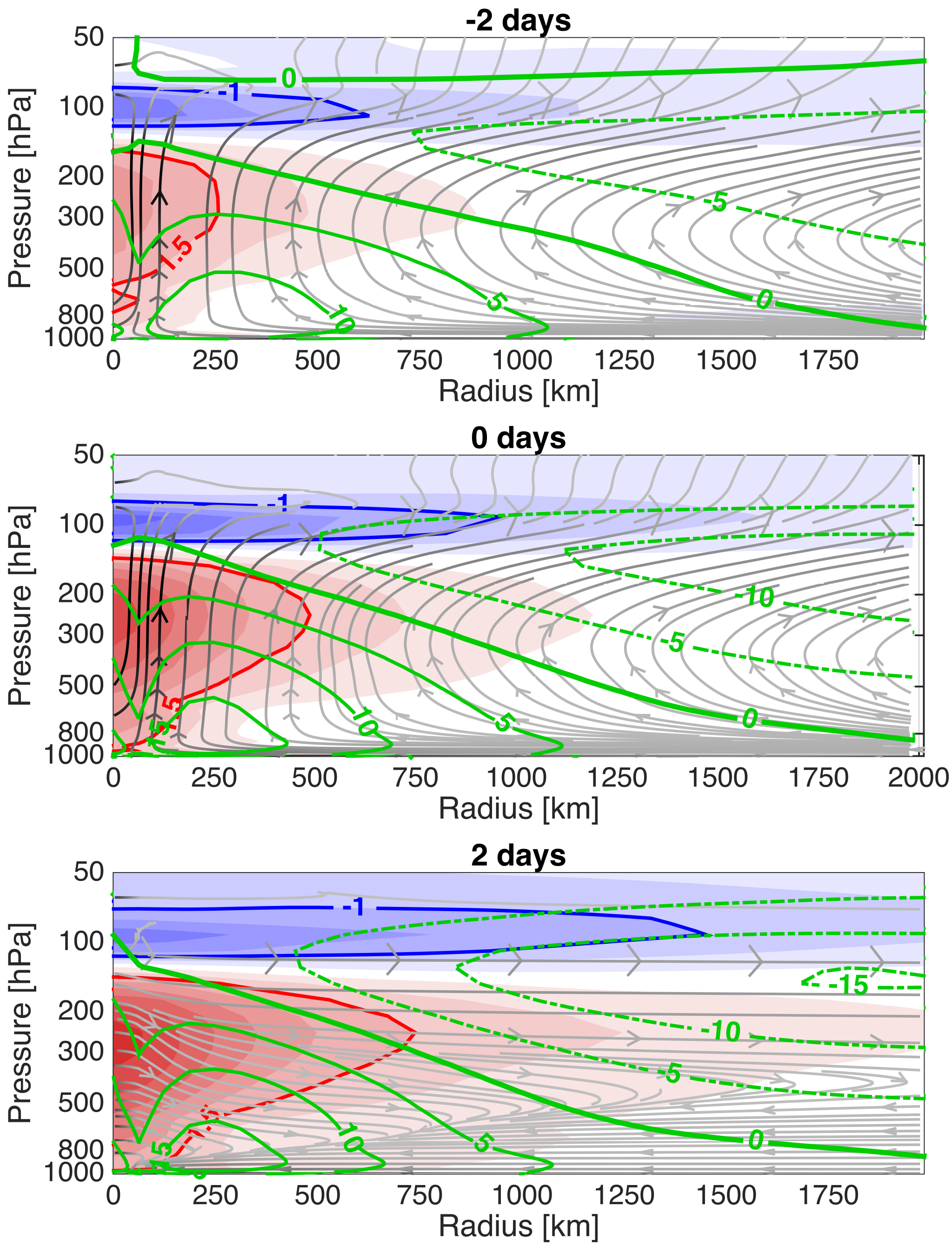

Figure 2.8: Same as Figure 2.7 but for MERRA-2.

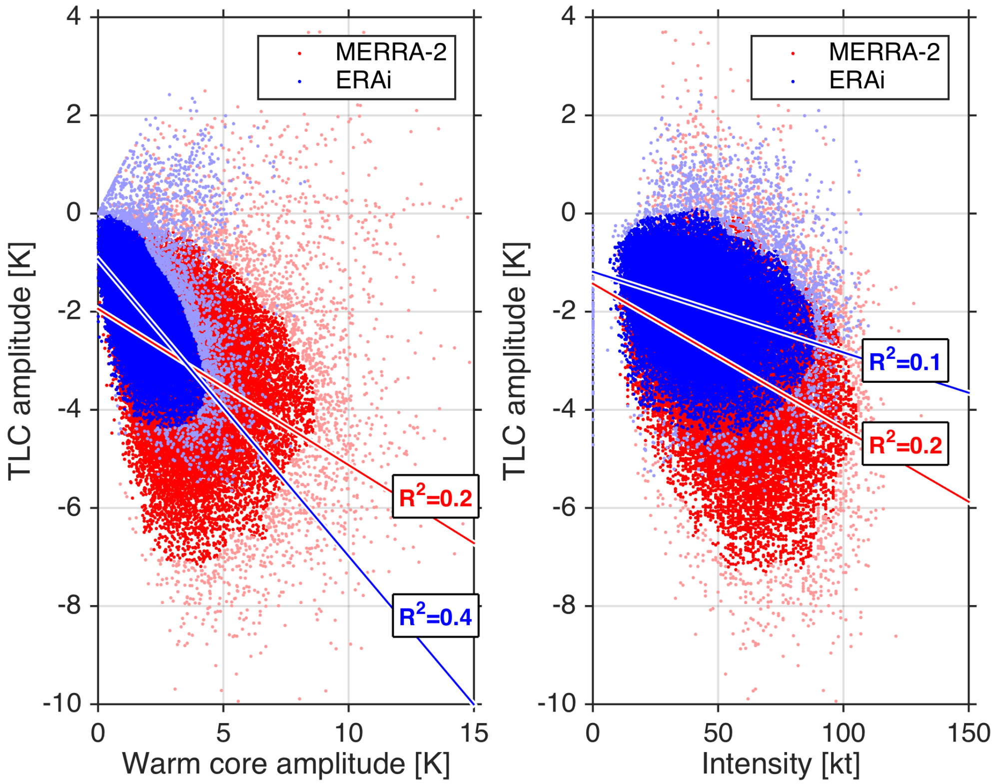

Figure 2.9: Scatter plot for the amplitude of the warm core and of TLC (left), and for the intensity and TLC (right). The amplitude of the warm core is defined as the difference in temperature between $0-200\,\mathrm{km}$ and $1000-1500\,\mathrm{km}$ averaged between the $200\,\mathrm{hPa}$ and $800\,\mathrm{hPa}$ levels. The amplitude of TLC is defined in the same way, but along the $100\,\mathrm{hPa}$ level. Outliers (light colors) are defined as points located outside the $2.5\,\%$ isoline of the normalized PDF, and are not included in the regression lines.

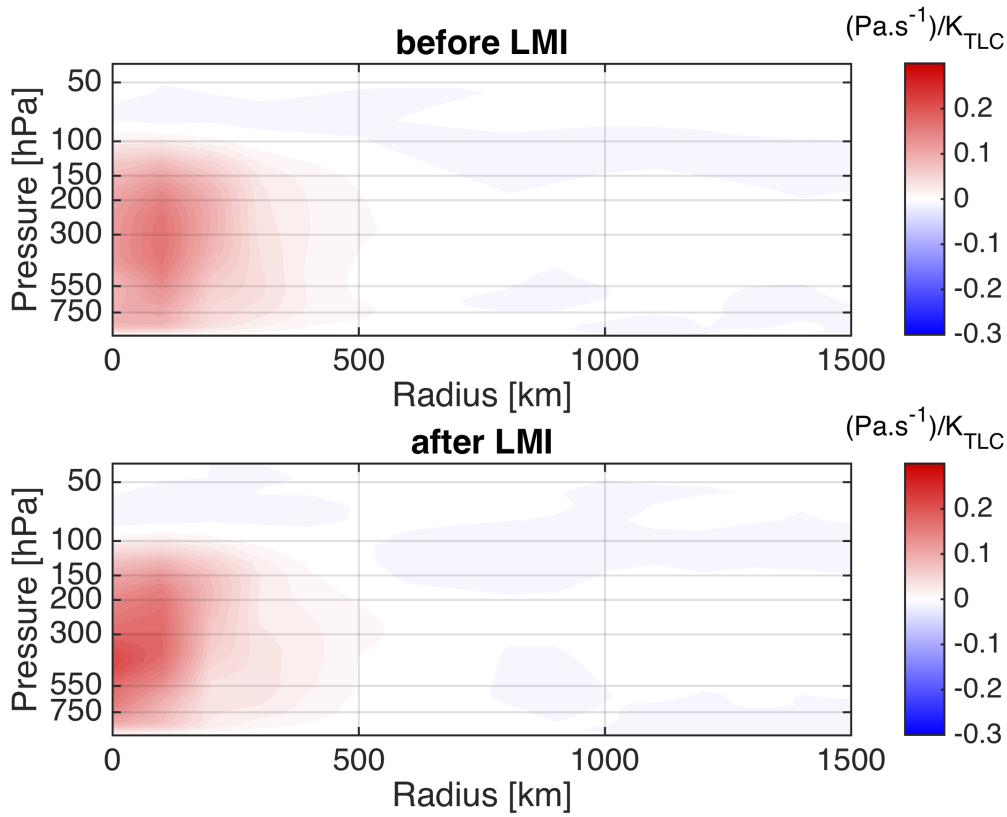

Figure 2.10: Slope of the linear regression between the TLC metric defined in Figure 2.9 and the vertical wind field. Red shades indicate regions where the vertical upward wind velocity decreases when the magnitude of negative temperature anomalies associated with TLC decreases.

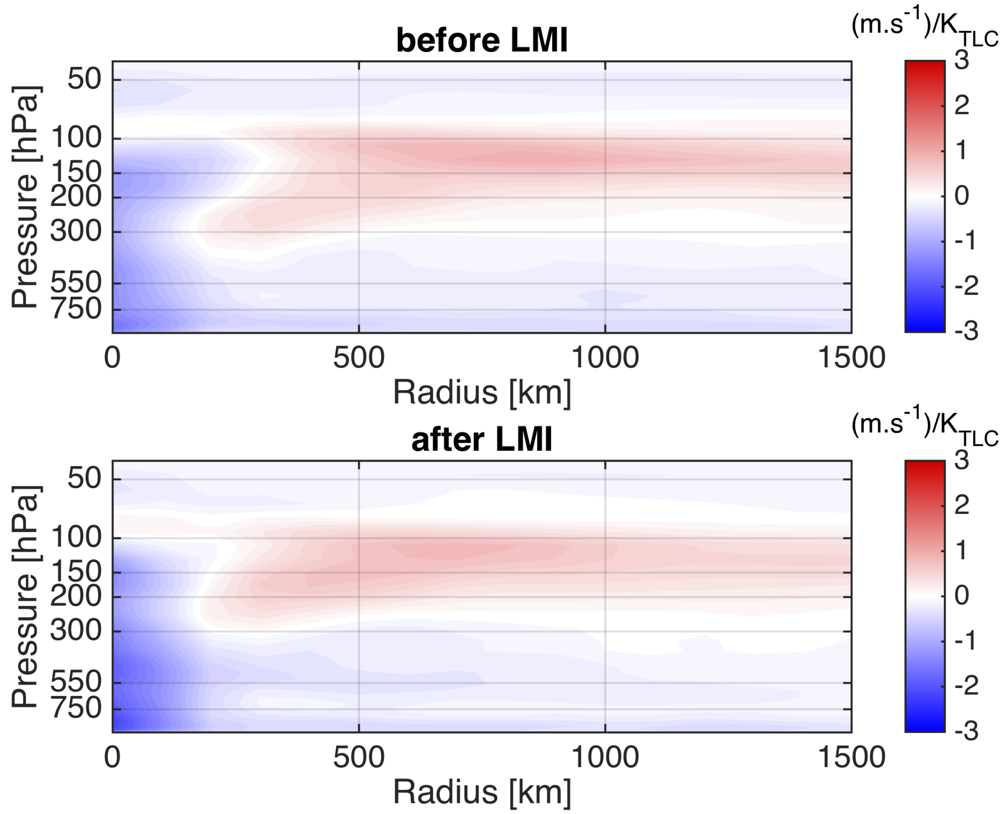

Figure 2.11: Slope of the linear regression between the TLC metric defined in Figure 2.9 and the azimuthal wind field. Red (blue) shades indicate regions where the anticyclonic (cyclonic) component of the horizontal wind field decreases when the magnitude of negative temperature anomalies associated with TLC decreases.

tropopause layer. For this reason, it is preferable that many simulations be run with varying initial conditions, so that one may analyze the temperature of the tropopause layer averaged over many simulations. For the sake of computational expense, and to simplify the framework so that axial asymmetries and associated complex processes be minimized, 2-dimensional simulations are run. Simplifying the real world to a 2D plane being a considerable leap in idealization, it is important to discuss known differences between 2D and 3D simulations.

It is generally accepted that axial asymmetries in TCs work to reduce the intensification rate and the mature TC intensity (B. Yang, Wang, & Wang, 2007, see also Bryan and Rotunno, 2009). In 2D simulations, asymmetries (upper-level asymmetric outflow jets, mesovortices in the eye and eyewall, vortex Rossby waves, boundary layer roll vortices, etc.) are viewed as turbulence and their effect is represented by model parameterizations. The results presented here should therefore be compared to 3D simulations to see whether they are valid in 3D and how they may be nuanced. One process leading to asymmetries is the barotropic breakdown of the unstable ring vortex (Michalke & Timme, 1967; Rotunno, 1979; Schubert et al., 1999). The ensuing potential vorticity redistribution process weakens the tangential wind speed (Schubert et al., 1999). From this view point, asymmetries result in the down-gradient mixing of momentum and buoyancy, i.e., asymmetries are akin to a diffusive process which reduces the intensification rate and maximum intensity of 3D tropical cyclones, compared to their 2D counterparts. Additionally, given that the release of latent heat by deep convection in 2D simulations occurs along concentric cylinders, it may be expected that 2D simulations are too efficient at producing buoyancy fluxes (Persing, Montgomery, McWilliams, & Smith, 2013)—although, at least in the boundary layer, the vertical profile of heating has the same shape in 2D and 3D simulations (Moeng, McWilliams, Rotunno, Sullivan, & Weil, 2004). Although 2D simulations are expected to produce TCs with a faster spin-up and larger maximum intensity, 2D simulations have generally been found to capture the structure and evolution of the azimuthally-averaged 3D simulation (Anthes, Trout, & Rosenthal, 1972; K. A. Emanuel, 1991). Insight may therefore be gained using 2D simulations, especially once a comparison with 3D simulations is made.

Other processes modulate the structure and dynamics of TCs in the UTLS, including the diurnal cycle of radiative fluxes. This includes an increase in the rate of tropical cyclonegenesis (Nicholls & Montgomery, 2013), and pulsating in the cirrus cloud field (Browner, Woodley, & Griffith, 1977; Lajoie & Butterworth, 1984; Muramatsu, 1983; Steranka, Rodgers, & Gentry, 1984) and rainfall (Shu, Zhang, & Xu, 2013) in association with pulsating in the deep convection near the storm center (Hobgood, 1986). However, these effects are all superposed to the mean effect of the secondary circulation and add layers of complexity not necessary for the time being. The diurnal cycle of radiation is therefore not included in the simulations. The role of radiation itself is also simplified by representing it as a simple Newtonian relaxation term which relaxes the temperature profile towards the initial state with a time constant of $12\,\mathrm{h}$ (as in Rotunno & Emanuel, 1987). This term mainly ensures that average temperature does not increase in the model domain and leaves out the effects of cloud radiative processes, which results in Section 2.1.2 suggest do not alone control the TC structure in the UTLS.

Updating the Dunion (2011) moist tropical profile

TC simulations are oftentimes run in a thermodynamic environment set by the Dunion average moist tropical profile (Dunion, 2011). This profile is given with $\sim 1\,\mathrm{km}$ resolution in the troposphere, degrading to $2-4\,\mathrm{km}$ near the tropopause. Since the profile was derived by averaging several years of rawinsonde data along pressure levels, the characteristics of the tropopause in the Dunion profile are necessarily affected by variability in the UTLS. An initial sounding is created which preserves the sharpness and temperature of the tropopause: a tropopause-relative coordinate is used to average COSMIC temperature retrievals over the same area of the Caribbean Sea and north Atlantic Ocean and over the same time period as in Dunion (2011). The averaged, tropopause-relative temperature profile is then assigned the average height of the tropopause, as in Birner (2006). The temperature given by the Dunion profile is used up to $11\,\mathrm{km}$, altitude above which dry COSMIC temperature retrievals provide a high-resolution, accurate depiction of the tropical UTLS. The moisture profile is the same as the Dunion profile up to the height of the average tropopause, and a climatological value of $4\,\mathrm{ppmv}$ (Birner & Charlesworth, 2017) is assigned

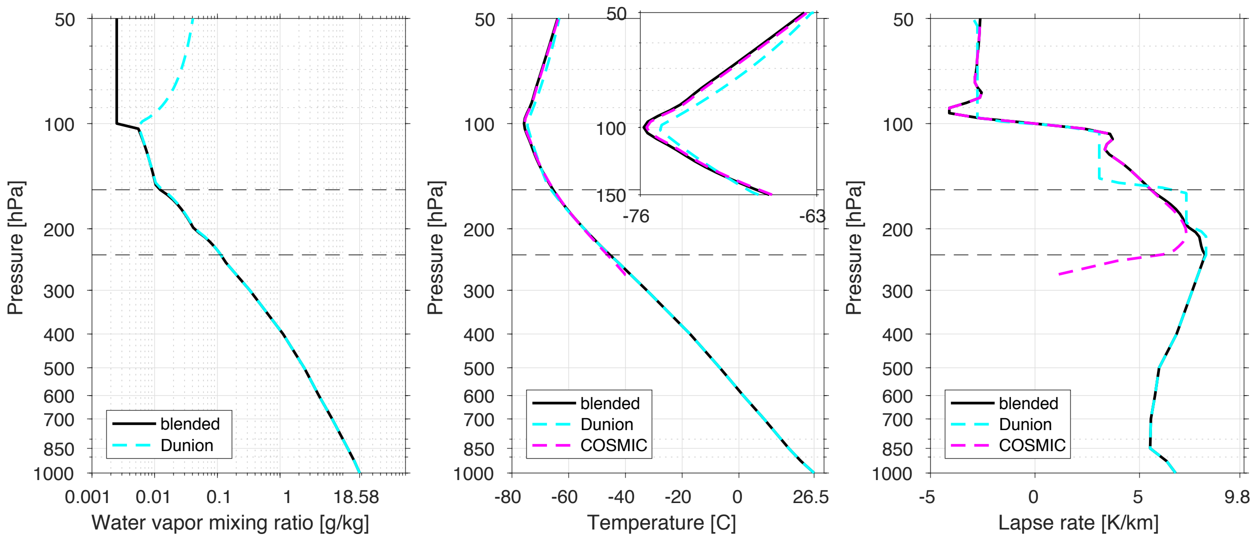

Figure 2.12: Water vapor mixing ratio, temperature, and lapse rate of the Dunion profile, average COSMIC Caribbean profile, and the blended "COSMIC-Dunion" profile. The blending region $(11 - 14\,\mathrm{km})$ is indicated by two dashed, horizontal lines.

in the stratosphere (rather than the relatively elevated value of the Dunion profile). This ensures that the constraints set by the environment in the lower troposphere and boundary layer are the same as if using the Dunion profile, while including a more realistic thermal structure in the upper troposphere and stratosphere. Near $11\,\mathrm{km}$, temperature differences between the Dunion and COSMIC-derived profiles are small enough that both data sets may be blended together with the following simple method: between $11 - 14\,\mathrm{km}$, the average lapse rate is defined as:

$$\Gamma(z) = \alpha \Gamma_{Dunion}(z) + (1 - \alpha)\Gamma_{COSMIC}(z)$$

with

$$\alpha = \frac{14 - z}{14 - 11}$$

(z in km) and the average temperature is calculated from the blended lapse rate. Figure 2.12 shows the Dunion and COSMIC average profiles, as well as the blended result.

In order to compare the effects of updating the UTLS of the Dunion (2011) profile, 30 simulations are run with the Dunion profile and 30 are run with the COSMIC-Dunion profile. The following model setup is used:

Table 2.1: Model setup description for the 2D tropical cyclone simulations

Domain top	:	$35\,\mathrm{km}$
Domain outer radius	:	$1500\,\mathrm{km}$
Horizontal resolution	:	$1\,\mathrm{km}$ inside $64\,\mathrm{km}$ radius stretched to $15\,\mathrm{km}$ at $1500\,\mathrm{km}$
Vertical resolution	:	$10\,\mathrm{m}$ near the ground, stretched to $150\,\mathrm{m}$ near $2\,\mathrm{km}$
Sponge layer	:	Newtonian damping towards base state between $28-35\,\mathrm{km}$
	:	with e-folding time $300\,\mathrm{s}$
Vertical boundary condition	:	rigid walls, free slip
Radiation scheme	:	simple relaxation term based on Rotunno and Emanuel (1987)
Initial state	:	– fixed $301.15\,\mathrm{K}$ sea surface temperature (no slab)
	:	– $\sim 0.1\,\mathrm{K}$ random potential temperature anomalies
	:	– Rotunno and Emanuel (1987) analytic vortex

The two initial soundings only produce small differences in the maximum intensity of the simulated TCs (Figure 2.13a). However, larger differences exist in the wind and cloud structure (Figure 2.13b-c and Figure 2.14). Particularly notable is the statistically significant upward and outward shift in the secondary circulation when using the COSMIC-Dunion profile, which is visible in the two rightside panels in Figure 2.14, as well as in the cloud field (Figure 2.13c). The shift in the secondary circulation is expected, given that the tropopause in the COSMIC-Dunion profile is slightly colder than that in the Dunion profile. Differences in the tangential wind field in the eyewall in Figure 2.14 correspond to the slightly larger intensification rates produced by the COSMIC-Dunion profile for model integration time period $2-4\,\mathrm{days}$ (Figure 2.13a) (the following statements are to a large extent valid for the $6-8$ days or $8-10$ days time period, when simulated TCs reach a quasi steady state in terms of intensity. The time period $2-4$ days was chosen to illustrate changes that exist during the intensification of simulated TCs, the model time period which has a real-world equivalent, as opposed to the quasi steady state). The elevated moisture content of the stratosphere in the Dunion initial sounding leads to the in situ formation of stratospheric clouds above the eye and eyewall (Figure 2.13c), via gravity wave activity. These clouds are most visible in the Dunion runs (they do not form in the COSMIC-Dunion runs) once the simulated TC reaches a quasi-steady state. Note that the simulated cloud cover in the TTL is much lesser than observed (Figure 2.3).

Structure of the UTLS

The simulations run using the COSMIC-Dunion initial sounding exhibit slight shifts in the UTLS structure (perhaps improvements, if one considers that a more realistic initial sounding always improves the representation of the real phenomenon). The first step towards analyzing potential mechanisms for tropopause layer cooling is to evaluate whether tropopause layer cooling exists in the model, and if it exhibits similarities to its real-world equivalent. Figure 2.15 shows the average thermal structure of the simulated TCs as an anomaly relative to the initial sounding. Cooling around the tropopause is clearly visible on large horizontal scales. The evolution of the thermal structure shows that cooling is initially generated near $15\,\mathrm{km}$ and that it is displaced or generated at increasing altitudes with time, eventually found on either side of the tropopause. This behavior is consistent with observations in Figure 1.5. The magnitude of positive, tropospheric temperature anomalies below the cooling increases with time as the cooling becomes more pronounced, also consistent with Figure 1.5. Lastly, the magnitude of the cooling is $\sim 1-2\,\mathrm{K}$, close to values reported in Figure 1.3.

After a few days of integration, negative temperature anomalies are seen propagating down from the lower stratosphere toward the tropopause. These anomalies may be the product of ducted gravity waves: convectively generated gravity waves propagate upward in the troposphere, and part of them penetrate the stratosphere, while another part is reflected into the troposphere. Waves that penetrate the stratosphere see their magnitude increase rapidly (and vertical wavelength decrease rapidly), as a result of the large static stability of the stratosphere. These waves may interact with each other and with the boundary conditions in the stratosphere, as well as with the bottom of the sponge layer where partial reflection may occur. When the distance between the wave source and

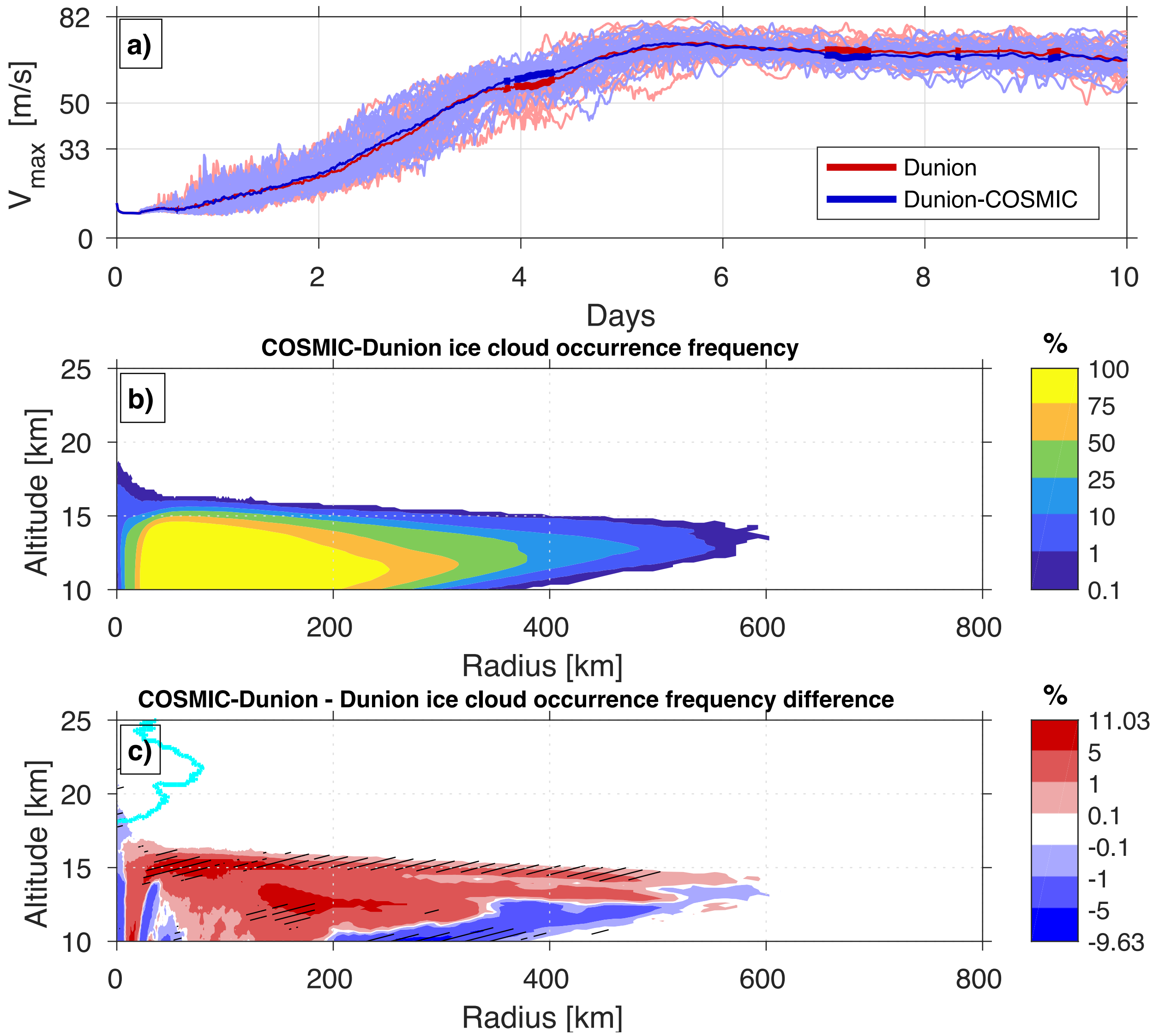

Figure 2.13: **a)** Maximum tangential wind velocity as a function of time for each ensemble member (thin, light lines) and for the ensemble average (thicker lines). Differences between the ensemble-averaged velocities of the Dunion and COSMIC-Dunion runs that are statistically significant to the $95\,\%$ level (using Student's *t*-test) are highlighted as thick segments. **b)** Frequency of occurrence of ice clouds (defined as ice water content $\geq 1 \times 10^{-6}\,\mathrm{kg\,kg^{-1}}$) for the Dunion-COSMIC runs, and **c)** average difference with the Dunion runs. The cyan contour in **c)** indicates the presence of in situ clouds at long integration times when using the Dunion initial sounding.

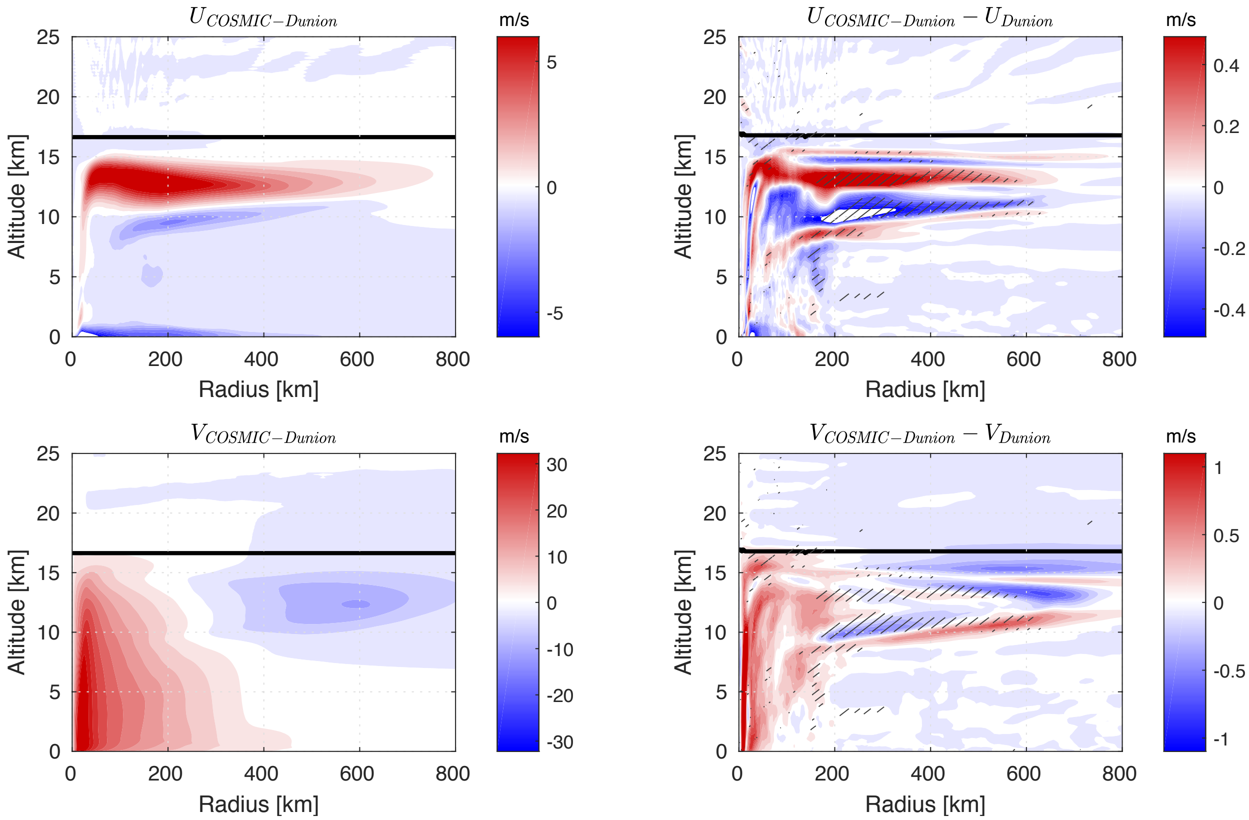

Figure 2.14: (top row) ensemble average radial wind for the COSMIC-Dunion runs and differences with the Dunion runs for the $2-4-$day integration time period. Differences statistically significant to the $95\,\%$ level using Student's *t*-test are hatched. (bottom row) Same but for the azimuthal wind field. The tropopause is indicated in black.

the reflecting level (boundary or sponge layer) is a multiple of the vertical wavelength, reflected and incident wave can constructively interfere and form a standing wave. The result manifests as domain-wide horizontal oscillations below $\sim 28\,\mathrm{km}$. While ducted waves may exist in the real world, their activity may certainly be overestimated in the model given the presence of reflecting levels that have no real world equivalent, and given the 2D . To test whether these ducted waves are the product of the formulation of the sponge layer, several experiments were run with varying sponge layer damping coefficients, bottom altitudes, damping profiles, vertical resolutions, and domain top altitudes (to allow for deeper or higher sponge layers). Ducted waves were found in every simulation, and with amplitudes similar to those seen in Figure 2.15. There seems to be an inverse relationship between the bottom altitude of the sponge layer and temperature variability just below the sponge layer, perhaps indicating that more waves are reflected by the sponge layer when they are allowed to propagate through a deeper layer of stratospheric characteristics. Since no model setup was found that qualitatively affects wave activity in the stratosphere, the choice was made to keep the initial model setup as described in Table 2.1.

Heat budget

The overall thermal structure of the UTLS in simulated TCs being in overall agreement with observations, potential temperature tendency terms are now analyzed to determine sources of cooling near the tropopause. In CM1, the governing equation for potential temperature is:

$$\partial_t \theta \quad = \quad \underbrace{-u\partial_x\theta - v\partial_y\theta - w\partial_z\theta}_{\text{advection}} - \underbrace{c\theta\nabla.\vec{u}}_{\text{moist divergence}} + T + N + D + Q + M$$

with c a constant related to the specific heat of air, ice, liquid, and gaseous water, and the gas constant (see definition at https://www2.mmm.ucar.edu/people/bryan/cm1/cm1_equations.pdf), T the tendency from subgrid turbulence, N the tendency from Newtonian relaxation in the sponge layer, D the tendency from dissipative heating (increase of internal energy when kinetic energy is dissipated), Q the tendency from external energy sources (here the radiation term), and M the tendency from the microphysics scheme (phase changes). In the model setup used, the diffusive

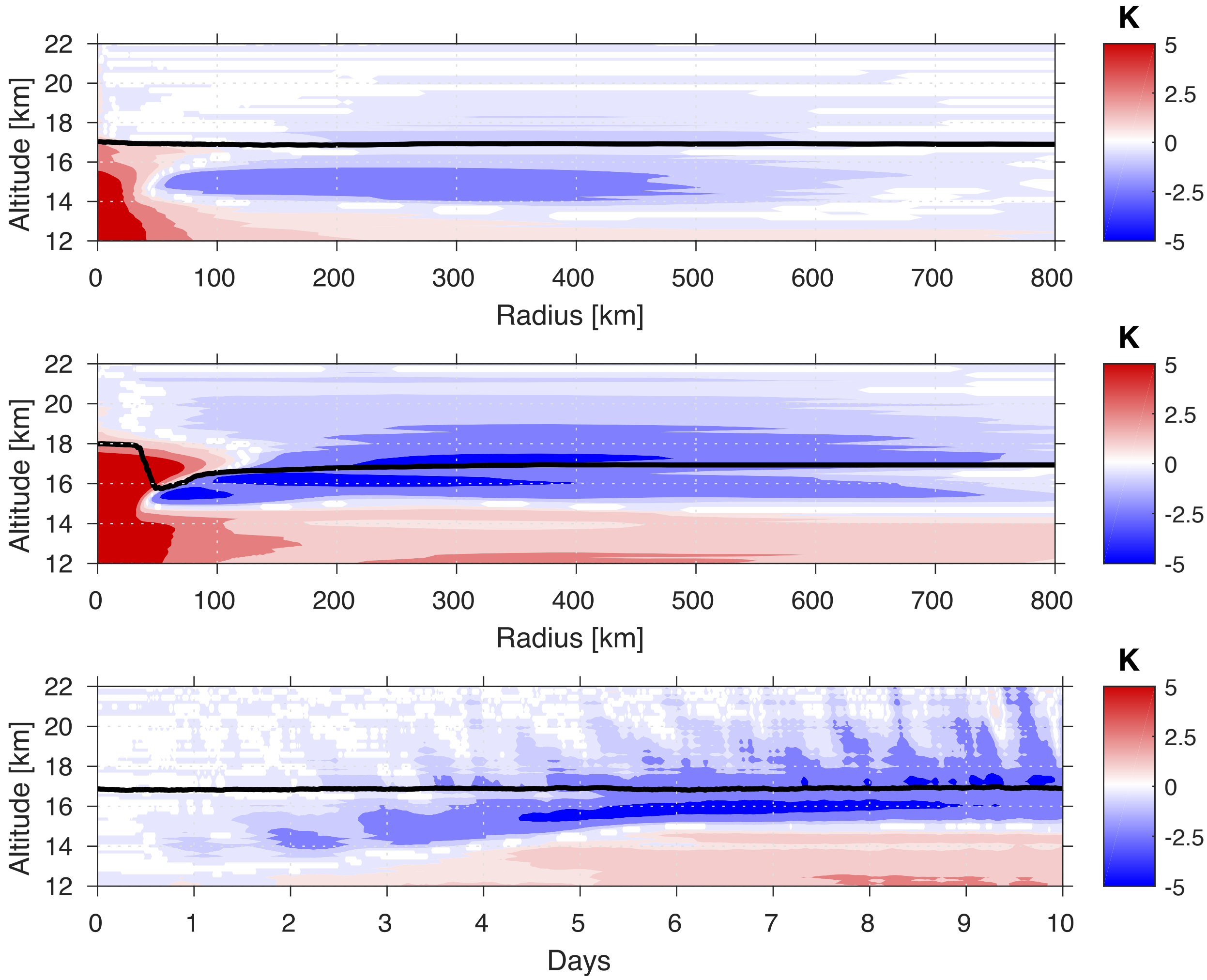

Figure 2.15: Average temperature anomaly as a function of radius and altitude for the $2-4$ day (top) and $8-10$ day (middle) time periods, and (bottom) as a space-time diagram averaged within $200-600\,\mathrm{km}$. The height of the tropopause in indicated in black. Anomalies are defined relative to the initial sounding.

tendency from small-scale fluctuations is ignored, and so is the tendency associated with falling hydrometeors. Since the model is run in its axisymmetric formulation, the azimuthal advection of potential temperature ($-v\partial_y\theta$) is zero.

In practice, the tendency from turbulence is small, that from Newtonian relaxation is only valid in the sponge layer, and that from the moist divergence term is on average small except in the eyewall (similar to the tendency from the microphysics scheme and from dissipative heating). Figure 2.16 shows the budget terms with the largest contributions in the UTLS, and the total tendency ($\partial_t\theta$). As a first observation, no budget term shows a distribution similar to the tropopause layer cooling. The only term with a contribution of the right sign to explain cooling is the radial advection of potential temperature. Both the radial wind velocity (see Figure 2.14) and radial gradient of potential temperature are negative near the tropopause, yielding cooling. The sum of the radial and vertical advection terms (not shown) yields cooling of order $1\,\mathrm{K\,d^{-1}}$ in the region where TLC is found, except at very small radii ($100\,\mathrm{km}$). Figure 2.16f shows that the assumption of steady state ($\partial_t\theta = 0$) is reasonable given the small tendencies shown there.

The contributions to advection of potential temperature by the mean flow and eddy terms are shown in Figure 2.17. Vertical advection by the mean flow produces negative tendencies that are $10-1000$ times smaller than tendencies produced by horizontal eddy terms, indicating that fast-evolving, short-lived eddies such as gravity waves may be responsible for TLC (at least in CM1, for a 2D framework, and with the chosen model setup). Given that the radial gradient of potential temperature is negative throughout the domain (not shown), this means that eddy terms are producing inflow where TLC is found.

If radial inflow produces cooling near the tropopause, one may wonder what causes radial inflow in the first place. To better visualize it, Figure 2.18 shows the streamfunction along with the thermal structure derived from CM1. The clockwise cell in the upper troposphere corresponds to the secondary circulation in its "in-up-and-out" sense (circulation induced by a source of heat in the troposphere, Schubert & McNoldy, 2010). The counterclockwise cell just below the tropopause and extending to $550\,\mathrm{km}$, however, does not directly correspond to the response to a heat source.

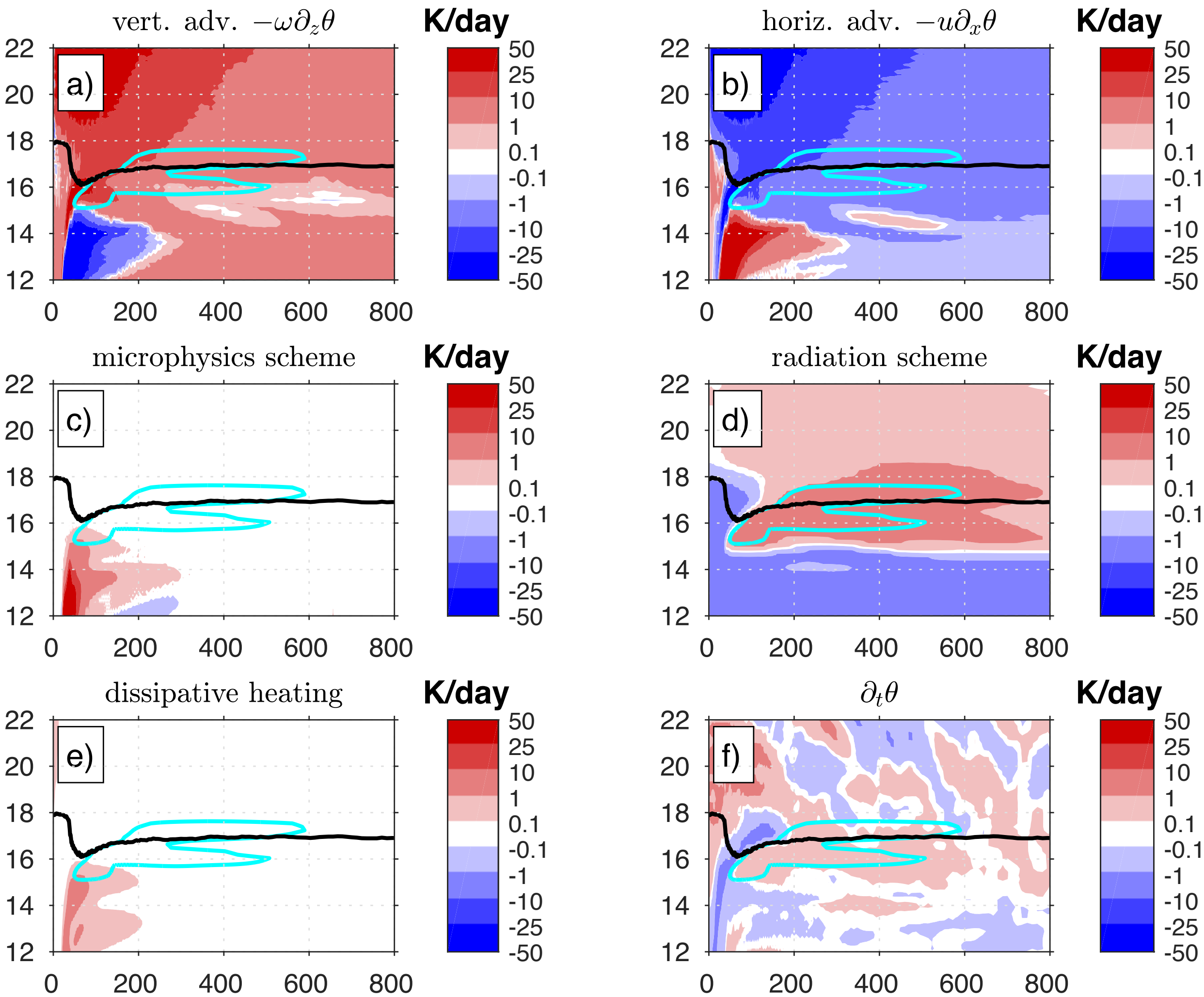

Figure 2.16: Average potential temperature tendency terms for the $8-10$ day time period. The tropopause is indicated in black, and the cyan contour shows $-2\,\mathrm{K}$ potential temperature anomalies. $\partial_t\theta$ is calculated as such, rather than as the sum of the other terms.

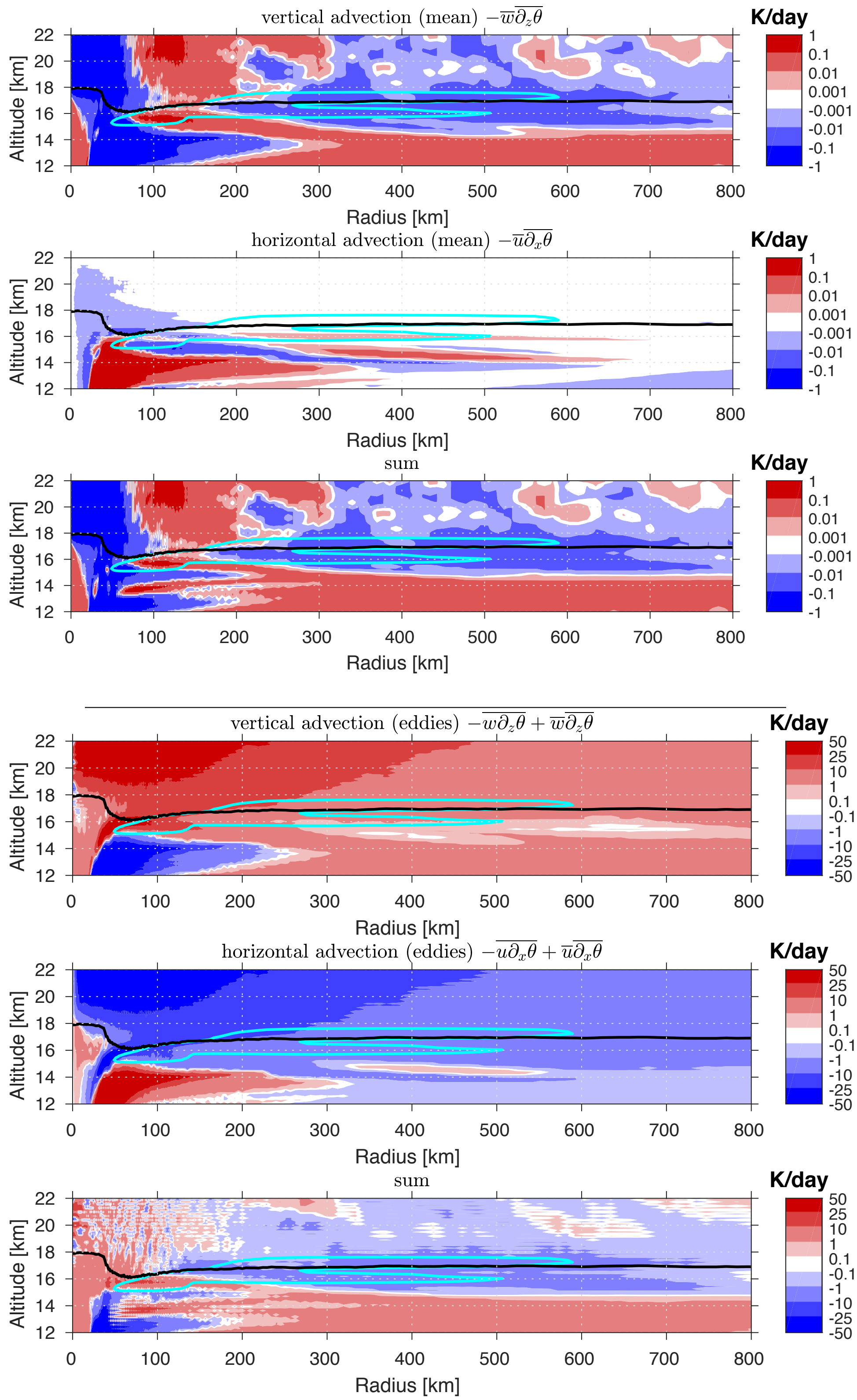

Figure 2.17: Average advective potential temperature tendency terms for the $8-10$ day time period, separated in mean (top) and eddy (bottom) terms, and their sum. The tropopause is indicated in black, and the cyan contour shows $-2\,\mathrm{K}$ potential temperature anomalies. Note the differences in the color schemes.

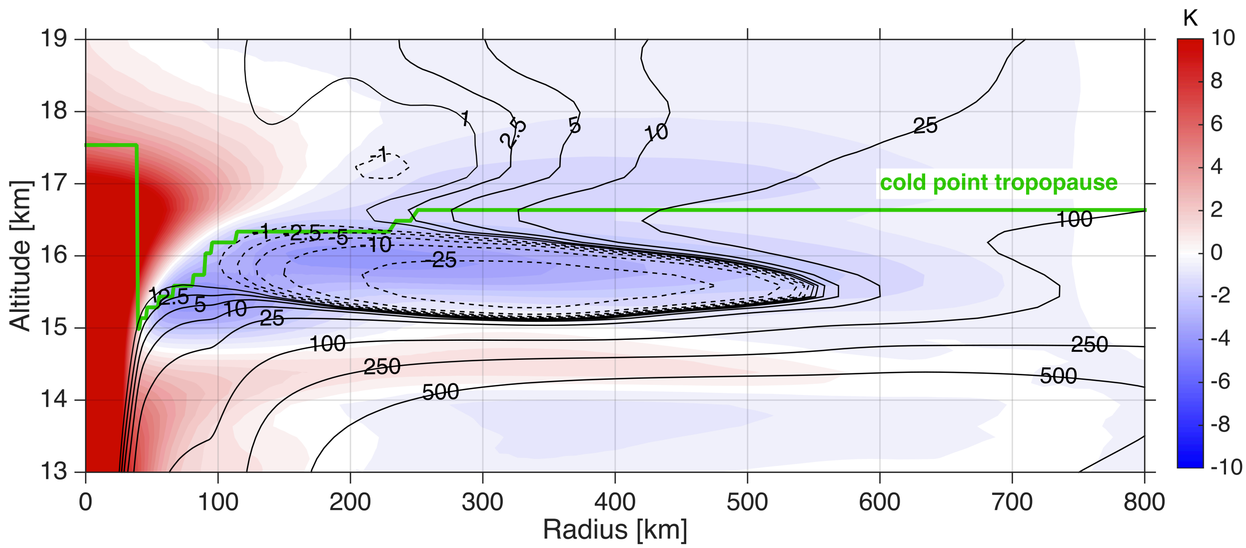

Figure 2.18: Average temperature anomaly (shaded) and streamfunction ($1 \times 10^9\,\mathrm{kg\,m\,s^{-1}}$, solid lines for clockwise flow, dashed for counterclockwise flow) for the $8-9$ day time period.

The presence of this counterclockwise circulation suggests that a source of momentum is acting that produces thermally indirect flow (Shapiro & Willoughby, 1982). The existence of these simulated features is supported by other modeling studies (Ohno & Satoh, 2015; D.-L. Zhang & Chen, 2012) reporting the existence of a narrow layer of inflow near the tropopause. Upper-tropospheric dropsonde data collected during the NASA Hurricane and Severe Storm Sentinel (HS3) field campaign (Komaromi & Doyle, 2017) and observations made in Hurricane Patricia in 2015 (Duran & Molinari, 2018) also corroborate these results. From Figure 2.17, it appears that horizontal advection by both the mean flow and eddies could explain why there is cooling in the portion of the counterclockwise circulation that exhibits downward average motion (between $\sim 100-300\,\mathrm{km}$ radius and $15-16\,\mathrm{km}$ altitude).

Another interesting feature of the streamfunction is the cross-tropopause flow that occurs between $250-800\,\mathrm{km}$, which, strictly speaking, is associated with the deformation of the thermally direct secondary circulation around the thermally indirect cell. Such upward flow is associated with adiabatic expansion and cooling, visible in the temperature anomalies in Figure 2.18 and potentially explaining why cooling exists in the lower stratosphere.

Momentum budget

In order to understand which processes control the radial wind field in the model, one may analyze the budget of radial momentum derived from the zonally-averaged equations of motion. Drawing a parallel between the meridional dimension and radius, and the longitudinal dimension and azimuth, the equations governing the radial flow in cylindrical coordinates may be re-written :

$$\begin{aligned}
\partial_t u + u\partial_r u + \frac{v}{r}\partial_\lambda u + w\partial_z u - \frac{v^2}{r} - fv &= -\frac{\partial_r p}{\rho} \\
\partial_t v + u\partial_r v + \frac{v}{r}\partial_\lambda v + w\partial_z v - \frac{uv}{r} + fu &= -\frac{\partial_\lambda p}{\rho} \\
\partial_t w + u\partial_r w + \frac{v}{r}\partial_\lambda w + w\partial_z w &= -\frac{\partial_z p}{\rho} - g \\
\partial_t \rho + \frac{\partial_r(\rho r u)}{r} + \frac{\partial_\lambda(\rho v)}{r} + \partial_z(\rho w) &= 0 \\
\partial_t \theta + u\partial_r \theta + \frac{v}{r}\partial_\lambda \theta + w\partial_z \theta &= Q
\end{aligned} \tag{2.1}$$

with t the time, u the radial wind (along r), v the azimuthal wind (along λ), w the vertical wind (along z), f the Coriolis factor, ρ the density, p the pressure, θ the potential temperature, and Q representing external sources of heat. Since the simulations run here have no azimuthal structure, $\partial_\lambda = 0$. Applying gradient wind balance (balance of the pressure gradient force, centrifugal force, and Coriolis):

$$-\frac{v_g^2}{r} - fv_g = -\frac{\partial_r p}{\rho}$$

where v_g is the component of the azimuthal wind that is in gradient wind balance, i.e. $v = v_g + v_a$ with v_a the component of the azimuthal wind not in gradient wind balance, one may write (2.1) as:

$$\partial_t u + u\partial_r u + w\partial_z u - \frac{v_a^2}{r} - \frac{2v_g v_a}{r} - fv_a = 0$$

Now decomposing the flow in its time mean and deviations therefrom:

$$
\begin{aligned}
u &= \overline{u} + u' \\
w &= \overline{w} + w'
\end{aligned}
$$

$$
\overline{\partial_t u} + \overline{u\partial_r u} + \overline{w\partial_z u} - \overline{\frac{(v_a + 2v_g)v_a}{r}} - f\overline{v_a} = 0
$$

becomes (with $\overline{\partial_t} = 0$ and $\overline{x'} = 0$):

$$
\underbrace{\overline{u}\partial_r\overline{u} + \overline{w}\partial_z\overline{u}}_{\text{adv. by the mean flow}} + \underbrace{\overline{u'\partial_r u'} + \overline{w'\partial_z u'}}_{\text{adv. by eddies}} - \underbrace{\overline{\frac{(v_a + 2v_g)v_a}{r}}}_{\text{curvature term}} - \underbrace{f\overline{v_a}}_{\text{Coriolis term}} = 0 \tag{2.2}
$$

The contribution to the acceleration of the radial flow from eddies corresponds to gravity wave activity in the UTLS. Gravity wave activity can be affected in the vicinity of model boundaries (e.g., at the inner radius in the simulations), however, this is limited to small radii (inside $100\,\mathrm{km}$) in the simulations. The advection by eddies is otherwise a small term (1–2 orders of magnitude smaller than advection by the mean flow). The advection by the mean flow becomes very small above $15\,\mathrm{km}$. At first glance, the terms which contain v_a (the curvature term and and the Coriolis term) exhibit the largest magnitudes near the tropopause. The Coriolis term (Figure 2.19) is the only term which exhibits a structure in alignment with the development of a counterclockwise circulation: outward acceleration below $16\,\mathrm{km}$ and inward acceleration above.

Remains to explain why the agradient wind has the structure shown in Figure 2.19. A scale analysis of the equations of motion (e.g., Willoughby, 1979) supports the common assumption that the winds above the boundary layer are held in gradient wind balance, however, such balance is expected to break down where the magnitude of the secondary circulation approaches that of the primary circulation (the vortex). This happens near the top of the vortex, where vortex Rossby waves and gravity waves may violate gradient wind balance. This break down also occurs where vertical gradients of frictional forces exist (in the boundary layer) and where radial and vertical gradients of diabatic heating exist (associated with deep convection and its changing structure, see Section 2.1).

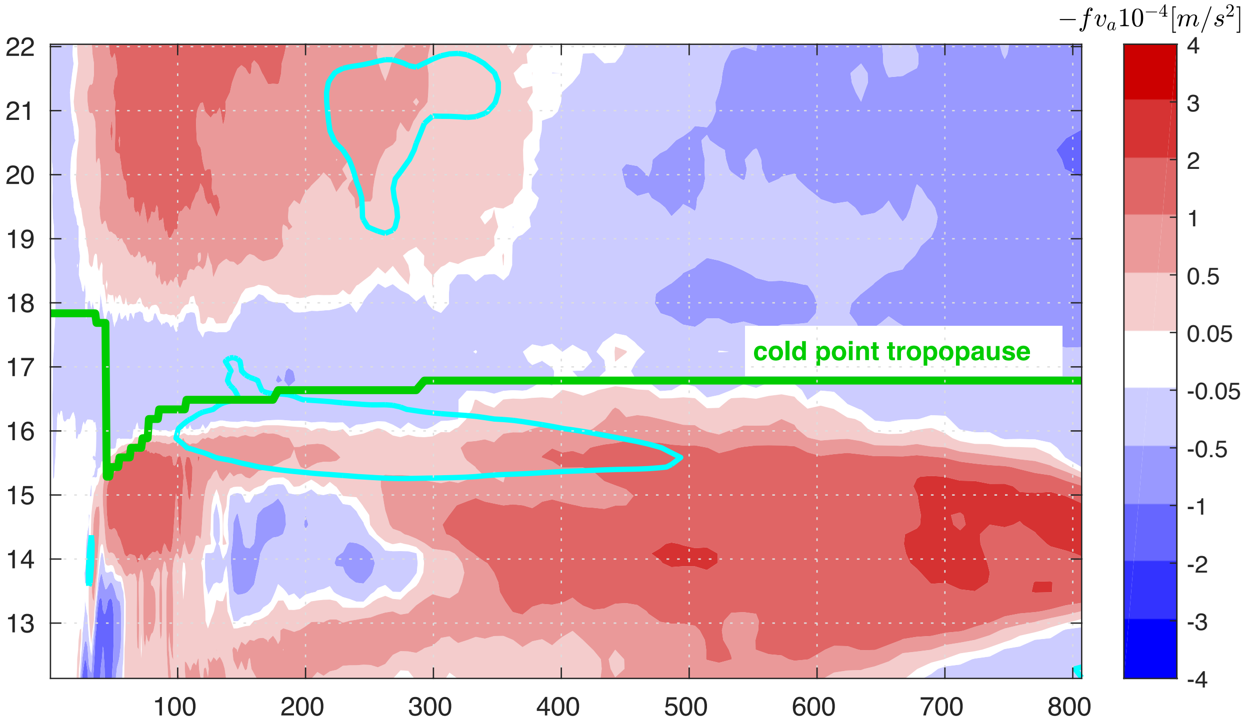

Figure 2.19: Acceleration of the radial flow due to the Coriolis term from (2.2). The $-1 \times 10^9\,\mathrm{kg\,m\,s^{-1}}$ contour of the streamfunction is shown in cyan. Note that the structure of the agradient azimuthal wind field can be inferred from this figure (the shading is proportional to v_a).

Chapter 3

Implications of tropopause layer cooling for tropical cyclone dynamics

As was seen in TC simulations from CM1 in Section 2.2.2, cooling near the tropopause occurs after an incubation time period of a few days during which cooling occurs below the tropopause. This evolution seems worth consideration to understand the role of clouds in TLC, given that cooling first occurs near the cloud top and evolves to stabilize near the tropopause, where cloud tops are not as frequent. In this section, the question of the feedbacks between the cooling and individual cloud elements is addressed. If such feedbacks are unearthed, they could allow improved understanding of the interplay between convection and dynamics in the upper troposphere of TCs.

The approach chosen to address the question is to **1)** develop a simple representation of a moist updraft using parcel theory to **2)** make predictions about the behavior of moist updrafts released in the environment characteristic of TCs (using simulations from Section 2.2.2), and finally **3)** to assess the realism and relevance of such predictions by comparison with idealized simulations of atmospheric warm bubbles.

3.1 Parcel theory

The case of an air parcel lifted pseudo-adiabatically from the surface is studied. The list of relevant variables and parameters is provided in Table 3.1:

The LCL is the height at which the parcel becomes saturated when lifted dry adiabatically, i.e., the height at which the dew point temperature and the temperature of the parcel are equal. The LFC is the height above the LCL at which the temperature of the parcel is larger than that of the environment. The LNB is the height above the LFC at which the temperature of the parcel is equal to that of the environment. CAPE is calculated as:

Table 3.1: List of symbols for parcel theory

CAPE	$\mathrm{J\,kg^{-1}}$	Convective Available Potential Energy
C_{pd}	$1005.7\,\mathrm{J\,kg^{-1}\,K^{-1}}$	heat capacity at constant pressure of dry air
C_{pv}	$1870\,\mathrm{J\,kg^{-1}\,K^{-1}}$	heat capacity at constant pressure of water vapor
dz	m	incremental height
e_s	hPa	saturation partial pressure of water vapor
Γ	$\mathrm{K\,m^{-1}}$	lapse rate
Γ_d	$9.8\,\mathrm{K\,km^{-1}}$	dry adiabatic lapse rate
λ	$\%\,\mathrm{m^{-1}}$	entrainment rate
LCL	m	Lifted Condensation Level
LFC	m	Level of Free Convection
LNB	m	Level of Neutral Buoyancy
LMO	m	Level of Maximum Overshoot
L_f	$3.34 \times 10^5\,\mathrm{J\,kg^{-1}}$	latent heat of fusion
L_v	$2257 \times 10^3\,\mathrm{J\,kg^{-1}}$	latent heat of vaporization
$L_s = L_v + L_f$	$\mathrm{J\,kg^{-1}}$	latent heat of sublimation
P	hPa	pressure
r	$\mathrm{kg\,kg^{-1}}$	water vapor mixing ratio
R_v	$461.5\,\mathrm{J\,kg^{-1}\,K^{-1}}$	gas constant of water vapor
R_d	$287.04\,\mathrm{J\,kg^{-1}\,K^{-1}}$	gas constant of dry air
$\epsilon = \dfrac{R_d}{R_v}$	0.622	
T	kelvin	temperature
T_0	$273.15\,\mathrm{K}$	freezing temperature of pure water at $1000\,\mathrm{hPa}$
T_V	K	virtual temperature
Subscripts:		
$_p$		parcel
$_e$		environment

$$CAPE = g\int_{LFC}^{LNB} \frac{T_{Vp} - T_{Ve}}{T_{Ve}} dz$$

and is proportional to the area between T_{Vp} and T_{Ve} from the LFC to the LNB. The LMO is calculated by assuming that all CAPE is converted to kinetic energy at the LNB, i.e., LMO is such that:

$$\int_{LNB}^{LMO} \frac{T_{Vp} - T_{Ve}}{T_{Ve}} dz = \int_{LFC}^{LNB} \frac{T_{Vp} - T_{Ve}}{T_{Ve}} dz$$

To best predict the behavior of the ascending parcel, virtual temperature is used rather than temperature. Virtual temperature accounts for the difference in density between dry air and water vapor, and is the proper variable to use in the equation of state $P = \rho R_d T_V$ so that R be truly constant. Given the sensitivity of a parcel's path to its initial state, it is important to account for the virtual temperature correction, as pointed out by Doswell and Rasmussen (1994). Virtual temperature is calculated as:

$$T_V = T\frac{1 + r\epsilon^{-1}}{1 + r}$$

T_V is always greater than or equal to temperature since replacing part of the air in a parcel by water vapor makes the parcel less dense, which can be considered equivalent to warming the parcel.

Several assumptions are made for the parcel's ascent:

- The level of freezing (level at which the phase of all condensate changes from liquid to solid) is defined as the height at which $T_{Vp} \leq T_0$. This is a simplification of what is observed in nature. Cloud droplets do not readily freeze at 0^oC, rather, they may remain in a super-cooled liquid state until homogeneous freezing occurs, or until ice nuclei make contact with the droplets. Given the dependency of homogeneous freezing with droplet size, and given the variability in the nature and number concentration of ice nuclei that marine deep convection may encounter, accounting for variations in the freezing level would require significant modifications to parcel theory—modifications which are not within the scope of the study.

- The ascent of the parcel is assumed to be pseudoadiabatic, i.e., all condensate is removed from the parcel as it forms. This is again a simplification of what is observed in nature. Cloud droplets and ice crystals can be lofted in updrafts, implying a reduced T_V from mass loading and an aerodynamic drag onto the condensate. Both these effects are ignored for the purpose of the study.

- The formulation of entrainment λ is such that every kilometer, $\lambda\%$ of the parcel's volume is replaced with air from the environment. This simple formulation is in a sense more analog to dilution than entrainment, that is to say, the formulation is more analog to environmental air penetrating the convective core and mixing with it than it is analog to environmental nonactive air being activated by convection and mixed into cloudy air at the edge of the cloud (Romps, 2010). This is not a problem for the analysis: the purpose of including entrainment here is to evaluate the qualitative effect of environmental air mixing with the cloud regardless of the precise location of said mixing, rather than evaluating the more nuanced behaviors one may obtain with more complete formulations. The formulation of entrainment here includes dilution by entrainment (Hannah, 2017) for free convection.

- The initial location of the parcel is the average pressure for the parcel. For coherence with the numerical model setup chosen for the warm bubble simulations in Section 3.3, the parcel has depth $1\,\mathrm{km}$ and is launched near $975\,\mathrm{hPa}$. Qualitatively speaking, the deeper the initial parcel the colder it is and the smaller LNB.

The iterative, one-dimensional algorithm is formulated as follows (the z and $z+1$ subscripts indicate that variables are estimated at a vertical level z or at the vertical level just above $z+1$):

At the initial parcel location:

$$\begin{aligned} T_{Vp} &= T_{Ve} \\ r_p &= r_e \\ \Gamma_p &= \Gamma_d \end{aligned}$$

From the initial location to the LCL: dry, undilute ascent:

$$\begin{aligned} T_{Vp,z+1} &= T_{Vp,z} - \Gamma_z dz \\ r_{p,z+1} &= r_{p,z} \\ \Gamma_{z+1} &= \Gamma_d \end{aligned}$$

From the LCL to the LFC: saturated ($e = e_s$), undilute ascent:

$$
\begin{aligned}
T_{Vp,z+1} &= T_{Vp,z} - \Gamma_z dz \\
e_{s,z+1} &= 6.112\ \exp\left(\frac{\alpha(T_{V,z+1} - T_0)}{T_{Vp,z+1} - T_0 + \beta}\right) \quad \text{Bolton (1980)} \\
r_{p,z+1} &= \frac{\epsilon e_{s,z}}{P_z - e_{s,z}} \\
\Gamma_{z+1} &= \Gamma_d \, \frac{1 + r_{p,z+1}}{1 + r_{p,z+1}\dfrac{C_{pv}}{C_{pd}}} \, \frac{1 + \dfrac{L r_{p,z+1}}{R_d T_{p,z+1}}}{1 + \dfrac{L^2 r_{p,z+1}(1 + r_{p,z+1}\epsilon^{-1})}{R_v T_{p,z+1}^2 (C_{pd} + r_{p,z+1} C_{pv})}} \quad \text{K. A. Emanuel (1994)}
\end{aligned}
$$

$$
\begin{aligned}
\alpha &= 17.67 \\
\beta &= 243.5\,\mathrm{K} \\
L &= L_v
\end{aligned}
$$

From the LCL to the top of the sounding: saturated ascent ($e = e_s$) with entrainment:

$$
\begin{aligned}
T_{Vp,z+1} &= (T_{Vp,z} - \Gamma_z dz)(1 - \lambda dz) + \lambda dz T_{Ve,z} \\
e_{s,z+1} &= 6.112 \ \exp\left(\frac{\alpha(T_{V,z+1} - T_0)}{T_{Vp,z+1} - T_0 + \beta}\right) \\
r_{p,z+1} &= \frac{\epsilon e_{s,z}}{P_z - e_{s,z}}(1 - \lambda dz) + \lambda dz(r_{e,z+1}) \\
\Gamma_{z+1} &= \Gamma_d \, \frac{1 + r_{p,z+1}}{1 + r_{p,z+1}\dfrac{C_{pv}}{C_{pd}}} \, \frac{1 + \dfrac{L r_{p,z+1}}{R_d T_{p,z+1}}}{1 + \dfrac{L^2 r_{p,z+1}(1 + r_{p,z+1}\epsilon^{-1})}{R_v T^2_{p,z+1}(C_{pd} + r_{p,z+1}C_{pv})}}
\end{aligned}
$$

Below the freezing level ($T_{Vp} > T_0$):

$$
\begin{aligned}
\alpha &= 17.67 \\
\beta &= 243.5\,\mathrm{K} \\
L &= L_v
\end{aligned}
$$

Above the freezing level ($T_{Vp} \leq T_0$)

$$
\begin{aligned}
\alpha &= 23.46 \\
\beta &= 272.62\,\mathrm{K} \\
L &= L_s
\end{aligned}
$$

Fundamental differences exist between the cloud represented by the above algorithm and a real cloud. Since entrainment is induced by discrete eddies in the real world, the interior of the moist updraft is in reality far from homogeneous. This process is not represented by the algorithm, since the algorithm is one-dimensional. Another process that is not represented is the presence of downdrafts driven by evaporative cooling at the edge of real clouds. These downdrafts form subsiding shells (Heus & Jonker, 2008; Jonker, Heus, & Sullivan, 2008) composed of a mixture of udpraft and environmental air, leading to significant downward mass flux. The effect of subsiding shells on convection is thought to be large, and subsiding shells may even explain why Jonas (1990) observed in-cloud air masses with properties of the environment at higher altitudes. Lastly, the life cycle of clouds and the circulations generated by precipitation are not represented in the moist updraft algorithm.

Despite the long list of assumptions and simplifications, the moist updraft algorithm is a valuable tool to isolate the basic, qualitative response of clouds to environmental perturbations like those seen in TCs. The effect of ice processes and entrainment is illustrated in Figure 3.1. When ice processes are taken into account, additional latent heat is released within the parcel above the freezing level (since $L_s > L_v$), leading to larger T_{Ve} and consequently larger LNB. Increasing entrainment rates yield decreasing LNB, consistent with dry ambient air limiting the intensity and height of a moist updraft (Del Genio, 2012; Derbyshire et al., 2004).

3.2 Predictions from parcel theory

The average vertical thermal structure within simulated TCs is extracted from simulations in Section 2.2.2 and is shown in Figure 3.2a) as a function of integration time. The presence of a tropospheric warm core and of cooling aloft is evident, along with warming in the low troposphere, boundary layer cooling, and other smaller variations throughout the atmosphere. For the purpose of studying the effect of the tropospheric warm core and cooling aloft on convection, the low-level features (below $\sim 5\,\mathrm{km}$) must be removed. These anomalies would otherwise dominate any behavior predicted from parcel theory, especially when entrainment is taken into account (large anomalies near the LCL and LFC would then mask the response of the moist updraft to the tropospheric and upper-tropospheric structures). Additionally, since an idealized approach is used and since the goal is to isolate overall, qualitative behaviors, small variations should also be removed. To do so, the anomalies in Figure 3.2a are approximated analytically with the following parameters:

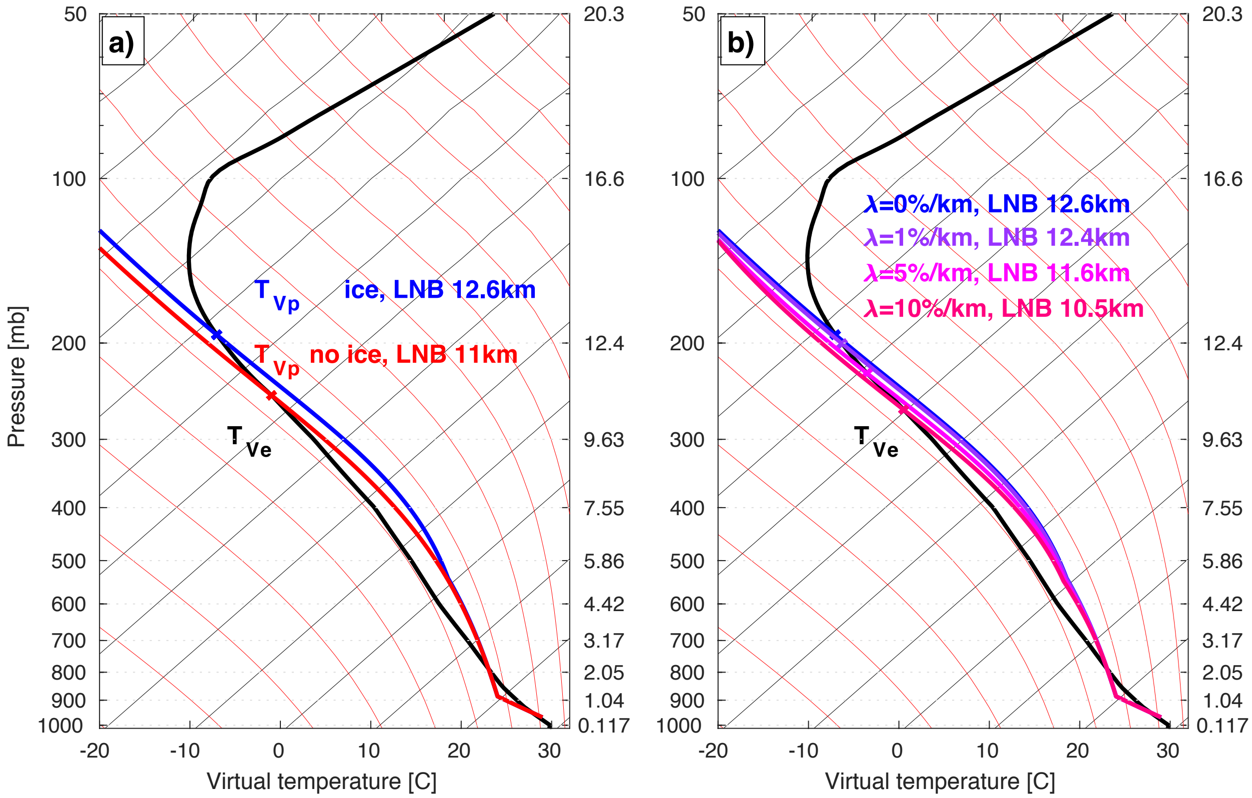

Figure 3.1: Skew-T diagrams for T_{Ve} (black) and T_{Vp} (colors) demonstrating the effects of **a)** ice processes and **b)** convective entrainment. The right hand side coordinate is pressure altitude [km].

- The altitude at which anomalies pass through zero between the warm core and the cooling aloft; z_0.
- The magnitude of the warm core m, considered to be equal to that of the cooling aloft (they are nearly equal at long integration times and are positively correlated).
- The depth of the cooling aloft, σ_C, and σ_W related to the half width of the warm core at its half maximum.

Given the shape of the cooling aloft and given how quickly it approaches zero near its summit, it is approximated using a sine function. The warm core is approximated below its maximum value using a Gaussian function, in order to capture the smaller anomalies in the middle troposphere. Above its maximum value, the warm core is approximated using the same sine function as for the cooling. This ensures a smooth transition between the warm core and cooling, as well as a smooth transition between the lower and upper parts of the warm core. The temperature anomaly profiles are approximated as follows:

$$
\begin{aligned}
\Delta T(z) &= m \sin\left(\pi \frac{z - z_0}{\sigma_C}\right) && \text{where } z \leq z_0 + \sigma_C \;\&\; z \geq z_0 - \sigma_C/2 \\
\Delta T(z) &= m \exp\left(-\frac{1}{2}\left(\frac{z - (z_0 - \sigma_C/2)}{\sigma_W}\right)^2\right) && \text{where } z < z_0 - \sigma_C/2
\end{aligned}
$$

with $\sigma_C = 2.12\,\mathrm{km}$ determined using the simulated anomaly profile at 9 days (see Figure 3.2), and σ_W chosen so that the half width at half maximum ($HWHM$) for the Gaussian function be $5\,\mathrm{km}$, i.e., with $\sigma_W = HWHM\sqrt{2\log(2)}^{-1}$, $\sigma_W \approx 4.25\,\mathrm{km}$.

In order to understand how the warm core and cooling aloft may modulate the depth of convection and how they may change the way a TC interacts with the TTL, the dependency of the cloud top with z_0 and m is first analyzed. In the moist updraft algorithm, the cloud top could be estimated using either the LNB or the LMO. Since overshooting is relatively rare over the open oceans, the LNB is chosen as a proxy for the cloud top. This choice is also motivated by the

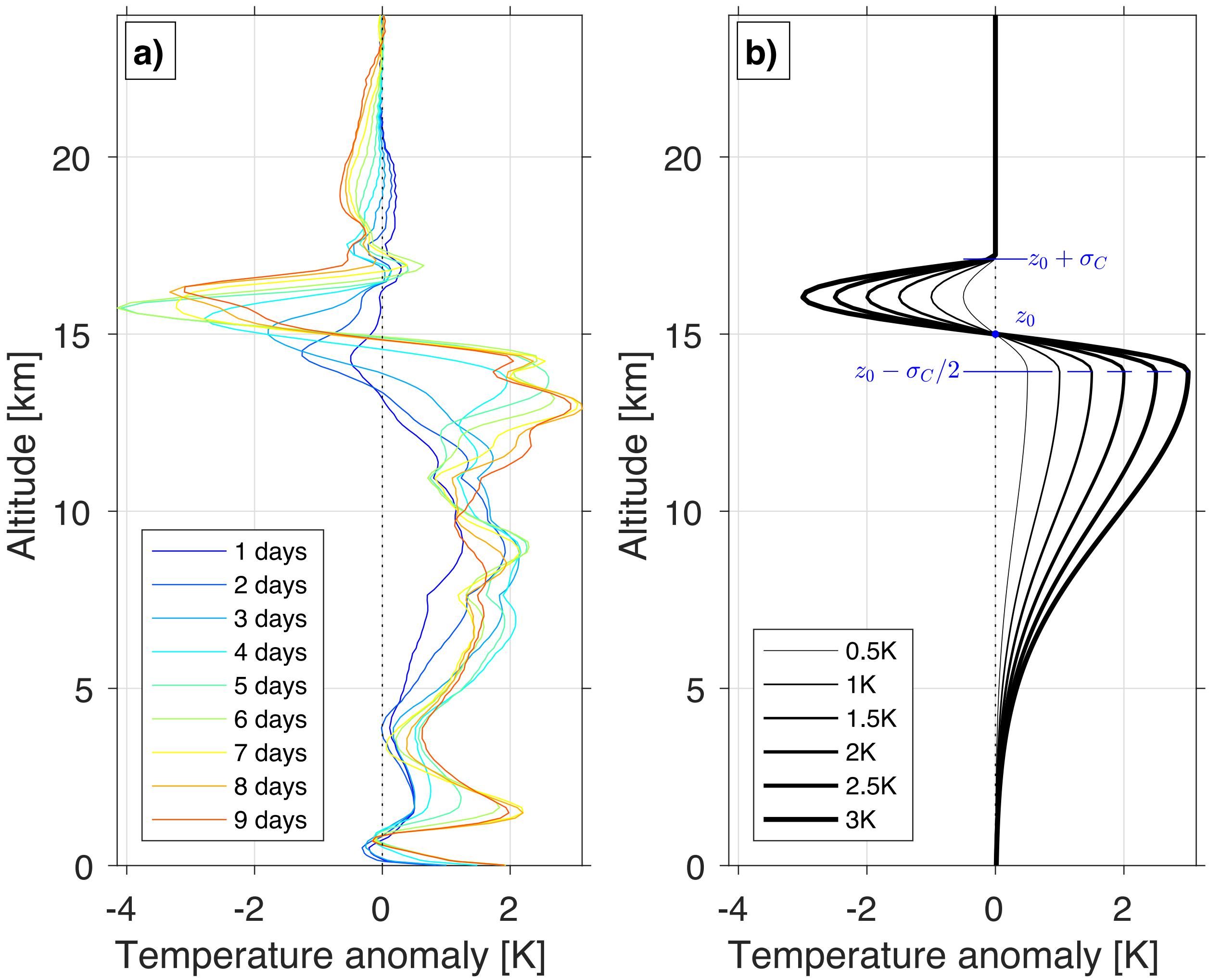

Figure 3.2: a) Simulated and **b)** idealized temperature anomaly profiles within TCs. Anomalies in **a)** are the difference of the 1-daay averaged simulated temperature from TC simulations between $100 - 200\,\mathrm{km}$ and $1000 - 1400\,\mathrm{km}$. Heights relevant to the analytical approximation of the temperature anomalies are indicated in blue in **b)**.

results of Sherwood, Minnis, and McGill (2004) which indicate that in reality, little CAPE is available near the LNB to propel cloud parcels to their LMO, because most of the CAPE is consumed by mixing with the environment. Additionally, results in Sherwood et al. (2004) and Takahashi and Luo (2014) indicate high correlation between the observed cloud top height and the LNB (especially for convection over the oceans).

Lifting a parcel which has the same properties as its environment produces relatively low LNBs ($10.5 - 12.5\,\mathrm{km}$, Figure 3.1) that are below the lowest z_0 from the simulations. However, LNB is expected to be most sensitive to changes in the environmental profile when z_0 approaches the LNB. Additionally, results in Rivoire et al. (2020, in review) indicate that deep convective cloud top heights in TCs below $12.5\,\mathrm{km}$ are very rare in the inner core. Therefore, the choice is made to lift a parcel that is initially warmer than their environment. This is done using the warm bubble setup from CM1; a temperature anomaly of magnitude $4\,\mathrm{K}$ and height $1\,\mathrm{km}$ is introduced to the profile of T_{Vp}. Note that introducing a warm bubble to the parcel profile does not change the qualitative results discussed below. Without a warm bubble, the results presented below would not be as relevant to the TC simulations. Introducing a warm bubble of magnitude $2\,\mathrm{K}$ or $8\,\mathrm{K}$ produces different results, with the weaker warm bubble reaching a maximum altitude near $14\,\mathrm{km}$ and the stronger warm bubble reaching altitudes near $19\,\mathrm{km}$ and producing unrealistically large vertical velocities. The sensitivity of the simulations to the initial height of the warm bubble is also large, and $1\,\mathrm{km}$ was chosen to match the study of Kilroy and Smith (2013). An important discussion point is the height at which the warm bubble is initiated. In the present case (and as in Kilroy & Smith, 2013), the warm bubble is initiated at the ground in order to ensure comparability with results from parcel theory. While warm bubbles are typically released near the ground (see e.g., Crook & Moncrieff, 1988; Kilroy & Smith, 2013; Rotunno, Klemp, & Weisman, 1988), deep tropical convection is known to produce vertical profiles of latent heating with a maximum near $5\,\mathrm{km}$ (Zagrodnik & Jiang, 2014). It may therefore be necessary to consider similar warm bubble experiments with a release height near $5\,\mathrm{km}$, although these experiments cannot be directly compared with results from the parcel theory laid out in Section 3.1. One advantage of increasing the release altitude for warm bubble simulations is that the resulting cloud may reach higher altitudes (desired in order to represent deep convection) without the need for a large energy input. For the time being, the release location is chosen as the ground, since isolating specific aspects of the basic response of convective clouds to their thermodynamic environment is still possible with this setup.

Figure 3.3 shows the dependency of the LNB on z_0 and m for several entrainment rates. When z_0 is below the LNB for an undisturbed environment (the LNB for $m = 0$, indicated by the red lines and subsequently referred to as “control LNB”), the cooling aloft lifts the intersection between T_{Vp} and T_{Ve} and LNB increases with increasing m. Moist updraft profiles illustrating this effect are indicated by blue circles in Figure 3.3a and are shown in Figure 3.4a. When z_0 is above the undisturbed LNB, it is the warm core which lowers the intersection between T_{Vp} and T_{Ve} and LNB decreases with increasing m. This effect is illustrated in Figure 3.4b (see pink circles in Figure 3.3a. For z_0 above the undisturbed LNB, the LNB is a steeper function of m when entrainment rate increases. This is because when z_0 is below the undisturbed LNB, the warm core lowers the LNB and the intersection between T_{Vp} and T_{Ve} occurs near smaller environmental lapse rate, leading to enhanced sensitivity of the LNB to small changes in m. The LNB shows little sensitivity to z_0, except when z_0 approaches the undisturbed LNB; in this case, the LNB exhibits maximal sensitivity to z_0 and minimal sensitivity to m. This is because when z_0 is near the LNB, neither the warm core of the cooling aloft may modulate the LNB unless m is very large. These results suggest that cloud top height is impacted the most by environmental disturbances when it is located just above or just below z_0. If one considers z_0 and m to be set by former convection, the results indicate that cloud top heights are most sensitive to their environment when they change slowly over time.

The hatching in Figure 3.3 has not been discussed yet. It indicates areas where a layer of near-neutral buoyancy (LNNB) develops around the LNB. The presence of an LNNB makes the notion of LNB irrelevant, as LNB may increase or decrease without the need for energy input to the parcel. An LNNB is detected when:

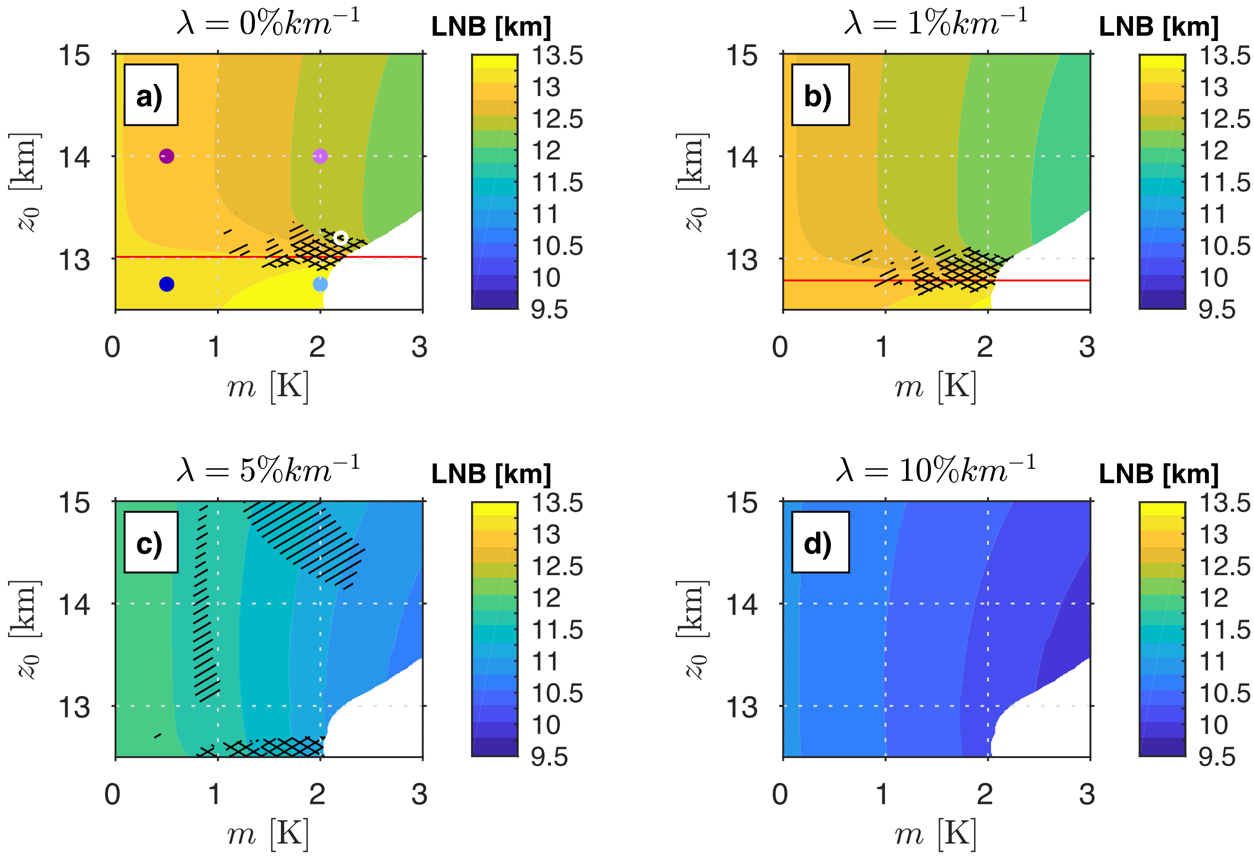

Figure 3.3: LNB (shaded) as a function of m and z_0 with entrainment rate λ **a)** $0\,\%\,\mathrm{km}^{-1}$, **b)** $1\,\%\,\mathrm{km}^{-1}$, **c)** $5\,\%\,\mathrm{km}^{-1}$, and **d)** $10\,\%\,\mathrm{km}^{-1}$. The red lines indicate the LNB for m=0 (z_0 is irrelevant in this case). Areas with single black hatching indicate that a layer of near-neutral buoyancy (LNNB) forms around the LNB (see text for details). The hatching is doubled when the LNNB is at least $1000\,\mathrm{m}$ deep. The control LNB for **c)** is $11.9\,\mathrm{km}$ and for **d)** is $10.8\,\mathrm{km}$. Full, colored circles correspond to Figure 3.4, and the white hollow circle corresponds to Figure 3.5. Areas of the $\{m,z_0\}$ parameter space that lead to the formation of superadiabatic layers ($\Gamma > 9.8\,\mathrm{K\,km}^{-1}$) appear white.

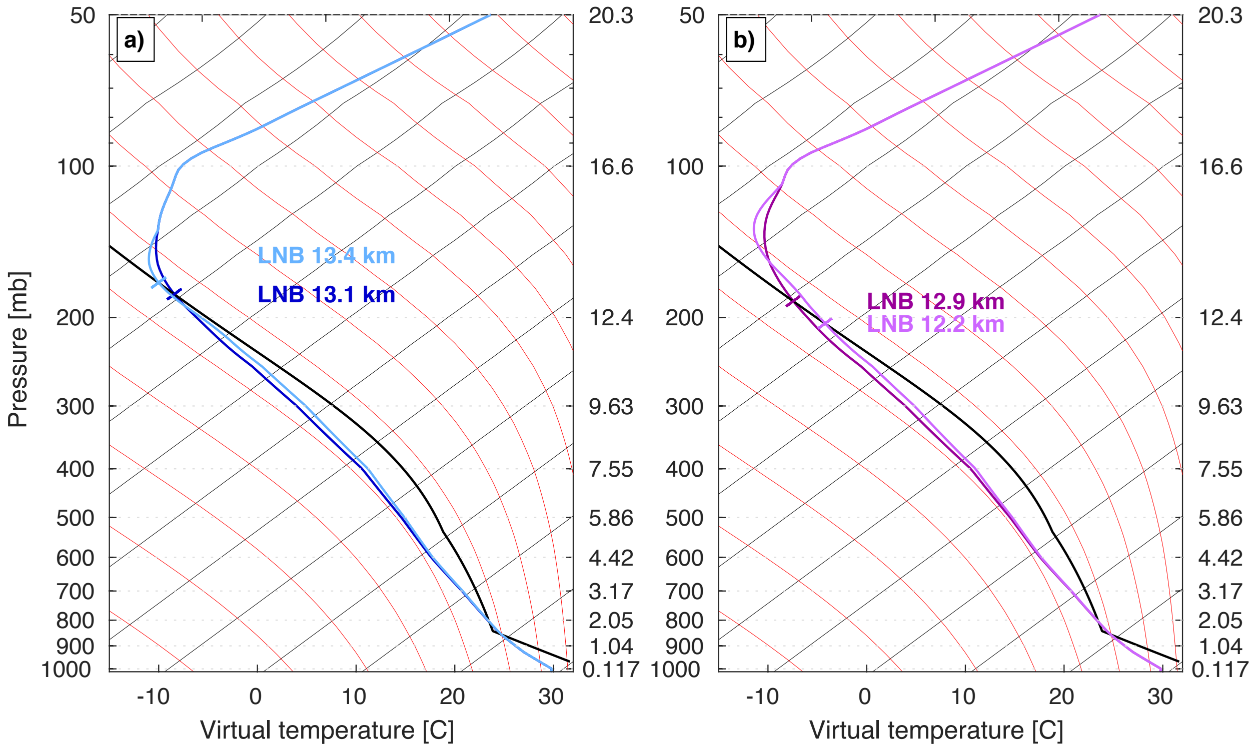

Figure 3.4: Skew-T diagrams for T_{Vp} (black) and T_{Ve} (colors) demonstrating the effects of increasing m when z_0 is **a)** above and **b)** below the control LNB. The color scheme for T_{Ve} corresponds to full, colored circles in Figure 3.3a. The right hand side coordinate is pressure altitude [km].

$|T_{Vp} - T_{Ve}| \leq 1.25\,\mathrm{K} \quad \& \quad |\Gamma_p - \Gamma_e| \leq 1.25\,\mathrm{K\,km^{-1}}$

These *ad hoc* thresholds were chosen so that the behavior of the LNNB be clearly visible on Figure 3.3 (more stringent thresholds simply diminish the size of the hatched areas on Figure 3.3). More work would need to be done to understand what thresholds might be more sensible. The LNNB is caused by increases in the environmental lapse rate that bring Γ_p closer to Γ_p. Increases in the environmental lapse rate maximize around z_0. For this reason, the LNNB tends to form when the LNB is close to z_0, at least when the entrainment rate is small. For moderate entrainment rate (Figure 3.3c), an LNNB may form even when the LNB is far below z_0, however, this LNNB is very shallow and therefore not as impactful on the LNB. For large entrainment, no LNNB forms because the LNB occurs where Γ_p and Γ_e are too far from one another. One example of LNNB is illustrated in Figure 3.5. In this example, the LNNB only forms when the environment contains sufficiently large temperature anomalies near the LNB.

The formation of the LNNB has several implications for TC dynamics. First, the LNNB may lead to deeper subsequent convection, since very little energy is then required to lift the parcel by several hundreds of meters ($1200\,\mathrm{m}$ in Figure 3.5). This is especially true when accounting for entrainment, which deepens the LNNB and exacerbates the sensitivity of clouds to the TC thermal structure. Deeper clouds may imply a deeper secondary circulation and elevated outflow layer, which increases MPI. Deeper clouds may also lead to radiative cooling near the cloud top at greater altitudes, closer to the tropopause. Second, the presence of the LNNB implies that clouds may form which–strictly speaking–overshoot their LNB, but which may not display the same characteristics as clouds that overshoot in the absence of LNNB (dome-like protrusions above anvils). Finally, the LNNB may correspond to a decrease in the Richardson number, that is, enhanced potential for turbulent mixing. This would be consistent with the suggestion by K. Emanuel and Rotunno (2011) that the Richardson number falls below a critical value for turbulence in the TC outflow layer, suggestion which was confirmed by observational analysis in Molinari, Duran, and Vollaro (2014). All these effects may display a diurnal cycle, given the importance of cloud radiative processes in establishing a warm/cold dipole in the upper troposphere. If that is the case, deeper, more frequent LNNBs could form during the daytime when in-cloud absorption of solar radiation produces increased lapse rate anomalies near the cloud top.

As a side remark, the use of CAPE as a proxy or metric for convective vigor may be problematic when the LNNB forms; when the LNNB forms, cloud top heights (LNB, at least) may be lifted by several hundreds of meters while only raising CAPE by a minute amount. However, at least one feedback mechanism may decrease the sensitivity of clouds to the LNNB. Given the case of a cloud for which the LNB is located at the bottom of an LNNB (i.e., z_0 is close to the LNB), the cloud top may be lifted by several hundreds of meters by the LNNB, but subsequent radiative processes may then produce a warm/cold dipole at greater altitude and increase z_0–in which case the LNNB can cease to exist (see Figure 3.3).

A general comment: the LNNB forms in atmospheric conditions that approach superadiabatic lapse rates (see Figure 3.3). This may imply that the LNNB is a short-lived feature which is “consumed” by convective instability. At the same time, the formation of the LNNB is consistent with results from Section 1.1 and Section 2.1.

One advantage of a simple approach like this one is that the effects of the warm core and of the cooling aloft can be studied separately. In the real atmosphere, both occur at the same time, but here, the idealized profiles in Figure 3.2 can be adapted so that only the warming, or only the cooling act at once, or both. Figure 3.6 shows how the LNB evolves and how the LNNB may form when warming and cooling act separately, in the case of undilute updrafts ($\lambda = 0\,\%\,\mathrm{km}^{-1}$). As a first observation, when the warming acts alone, the LNB is only affected when z_0 is above the control LNB ($13.01\,\mathrm{km}$). This is because when there is no cooling above z_0, and when z_0 is below the LNB, the effect of the warming is primarily a decrease in CAPE with no change in the intersection of T_{Ve} and T_{Vp} (except for the largest value of m when the distance between the LNB and z_0 is relatively small). The opposite is true of the cooling; when acting alone, it can only affect the LNB when it is present near the LNB. When acting alone, either the warming or cooling do not produce a substantial LNNB (see the single hatching in Figure 3.6a-b), but when acting

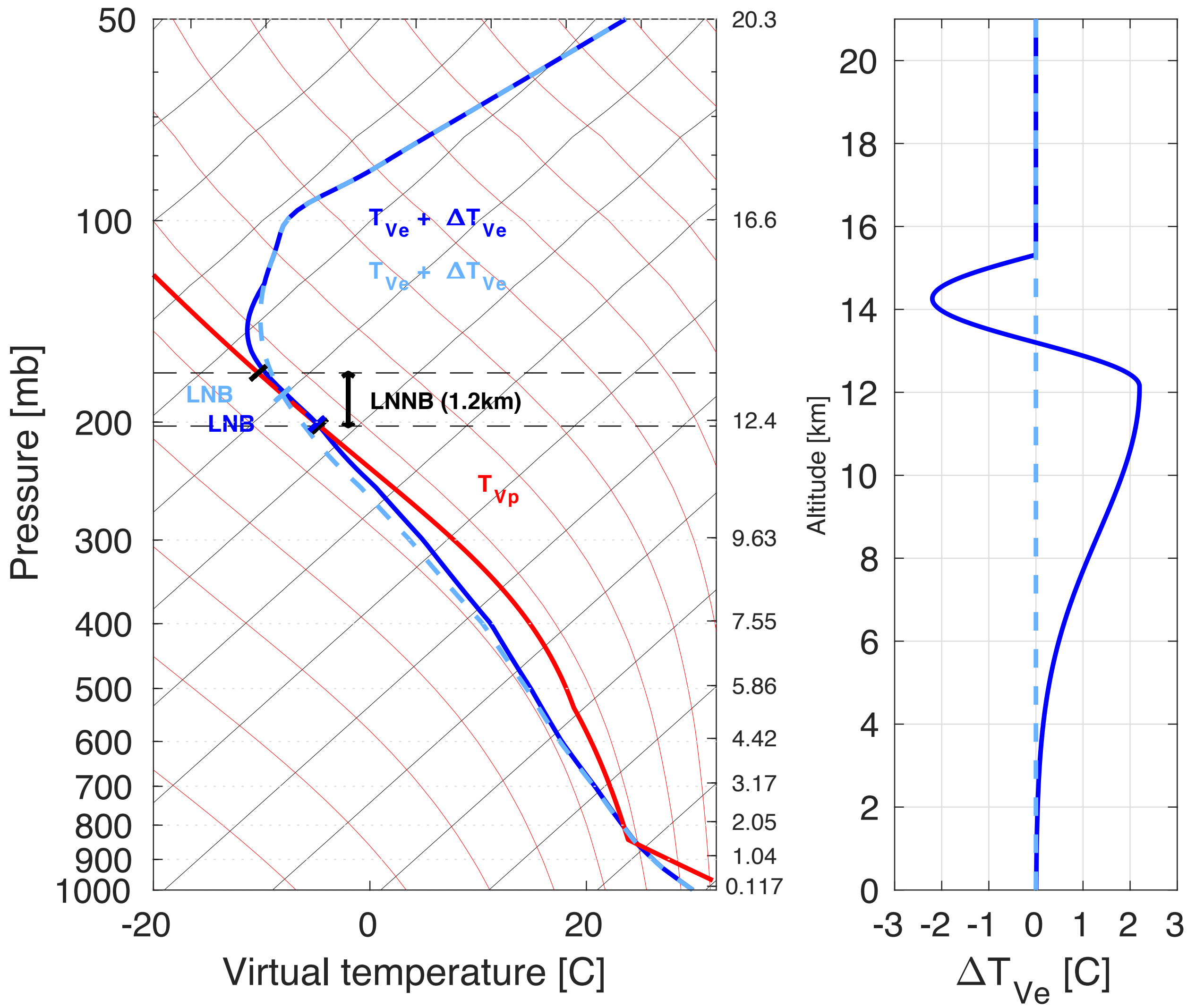

Figure 3.5: Skew-T diagrams for T_{Vp} (red) and T_{Ve} (blue shades) demonstrating the formation of an LNNB near the LNB when m increases. The dashed blue line shows T_{Ve} when $m = 0$, and the solid blue line shows T_{Ve} when $m = 2.2\,\mathrm{K}$ and $z_0 = 13.2\,\mathrm{km}$ (solid blue curve in the right side panel, also corresponding to the white hollow circle in Figure 3.3a. The LNNB is defined with the same T_V and Γ thresholds as in the text.

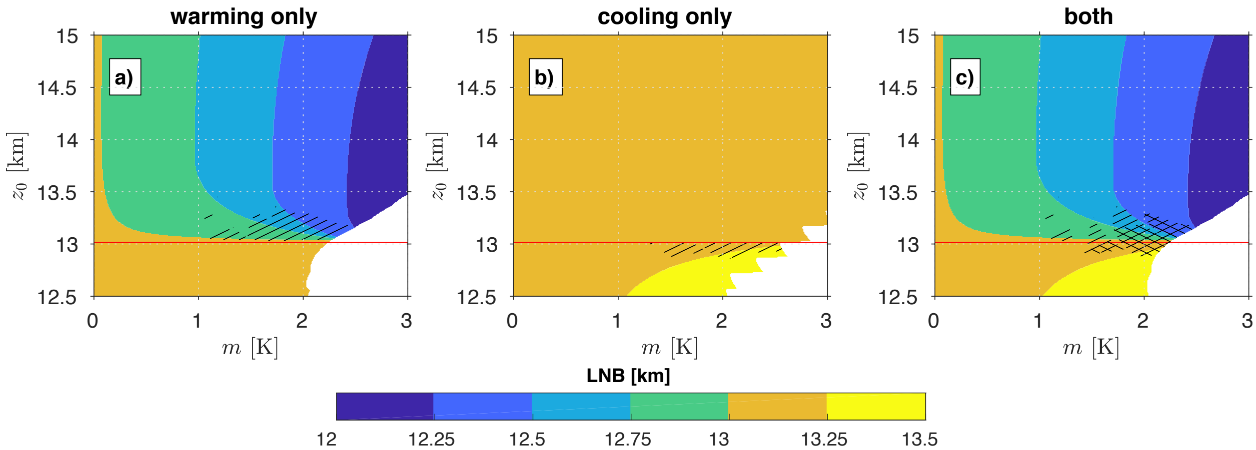

Figure 3.6: LNB (shaded) as a function of m and z_0 with entrainment rate $\lambda = 0\,\%\,\mathrm{km}^{-1}$ when **a)** only the warming, **b)** only the cooling, and **c)** both are present. The red lines indicate the control LNB (when $m = 0$, z_0 being irrelevant then). Areas with single black hatching indicate that a layer of near-neutral buoyancy (LNNB) forms around the LNB. The hatching is doubled when the LNNB is at least $1000\,\mathrm{m}$ deep. Areas of the $\{m,z_0\}$ parameter space that lead to the formation of superadiabatic layers ($\Gamma > 9.8\,\mathrm{K\,km}^{-1}$) appear white.

together, a deeper LNNB may form. This is expected, since the LNNB is the result of lapse rate anomalies in the environment, and since these anomalies are largest when both warming and cooling are present.

For the undilute case $\lambda = 0\,\%\,\mathrm{km}^{-1}$, the effects of warming and cooling on the behavior of the LNB are simply superposed; when the LNB occurs within the cooling (warming, respectively), only the magnitude and position of the cooling (warming) may affect the LNB. For the dilute case ($\lambda \neq 0$, not shown) "non-local" effects arise; for instance, moderate entrainment of environmental air from the warm core into the parcel may lead to slightly elevated Γ_p, and a correspondingly lifted LNB when z_0 is below the control LNB. However, these non-local effects are small (of order $10-100\,\mathrm{m}$) and only become appreciable ($\sim$$250\,\mathrm{m}$) when both warming and cooling are taken into account—at least, that is the prediction from parcel theory.

3.3 Testing parcel theory predictions with idealized simulations

The predictions for the behavior or convective clouds evolving within the average TC are now compared against the simulated behavior from warm bubble experiments. The choice of starting the comparison using only very simple tools is motivated by the level of complexity in processes that act within TCs. The goal here is to compare a basic predicted behavior with a more realistic, simulated behavior—simulated behavior which is designed so that the complex influences of radiation, wind shear, rotation, etc, are removed. These complex influences could be progressively introduced to warm bubble experiments (see Section 3.3), but a judicious choice is to start with none of these influences. To this end, idealized warm bubble experiments were run using CM1 with the following setup:

Table 3.2: Model setup description for the warm bubble simulations

Domain size	:	$25\,\mathrm{km}\times 25\,\mathrm{km}\times 35\,\mathrm{km}$, W×D×H
Horizontal resolution	:	fixed, $250\,\mathrm{m}$
Vertical resolution	:	variable, $10\,\mathrm{m}$ near the ground, progressively stretched to $150\,\mathrm{m}$
Sponge layer	:	Newtonian damping towards base state between $28-35\,\mathrm{km}$ with e-folding time $300\,\mathrm{s}$
Vertical boundary condition	:	open radiative scheme (energy can leave the domain so it does not affect the solution in non-physical ways by reflecting against the model's edge)
Radiation scheme	:	simple relaxation term based on Rotunno and Emanuel (1987)
Initial state	:	– $4\,\mathrm{K}$ warm bubble centered at the ground, vertical radius $1\,\mathrm{km}$, horizontal radius $5\,\mathrm{km}$ – fixed $301.15\,\mathrm{K}$ sea surface temperature (no slab) – COSMIC-Dunion initial sounding (Section 2.2.2) – temperature anomalies with variable m and z_0 (see text)

55 simulations are initially run, one control simulation with no environmental disturbances $(m = 0)$, and 18 experiments spanning the parameter space: $\Big\{\big(m = 0.5\,,\,1\,,\,1.5\,,\,2\,,\,2.5\,,\,3\,\mathrm{K}\big)\,;\,\big(z_0 = 13\,,\,14\,,\,15\,\mathrm{km}\big)\Big\}$

The simulations are run for $3\,\mathrm{h}$ in order to let the moist updrafts develop and reach a steady state. The basic structure of the warm bubble and its evolution are illustrated in Figure 3.7. Initially, the warm bubble is visible below $1\,\mathrm{km}$ altitude along with a fountain-like weak circulation spanning the troposphere (Figure 3.7b). When the simulation is started, the superadiabatic lapse rate near the surface is quickly eroded as the warm bubble rises and starts releasing latent heat via condensation. About half an hour later (Figure 3.7c), the maximum height of the ice cloud formed during ascent reaches the tropopause. At this point in time, the moist updraft takes on a dipolar structure with cooling near the top of the ice cloud. This cooling can only be due to dynamical processes since no radiation scheme is used and since the time scale of the simulations is much shorter than radiative-convective equilibrium time scales. Below the cooling, several torus-shaped rolls form as a butterfly-shaped circulation develops throughout the troposphere and into the lower stratosphere. The tropopause dips down towards the cold top of the cloud as subsidence occurs in the lower stratosphere. As the cloud continues to evolve, the circulation diminishes to a simmer and an anvil-like feature develops in the upper troposphere, with several secondary anvil-shaped protrusions along the side of the cloud in the middle troposphere. While in appearance similar to a nuclear mushroom cloud, the cloud is the product of the release of an amount of energy of order $1\,\mathrm{GJ}$, compared to the $\sim$$150\,\mathrm{GJ}$ that an area the size of the warm bubble can receive in solar energy in a day.

The time series of cloud top height (Figure 3.7a) reveals the occurrence of oscillations in the cloud top near the tropopause. This is associated with gravity waves spreading into the stratosphere, from the cloud top upward. During the first oscillation, the warm bubble reaches a level at which it is not buoyant anymore, resulting in the oscillation. Just before the second oscillation, an intense secondary updraft develops throughout the troposphere, likely resulting in the second oscillation of the cloud top to be lifted by $\sim$$1\,\mathrm{km}$. Since the moist updrafts seems to be undergoing processes that are not captured by parcel theory after the first oscillation (likely, the secondary release of latent heat), the state of the simulated atmosphere at the time of the first oscillation will be used to diagnose a proxy for the LNB. This is assuming that the warm bubble does not at first overshoot its LNB, assumption which is discussed later on.

The lens of cold air topping the cloud (Figure 3.7c) is worth some discussion. Cooling may partly come from adiabatic expansion of air above the warm bubble (where latent heat release may take some time to counteract the cooling) or from rapid compression of a layer of air near the top of the warm bubble (resulting in increased density). Since neither effect is represented in parcel theory, the height of the ice/liquid water cloud, determined itself using an arbitrary

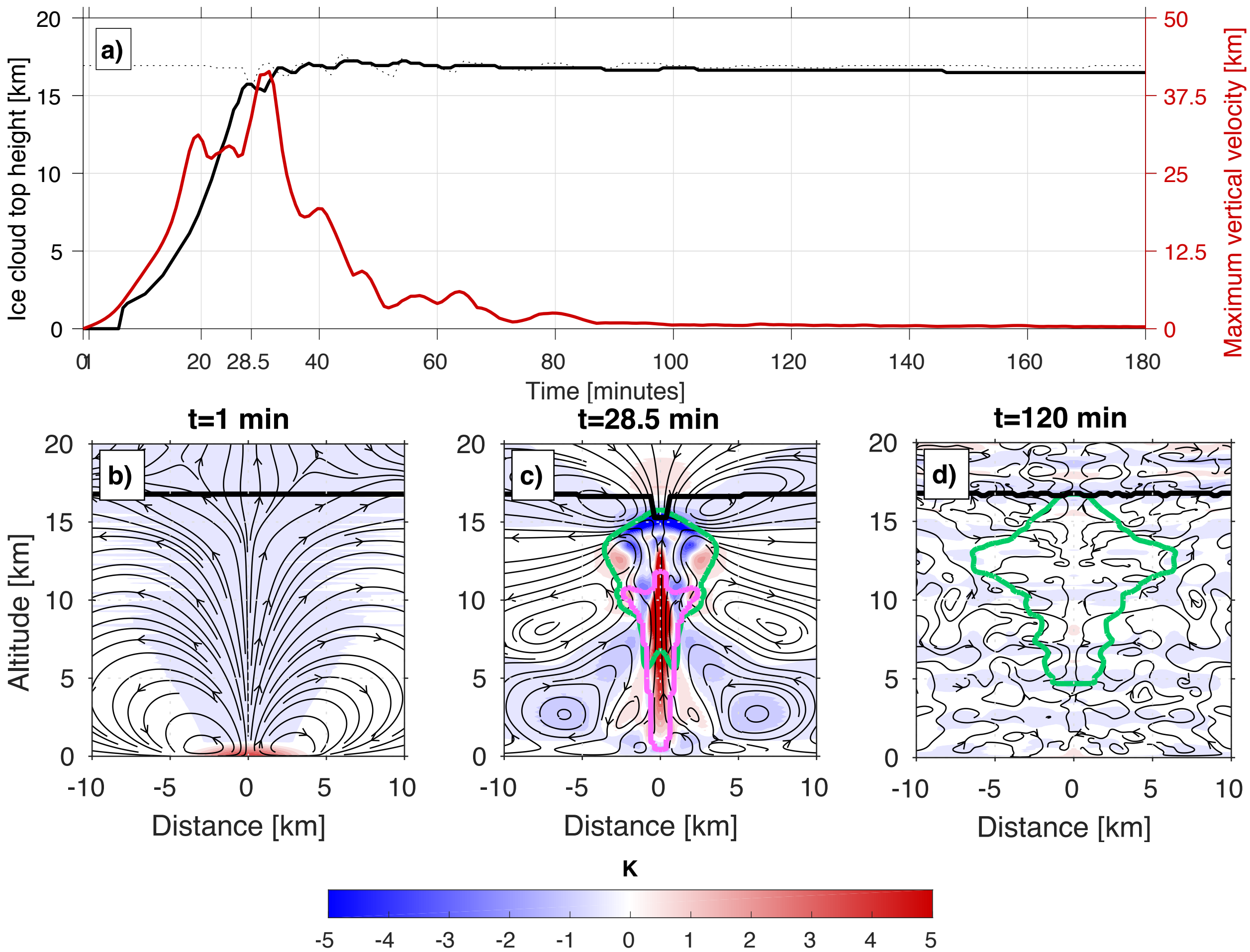

Figure 3.7: a): Time series of the cloud top height (black), height of the cold point tropopause (dotted), and maximum vertical velocity (red). **b)** through **d)**: Temperature anomalies relative to the environmental initial profile (shaded), wind field (black curvy arrows), edge of the ice water cloud (green) and of the liquid water cloud (pink). Cloud boundaries are defined using a $1 \times 10^{-6}\,\mathrm{kg\,kg^{-1}}$ threshold.

threshold, should not be used to determine the LNB. Instead, a more dynamically-relevant diagnosis should be used. Figure 3.8 compares the theoretical LNB against three diagnoses of the simulated LNB, namely:

- For the sake of comparison; the first occurrence of a local maximum in the **height of the cloud top**, as defined by the greatest altitude at which either the ice or liquid cloud water content is larger or equal to $1 \times 10^{-6}\,\mathrm{kg\,kg^{-1}}$.

- The first occurrence of a local maximum in the height at which the largest temperature anomaly relative to the base state occurs. This corresponds to the **center of the warm bubble**. (note: when the vertical profile of temperature anomaly exhibits several local maxima, the center of the warm bubble is assigned that maximum which is closest in altitude to the maximum for the previous integration time step.)

- The first occurrence of a local maximum in the height at which the temperature anomaly becomes negative above the warm bubble center. This corresponds to the **top of the warm bubble**.

The time series in Figure 3.8a shows the position of the three LNB diagnoses in relation to temperature anomalies associated with the warm bubble. The diagnosed LNB lies at $15.7\,\mathrm{km}$, $14.1\,\mathrm{km}$, and $13.2\,\mathrm{km}$ when diagnosed using the cloud top, warm bubble top, and warm bubble center, respectively. Comparing with the theoretical LNB for the control case ($m = 0$) which lies near $13\,\mathrm{km}$, diagnosing the LNB using the center of the warm bubble gives the best agreement. While the difference between the warm bubble top and center diagnosis seems small, Figure 3.8b-c-d show poor correlation between the warm bubble top and the theoretical LNB when m and z_0 change. The cloud top method yields large LNBs which are only matched by the LMO for the theoretical moist updraft with very large values of entrainment (not shown). The highly non monotonous behavior of the simulated LNB metrics suggests either that:

- warm bubble simulations react to changes in environmental thermodynamic conditions in complex ways.

- the LNB metrics are not robust enough and may need to be refined using, for instance, data filtering.

- an LNNB forms under certain conditions in the simulations that do not match those predicted by parcel theory (Figure 3.3). Any disagreement with parcel theory for the formation of the LNNB would not be surprising, given that the theoretical LNNB is defined with arbitrary thresholds and that it cannot interact with the lifted parcel in parcel theory.

Given these results, it seems reasonable to state that the basic behavior of clouds as represented by warm bubble simulations may indeed be captured by some diagnostics derived from parcel theory. In this case, the assumption made earlier that the moist updraft does not overshoot its LNB is reasonable; the vertical distance between the theoretical and simulated LNBs is often less than $250\,\mathrm{m}$. Note that the assumption of no overshooting was perhaps not the intuitive or traditional assumption to make. While overshooting convection is relatively rare over the oceans, parcel theory for the moist updraft predicts very large CAPE: in the vicinity of $3000\,\mathrm{J\,kg^{-1}}$. Such large values are often associated with deep, overshooting convection. If the warm bubble does not overshoot its LNB, parcel theory must be modified so that CAPE may be consumed via mixing before the LNB is reached, i.e., convective entrainment should be included. This is where the comparison between diagnosed and theoretical LNB ends; with the formulation of the entrainment rate as it is, the gap between the theoretical LNB and the simple diagnosis described in Figure 3.8 would only widen when entrainment rate increases (see Figure 3.1b for the qualitative effect of entrainment rate on the LNB). Perhaps a more refined diagnosis of the LNB is needed, or perhaps entrainment should be formulated otherwise. Such developments are outside the scope of the study.

The last goal of the study is to evaluate the effect that changing m and z_0 has on cloud structure in the warm bubble simulations. This part of the study deals with the formation of an ice cloud in the upper troposphere (not just the evolution of a warm parcel), therefore, predicted behaviors from parcel theory are not as relevant for comparison. Shifts in the cloud ice water content distribution induced by changes in m and z_0 are illustrated in Figure 3.9 using contoured

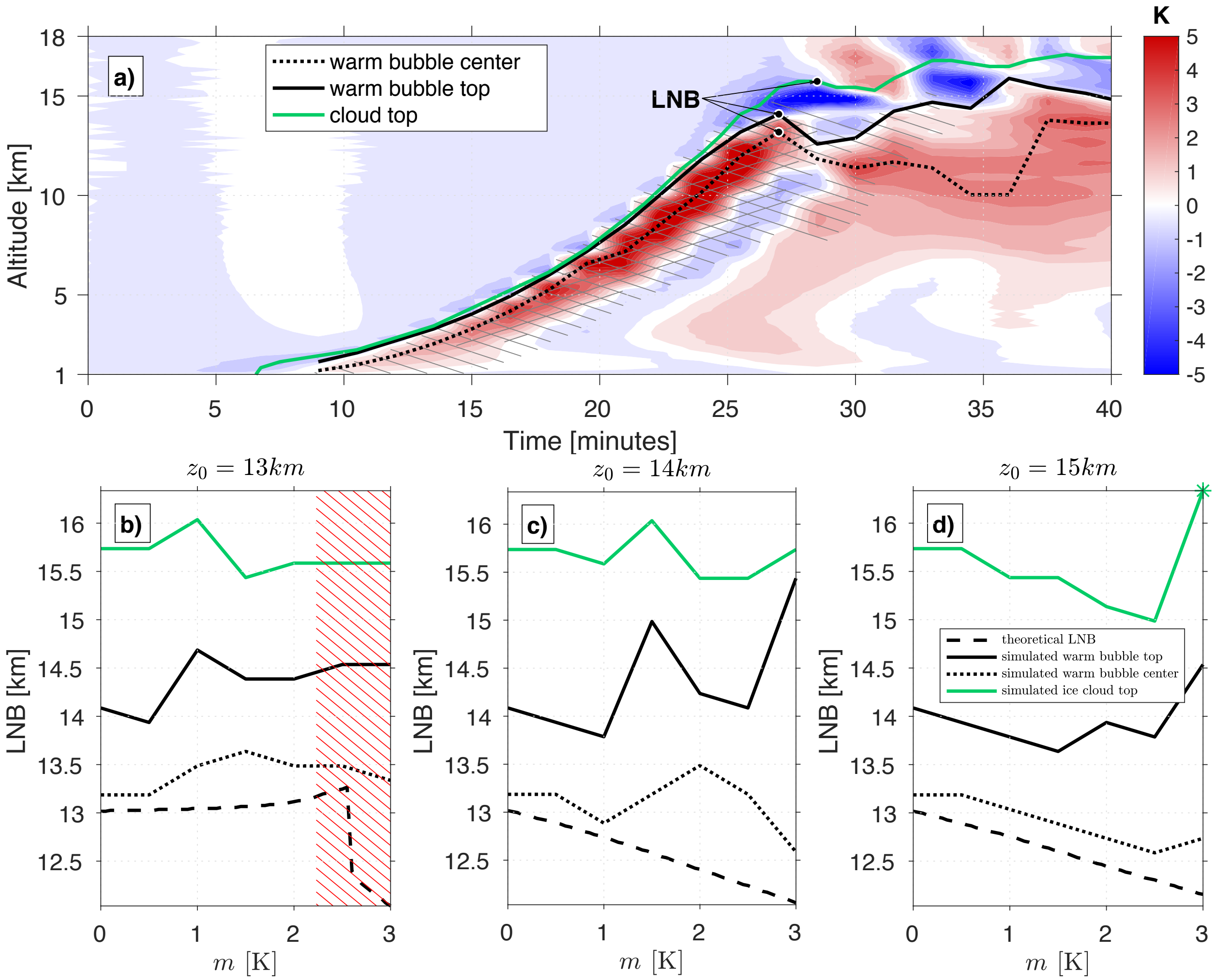

Figure 3.8: **a)** Temperature anomaly from the control simulation ($m = 0$) averaged within $1\,\mathrm{km}$ of the warm bubble's center, as a function of integration time and altitude (shaded). The height of the warm bubble top, center, and of the ice/liquid water cloud are indicated in the legend. The diagnosed height of the LNB in each case is indicated by a black circle. Single (double) hatching indicates that the vertical velocity—averaged within the same area as temperature—is greater than $4\,\mathrm{m\,s^{-1}}$ ($10\,\mathrm{m\,s^{-1}}$). **b)** through **d)** Comparison between the theoretical, undilute LNB (dashed), LNB diagnosed from the top of the warm bubble (black, solid), center of the warm bubble (dotted), and cloud top (green, solid), as a function of m. Red hatching indicates the occurrence of superadiabatic layers in the environmental profile. Likely formation of high-altitude, in situ ice clouds is indicated by green asterisks.

frequency by altitude diagrams (CFAD). The frequency isoline shown is chosen so as to clearly represent the behavior of the main ice cloud without showing too much of the noisy behavior of secondary, wispier cloud features. The typical boomerang shape of the distributions is visible, showing that the main ice cloud is most dense above $\sim 10\,\mathrm{km}$. Smaller features in the middle troposphere reveal the presence of thinner cloud features which may be the results of mixing with the environment in the trailing rolls that develop near the bottom edge of the warm bubble, however, these are not the primary focus of the present analysis.

The top row in Figure 3.9 shows the distributions for the ice cloud when it just reaches its LNB, i.e., the distributions relevant to the primary cloud which forms in the simulations (the one most directly relevant to parcel theory). Generally speaking, the larger m the larger the shifts in the distributions. Near the top of the cloud, the downward shift in the distribution reveals that large m values tend to produce lower clouds, except for specific values of m (more discussion about this later on). At the same time, the shift to the right in the middle troposphere indicates a denser cloud there. Together these shifts indicate that increasing m produces more compact clouds (shorter but more dense). This is consistent with the buoyancy of the warm bubble being reduced when the environmental troposphere is warmer. In the uppermost troposphere (near $16\,\mathrm{km}$), isolated ice cloud occurrence shows in situ ice clouds which form when the upper troposphere is cold enough (large m) and air masses lifted by gravity waves produce ice crystals. In some simulations, this general behavior does not apply. Namely, when $\{m; z_0\}$ is $\{1\,\mathrm{K}; 13\,\mathrm{km}\}$, $\{1.5\,\mathrm{K}; 14\,\mathrm{km}\}$, $\{3\,\mathrm{K}; 14\,\mathrm{km}\}$, and $\{3\,\mathrm{K}; 15\,\mathrm{km}\}$. In these simulations, tropospheric warming and upper tropospheric cooling seem to interact with the cloud in ways that produce an elevated cloud top (also visible in Figure 3.8b-d).

The bottom row in Figure 3.9 shows the distributions for the ice cloud at long integration times, i.e., the cloud that has exhausted latent heat and begins to slowly dissipate. Consistent with the dissipation, overall smaller ice mixing ratios are observed throughout the troposphere. The in situ formation of clouds just below the tropopause is still visible. A new feature develops near $14\,\mathrm{km}$: a "tongue" of lower ice mixing ratios in continuity with the main cloud. This corresponds to the mixing of cloudy and environmental air where the cloud detrains, i.e., the anvil near the level of neutral buoyancy. The ice mixing ratio decreases with height within the anvil, perhaps indicating that environmental air is mixed into the anvil from the top, rather than from the bottom. Several simulations with $z_0 = 13\,\mathrm{km}$ display a thick and elevated anvil. The simulations with $\{m$; $z_0\}$ = $\{1.5\,\mathrm{K};\,14\,\mathrm{km}\}$ and $\{3\,\mathrm{K};\,14\,\mathrm{km}\}$ show no anvil. Rather, they show an elevated cloud top (as pointed out earlier) that is subject to marginal mixing with the environment.

While it would seem straightforward for clouds with an initially elevated cloud top to later develop an elevated anvil, this behavior is not the one observed. Instead, some elevated clouds develop no anvil, while clouds with lower tops initially later develop an elevated anvil. In order to better understand how these behaviors arise, the warming and cooling are introduced separately in a new set of simulations. Simulations spanning the following parameter space are run:

$\Big\{(m = 0.5\,,\,1\,,\,1.5\,,\,2\,,\,2.5\,,\,3\,\mathrm{K});(z_0 = 13\,,14\,,15\,\mathrm{km});(\text{warming alone, cooling alone})\Big\}$

The results are shown in Figure 3.10 and Figure 3.11. For clarity, the interpretation of the results is laid out as a list:

1. Warming alone:

    - Has overall "monotonous" effects: the cloud top height only decreases with increasing m.

    - Decreases the cloud top height at short and long lead times, with little sensitivity to z_0 (consistent with predictions).

    - Raises the anvil when z_0 is below the anvil (consistent with the destabilization occurring above z_0), and inhibits anvil development when z_0 is above the anvil (consistent with the anvil spreading in a warmer environment).

2. Cooling alone:

    - Has overall "monotonous" effects: the cloud top height only increases with increasing m.

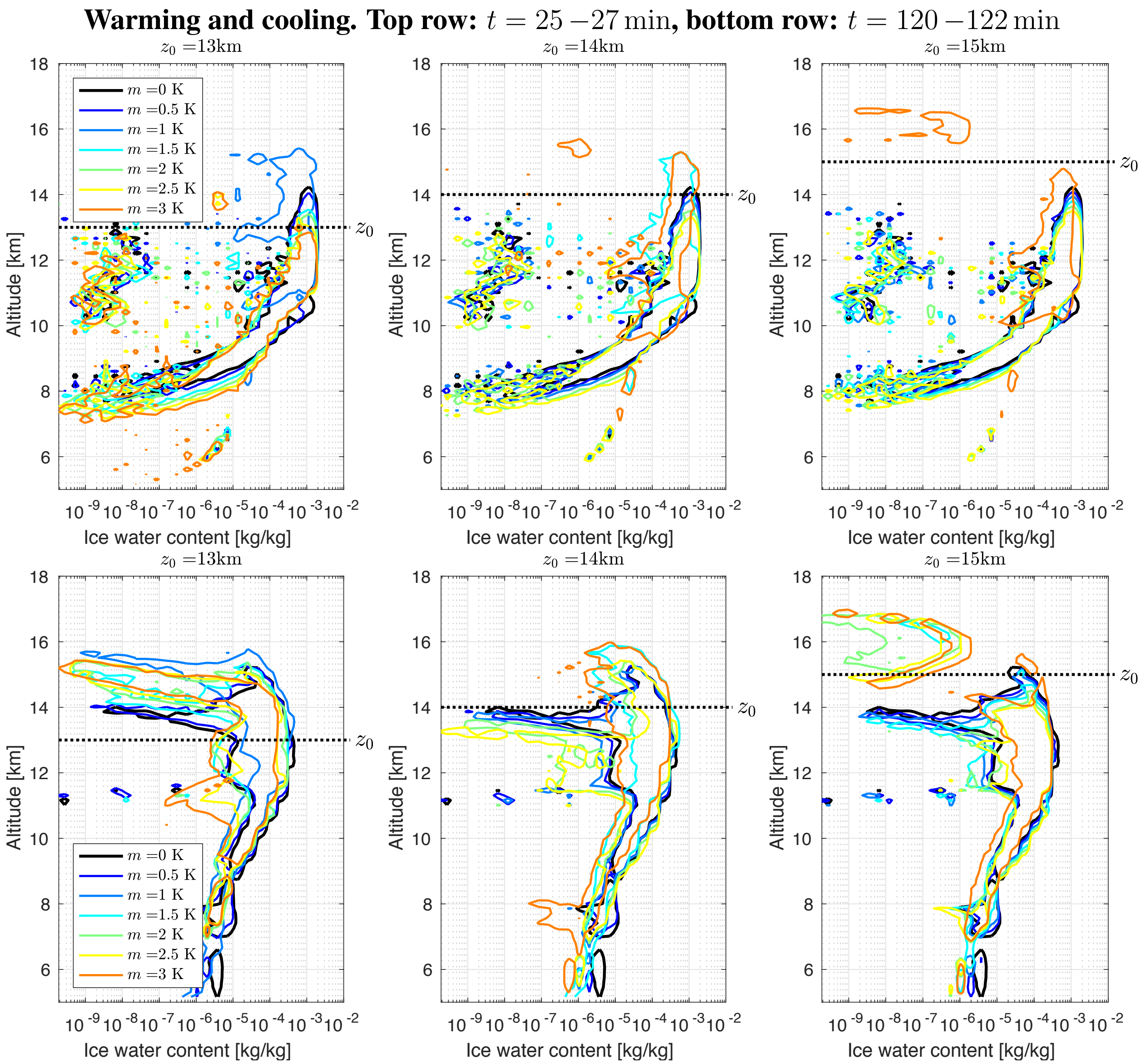

Figure 3.9: Contoured frequency by altitude diagram (CFAD) of cloud ice water content. Data are from warm bubble simulations for z_0 in $\{13,\ 14,\ 15\,\text{km}\}$ (indicated as a black dashed line) and for m in $\{0\,,\ 0.5\,,\ 1\,,\ 1.5\,,\ 2\,,\ 2.5\,,\ 3\,\text{K}\}$ (see color scheme in the legend), within the $5{\times}5\,\text{km}$ box around the center of the model domain, and for integrations times $25-27\,\text{min}$ (top row) and $120-122\,\text{min}$ (bottom row). The frequency is the number of sample in each ice water content, altitude sampling box divided by the total number of sample for each simulation. The 0.01 frequency isoline is shown.

- Has very little effect on cloud top height at short lead times (inconsistent with predictions from parcel theory).
- Tends to increase cloud top and anvil height at long lead times, except when z_0 is near the cloud top, in which case the cloud top height decreases and anvil formation is inhibited.
- Enhances the formation of in situ clouds.
- Interestingly, has an effect on ice distributions in the troposphere at long lead times.

These results do not always corroborate predictions from parcel theory. At the moment, given that warming and cooling alone produce monotonous changes, it remains unclear how non monotonous behaviors may arise when both warming and cooing act together. One way to further disentangle the influences of warming and cooling is to analyze CFADs for the vertical wind field (not shown), which can help separate the effects of dynamics and microphysics. Upper level cooling leads to slight increases in upward average wind velocities above z_0, while the magnitude of transient and stronger updrafts is reduced. Generally speaking, the presence of a warm core leads to reduced upward average wind velocities below $z_0 - \sigma_C/2$, and increased upward average wind velocities can be found above $z_0 - \sigma_C/2$, consistent with the change in static stability introduced to the environment by the structure of the idealized warm core. The magnitude of downdrafts below $10\,\mathrm{km}$ is sometimes increased by the presence of the warm core. More complex effects are also seen that require future work to interpret. When upper level cooling and the warm core are present at the same time, the simulations that present the largest differences in Figure 3.9 also display large differences: for instance, the simulation with $z_0 = 13\,\mathrm{km}$ and $m = 1\,\mathrm{K}$ exhibits updrafts at higher altitudes than the rest of the simulations, consistent with the presence of ice at higher altitudes seen in Figure 3.9. The reasons why cloud development differs vastly given small changes in environmental parameters remain unknown at present, and suggest the need for more research. It is possible that certain combinations of environmental parameters lead to the development of the LNNB in the warm bubble simulations. This possibility is inherently difficult to investigate given the differences that exist between the predictions from parcel theory and the warm bubble simulations, and given the parcel theory-based definition of the LNNB. It may be useful to base the definition of the LNNB on the vertical structure of static stability.

The results presented here show that the qualitative behaviors predicted by parcel theory are not always found in idealized simulations that otherwise display general similarities with parcel theory. It appears that cloud development is impacted in highly nonlinear ways by the thermal structure of the environment, which may be indicative of entrainment processes. The response of clouds with increasing z_0, which is analog to increasing integration time in TC simulations (see Figure 3.2), suggests that a negative feedback may exist between cloud top height and z_0 (time). Testing this would require progressively adding levels of complexity to the warm bubble simulations to include more elements of the TC circulation.

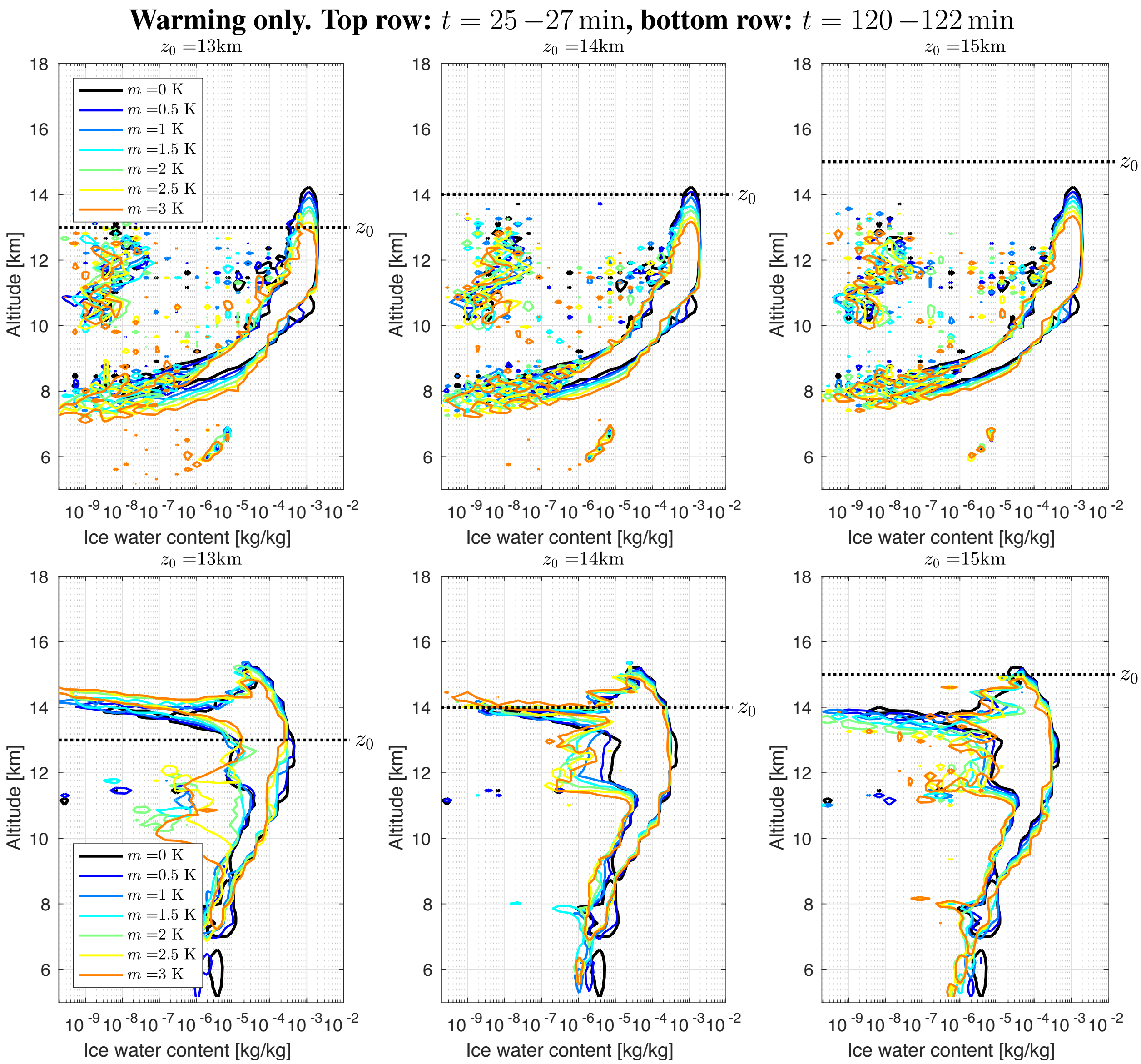

Figure 3.10: Same as Figure 3.9 but with only tropospheric warming acting in the environment.

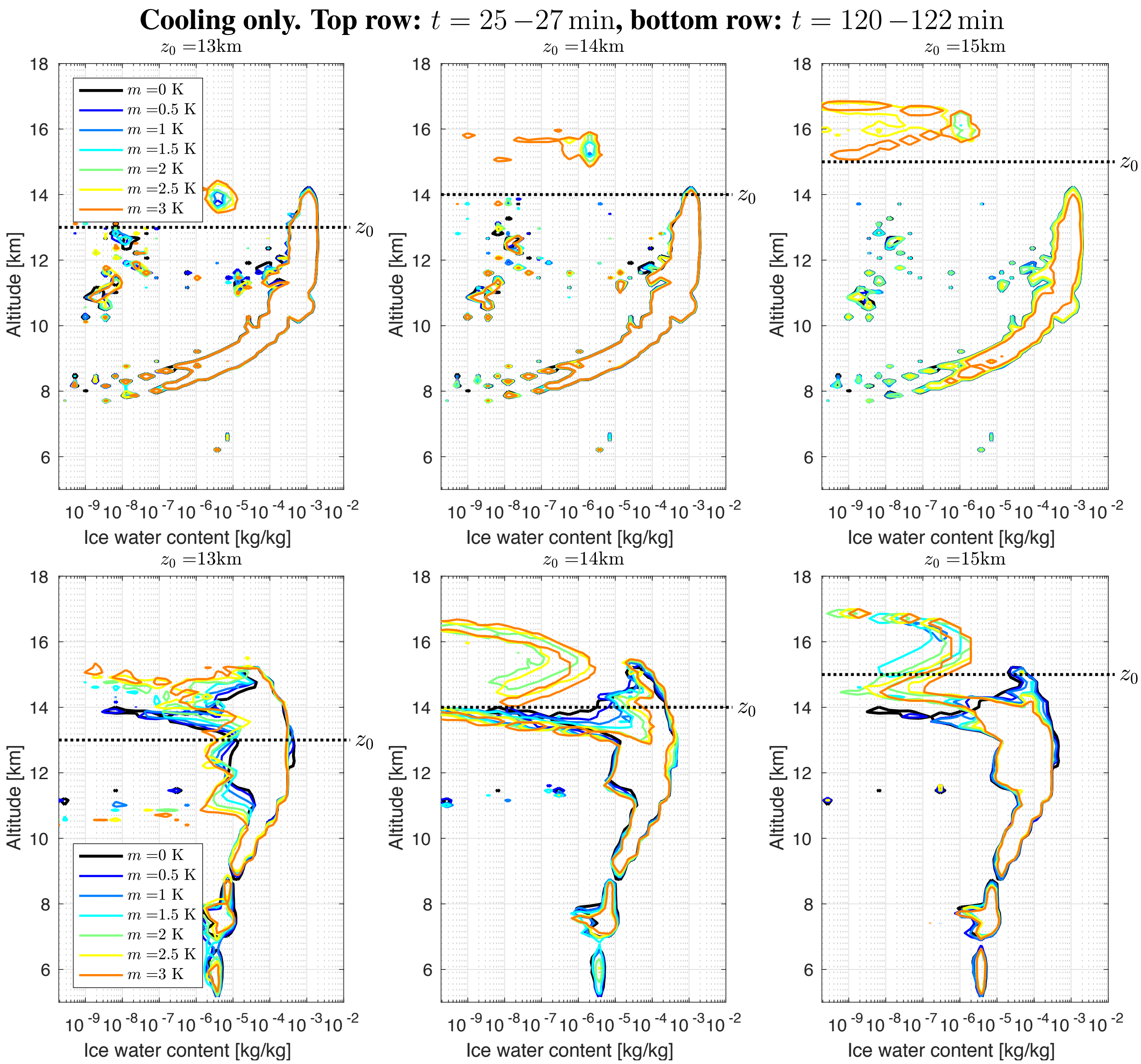

Figure 3.11: Same as Figure 3.9 but with only upper tropospheric cooling acting in the environment.

Conclusions and discussion

In this work, observational data, reanalysis data sets, numerical simulations, and theoretical approaches have been used to provide elements of answer to the questions:

1. What is driving the temperature of the tropopause layer in tropical cyclones?
2. Which feedbacks exist between the temperature of the tropopause and the structure and dynamics of tropical cyclones?

Main results and future work are discussed.

Summary and discussion of fundamental results

The high-resolution, updated characterization of TLC provided in Chapter 1 shows that cold air is found on meso- to synoptic scales above TCs, implying that TLC be produced locally and exported to larger scales and/or produced on large scales directly. Reanalyses are able to capture TLC in terms of magnitude and spatial extent, although the evolution of the signal over the lifetime of TCs is not always captured properly. At present, the quality of the representation in reanalysis data sets may not suffice to explain the behavior of TLC during the extratropical transition of TCs and their decay. However, reanalyses were able to provide clues about the mechanisms for TLC, namely, that TLC must have a large-scale, hydrostatic component, and that TLC scales like the tropospheric warm core of TCs (in the reanalyses).

The latest A-train products provided vertically-resolved radiative heating rate estimates within TCs, of which the analysis in Chapter 2 Section 2.1 suggests that even in TCs where deep convection reaches the upper troposphere and lower stratosphere the most (out of all marine convective systems), cloud top heights are not high enough on scales large enough to explain TLC. In the very inner core of TCs, near the eyewall, deep convective clouds may reach the stratosphere often enough to explain up to $50\,\%$ of TLC locally, however, the amount of cooling explained by cloud radiative processes over the majority of the area covered by TCs remains marginal. This result is important in light of the analysis in Chapter 2 Section 2.2. While the

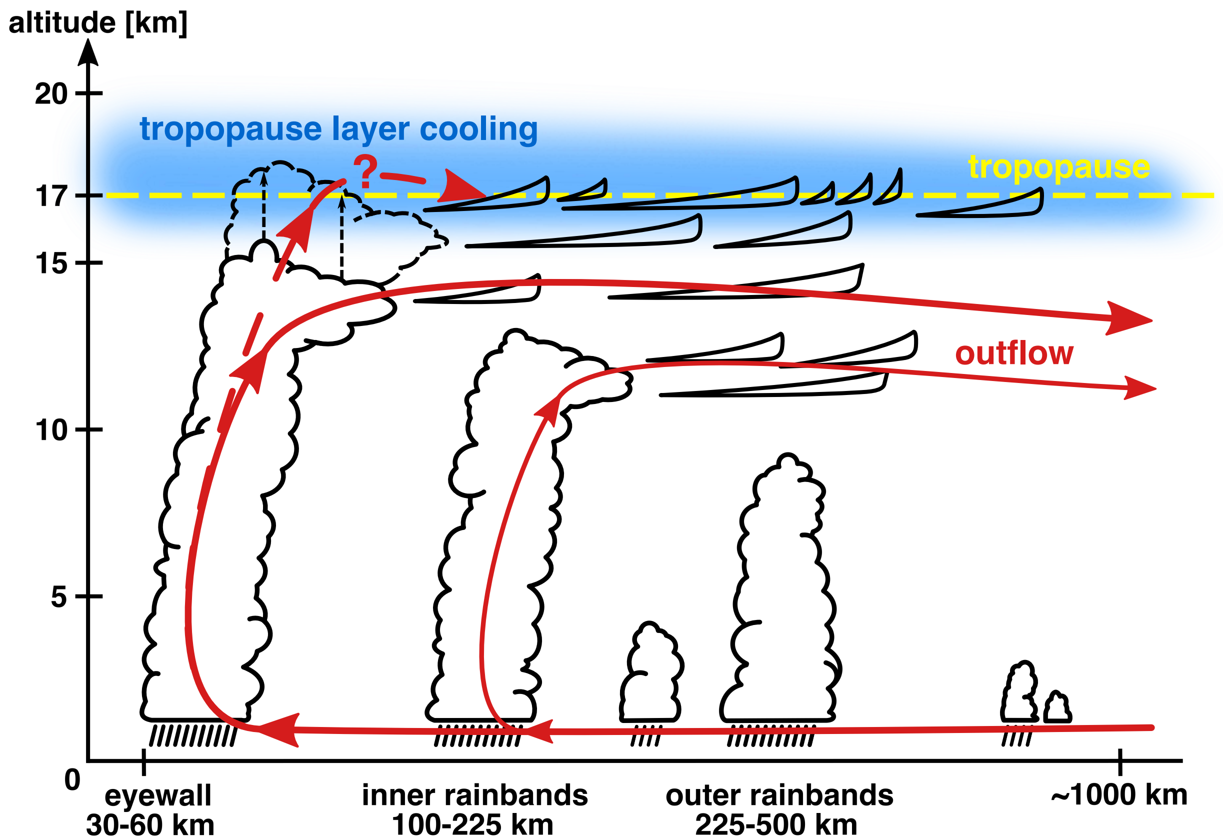

Figure 4.12: Illustration of the TC secondary circulation and typical cloud structure.

secondary circulation was not found to directly produce ascent above $\sim 15\,\mathrm{km}$ in the intense, deep TCs produced by axisymmetric simulations, circulations which are not explained by the balanced vortex model were found that may explain TLC over large areas. Specifically, a thermally indirect circulation was unveiled near the tropopause, producing inflow near the tropopause, and ascent across the tropopause and into the lower stratosphere. The existence of this circulation is supported by observations and modeling studies, and highlights the potential for gradient wind balance to be violated in the upper troposphere of TCs. Given the radial structure that cloud top radiative cooling displays in the lower TTL (stronger cooling near the center), cloud radiative processes may force the outward component of the TC secondary circulation, forcing the outflow layer out of balance.

Finally, hypothesized feedbacks between TLC and the structure and dynamics of TCs were explored in Chapter 3. Parcel theory yielded simple, intuitive behaviors for clouds in the presence of tropospheric warming (the warm core) and tropopause layer cooling. It was found that the warming and cooling act in synergy to produce a layer in the upper troposphere where pseudo-adiabatically lifted air parcels may encounter neutral buoyancy, i.e., a layer which makes the notion of LNB irrelevant. While impossible to diagnose in e.g. model output, this layer was hypothesized to translate to enhanced sensitivity of the cloud top height to environmental disturbances especially when convective entrainment is taken into account, and a decreased Richardson number in the TC outflow layer consistent with recent literature. These results stem from a highly idealized framework, and more work is needed to assess their validity in frameworks more representative of TCs. However, the value of the idealized framework was demonstrated using simple diagnostics to compare predictions from parcel theory with simulated moist updrafts.

Future work

Potential for future research has been mentioned throughout this dissertation. A non-exhaustive list of tasks for future research is laid out below.

1. Diagnose the LNNB in observations and simulations in order to determine the range of conditions in which the LNNB forms, and how the LNNB impacts cloud development. Direct diagnosis not being possible, simulations could be used in which tracked air parcels or a tracer species would be introduced to analyze changes in the cloud top and near cloud top layer corresponding to environmental disturbances favorable to the development of the LNNB. Since tropospheric warming and cooling aloft exist on very large scales in the vicinity of tropical deep convection, such a study could prove valuable to improve our understanding of feedbacks between clouds and their environment, globally.

2. Determine the feedbacks between TLC and the structure and dynamics of the underlying TC by including perturbations to TLC in TC simulations. This could involve forcing TLC to be removed or added to simulations, and may be done by adding a background temperature tendency corresponding to large-scale ascent or subsidence in the model. In essence, a Brewer-Dobson-like circulation could be added to the model setup and either enhance TLC or prevent it from forming. This may require the use of long-running simulations, given the time scales on which circulations of this kind act. In this case, only the TC "steady-state" structure and associated feedbacks may be inferred.

3. Elucidate the role of partial reflection of gravity waves near the bottom of the sponge layer within numerical simulations. Some work has already been done on this topic, however, no model setup was found that offers worthwhile tradeoff between computational cost and quality of the simulation. Gravity waves forced to interact with one another in ways that have no real-world equivalent were found to produce so-called ducted waves, i.e., quasi-steady features that enhance the temperature variability of the tropopause layer. One way to go about this is to use several model setups in which gravity wave activity is expected to be disturbed more or less, and to analyze the momentum forcing associated with eddies in each simulation. The momentum forcing could also be compared to that in 3D simulations in which reflection of gravity waves at the inner radius does not occur, by

construction. Valuable insight may be gained into model requirements for modeling studies focusing on upper-level processes in TCs.

4. Add levels of complexity/realism to warm bubble simulations in order to assess the validity of cloud-TLC feedbacks. This could include warm bubble simulations with horizontal and vertical wind shear representative of the average TC circulation (from, e.g., 2D TC simulations), simulations including low-level convergence and vertical wind like that induced by the TC secondary circulation, and perhaps simulations of TCs in which a nested grid is used to track the evolution of a warm bubble released near the surface.

5. Further use the TC tracks developed for reanalysis data sets to quantify the horizontal structure of TLC and its response to environmental wind shear, its inter-basin and inter-storm variability, etc.

References

Ackerman, T. P., Liou, K.-N., Valero, F. P., & Pfister, L. (1988). Heating rates in tropical anvils. *Journal of the atmospheric sciences*, *45*(10), 1606–1623.

Alcala, C., & Dessler, A. (2002). Observations of deep convection in the tropics using the tropical rainfall measuring mission (TRMM) precipitation radar. *Journal of Geophysical Research: Atmospheres*, *107*(D24), AAC–17.

Angell, J. K., & Korshover, J. (1964). Quasi-biennial variations in temperature, total ozone, and tropopause height. *Journal of the Atmospheric Sciences*, *21*(5), 479–492.

Anthes, R. A., Bernhardt, P., Chen, Y., Cucurull, L., Dymond, K., Ector, D., ... others (2008). The cosmic/formosat-3 mission: Early results. *Bulletin of the American Meteorological Society*, *89*(3), 313–334.

Anthes, R. A., Trout, J. W., & Rosenthal, S. L. (1972). Comparisons of tropical cyclone simulations with and without the assumption of circular symmetry. *Mon. Weather Rev*, *99*(10), 759–766.

Arakawa, H. (1951). Analysis of the tropopause and the stratospheric field of temperature of a mature typhoon. *Papers in Meteorology and Geophysics*, *2*(1), 1–5.

Austin, R. T., Heymsfield, A. J., & Stephens, G. L. (2009). Retrieval of ice cloud microphysical parameters using the cloudsat millimeter-wave radar and temperature. *Journal of Geophysical Research: Atmospheres*, *114*(D8).

Bengtsson, L., Botzet, M., & Esch, M. (1995). Hurricane-type vortices in a general circulation model. *Tellus A*, *47*(2), 175–196.

Biondi, R., Ho, S.-P., Randel, W., Syndergaard, S., & Neubert, T. (2013). Tropical cyclone cloud-top height and vertical temperature structure detection using GPS radio occultation measurements. *Journal of Geophysical Research: Atmospheres*, *118*(11), 5247–5259.

Biondi, R., Randel, W., Ho, S.-P., Neubert, T., & Syndergaard, S. (2012). Thermal structure of intense convective clouds derived from GPS radio occultations. *Atmospheric Chemistry* *and Physics*, *12*(12), 5309–5318.

Birner, T. (2006). Fine-scale structure of the extratropical tropopause region. *Journal of Geophysical Research: Atmospheres*, *111*(D4).

Birner, T., & Charlesworth, E. J. (2017). On the relative importance of radiative and dynamical heating for tropical tropopause temperatures. *Journal of Geophysical Research: Atmospheres*, *122*(13), 6782–6797.

Black, P. G., & Anthes, R. A. (1971). On the asymmetric structure of the tropical cyclone outflow layer. *Journal of the Atmospheric Sciences*, *28*(8), 1348–1366.

Bolton, D. (1980). The computation of equivalent potential temperature. *Monthly weather review*, *108*(7), 1046–1053.

Bosilovich, M. G., & Coauthors. (2015). *MERRA-2: Initial evaluation of the climate*. National Aeronautics and Space Administration, Goddard Space Flight Center.

Browner, S. P., Woodley, W. L., & Griffith, C. G. (1977). Diurnal oscillation of the area of cloudiness associated with tropical storms. *Monthly Weather Review*, *105*(7), 856–864.

Bryan, G. H., & Rotunno, R. (2009). The maximum intensity of tropical cyclones in axisymmetric numerical model simulations. *Monthly Weather Review*, *137*(6), 1770–1789.

Buontempo, C., Flentje, H., & Kiemle, C. (2006). In the eye of a tropical cyclone. *Weather*, *61*(2), 47–50.

Cairo, F., Buontempo, C., MacKenzie, A., Schiller, C., Volk, C., Adriani, A., … others (2008). Morphology of the tropopause layer and lower stratosphere above a tropical cyclone: a case study on cyclone Davina (1999). *Atmospheric Chemistry and Physics*, *8*(13), 3411–3426.

Camargo, S. J., Barnston, A. G., & Zebiak, S. E. (2005). A statistical assessment of tropical cyclone activity in atmospheric general circulation models. *Tellus A: Dynamic Meteorology and Oceanography*, *57*(4), 589–604.

Chen, H., & Zhang, D.-L. (2013). On the rapid intensification of hurricane wilma (2005). part ii: Convective bursts and the upper-level warm core. *Journal of the Atmospheric Sciences*, *70*(1), 146–162.

Corti, T., Luo, B., Peter, T., Vömel, H., & Fu, Q. (2005). Mean radiative energy balance and vertical mass fluxes in the equatorial upper troposphere and lower stratosphere. *Geophysical Research Letters*, *32*(6).

Courtney, J., & Knaff, J. A. (2009). Adapting the Knaff and Zehr wind-pressure relationship for operational use in tropical cyclone warning centres. *Australian Meteorological and Oceanographic Journal*, *58*(3), 167.

Crook, N. A., & Moncrieff, M. W. (1988). The effect of large-scale convergence on the generation and maintenance of deep moist convection. *Journal of the atmospheric sciences*, *45*(23), 3606–3624.

Danielsen, E. F. (1993). In situ evidence of rapid, vertical, irreversible transport of lower tropospheric air into the lower tropical stratosphere by convective cloud turrets and by larger-scale upwelling in tropical cyclones. *Journal of Geophysical Research: Atmospheres*, *98*(D5), 8665–8681.

Davis, N., & Birner, T. (2016). Climate model biases in the width of the tropical belt. *Journal of Climate*(2016).

Dee, D. P., Uppala, S. M., Simmons, A., Berrisford, P., Poli, P., Kobayashi, S., ... others (2011). The ERA-Interim reanalysis: Configuration and performance of the data assimilation system. *Quarterly Journal of the royal meteorological society*, *137*(656), 553–597.

Del Genio, A. D. (2012). Representing the sensitivity of convective cloud systems to tropospheric humidity in general circulation models. *Surveys in geophysics*, *33*(3-4), 637–656.

Demuth, J. L., DeMaria, M., & Knaff, J. A. (2006). Improvement of Advanced Microwave Sounding Unit tropical cyclone intensity and size estimation algorithms. *Journal of Applied Meteorology and Climatology*, *45*(11), 1573–1581.

Demuth, J. L., DeMaria, M., Knaff, J. A., & Vonder Haar, T. H. (2004). Evaluation of Advanced Microwave Sounding Unit tropical-cyclone intensity and size estimation algorithms. *Journal of Applied Meteorology*, *43*(2), 282–296.

Derbyshire, S., Beau, I., Bechtold, P., Grandpeix, J.-Y., Piriou, J.-M., Redelsperger, J.-L., &

Soares, P. (2004). Sensitivity of moist convection to environmental humidity. *Quarterly Journal of the Royal Meteorological Society: A journal of the atmospheric sciences, applied meteorology and physical oceanography*, *130*(604), 3055–3079.

Ditchek, S. D., Molinari, J., & Vollaro, D. (2017). Tropical cyclone outflow-layer structure and balanced response to eddy forcings. *Journal of the Atmospheric Sciences*, *74*(1), 133–149.

Doswell, C. A. I., & Rasmussen, E. N. (1994). The effect of neglecting the virtual temperature correction on CAPE calculations. *Weather and Forecasting*, *9*(4), 625–629.

Doyle, J. D., Moskaitis, J. R., Feldmeier, J. W., Ferek, R. J., Beaubien, M., Bell, M. M., … others (2017). A view of tropical cyclones from above: The Tropical Cyclone Intensity Experiment. *Bulletin of the American Meteorological Society*, *98*(10), 2113–2134.

Dunion, J. P. (2011). Rewriting the climatology of the tropical North Atlantic and Caribbean Sea atmosphere. *Journal of Climate*, *24*(3), 893–908.

Duran, P., & Molinari, J. (2018). Dramatic inner-core tropopause variability during the rapid intensification of Hurricane Patricia (2015). *Monthly Weather Review*, *146*(1), 119–134.

Emanuel, K., & Rotunno, R. (2011). Self-stratification of tropical cyclone outflow. Part I: Implications for storm structure. *Journal of the Atmospheric Sciences*, *68*(10), 2236–2249.

Emanuel, K. A. (1991). The theory of hurricanes. *Annual Review of Fluid Mechanics*, *23*(1), 179–196.

Emanuel, K. A. (1994). *Atmospheric convection*. Oxford University Press on Demand.

Flatau, M., & Stevens, D. E. (1993). The role of outflow-layer instabilities in tropical cyclone motion. *Journal of the atmospheric sciences*, *50*(12), 1721–1733.

Frank, W. M. (1977). The structure and energetics of the tropical cyclone I. Storm structure. *Monthly Weather Review*, *105*(9), 1119–1135.

Fritsch, J., & Brown, J. (1982). On the generation of convectively driven mesohighs aloft. *Monthly Weather Review*, *110*(11), 1554–1563.

Fu, Q., & Liou, K. (1992). On the correlated k-distribution method for radiative transfer in nonhomogeneous atmospheres. *Journal of the Atmospheric Sciences*, *49*(22), 2139–2156.

Fueglistaler, S., Dessler, A., Dunkerton, T., Folkins, I., Fu, Q., & Mote, P. W. (2009). Tropical tropopause layer. *Reviews of Geophysics*, *47*(1).

Gettelman, A., Forster, P. M. d. F., Fujiwara, M., Fu, Q., Vömel, H., Gohar, L. K., ... Ammerman, M. (2004). Radiation balance of the tropical tropopause layer. *Journal of Geophysical Research: Atmospheres*, *109*(D7).

Gettelman, A., Hoor, P., Pan, L., Randel, W., Hegglin, M., & Birner, T. (2011). The extratropical upper troposphere and lower stratosphere. *Reviews of Geophysics*, *49*(3).

Gettelman, A., Salby, M., & Sassi, F. (2002). Distribution and influence of convection in the tropical tropopause region. *Journal of Geophysical Research: Atmospheres*, *107*(D10), ACL–6.

Goldberg, M. D., Crosby, D. S., & Zhou, L. (2001). The limb adjustment of AMSU-A observations: Methodology and validation. *Journal of Applied Meteorology*, *40*(1), 70–83.

Hahn, C. J., & Warren, S. G. (1999). *Extended edited synoptic cloud reports from ships and land stations over the globe, 1952-1996* (Tech. Rep.). Oak Ridge National Lab., TN (US).

Hannah, W. M. (2017). Entrainment versus dilution in tropical deep convection. *Journal of the Atmospheric Sciences*, *74*(11), 3725–3747.

Hartmann, D. L., Holton, J. R., & Fu, Q. (2001). The heat balance of the tropical tropopause, cirrus, and stratospheric dehydration. *Geophysical Research Letters*, *28*(10), 1969–1972.

Hawkins, J. D., Turk, F. J., Lee, T. F., & Richardson, K. (2008). Observations of tropical cyclones with the ssmis. *IEEE Transactions on Geoscience and Remote Sensing*, *46*(4), 901–912.

Haynes, J. M., L'Ecuyer, T. S., Stephens, G. L., Miller, S. D., Mitrescu, C., Wood, N. B., & Tanelli, S. (2009). Rainfall retrieval over the ocean with spaceborne w-band radar. *Journal of Geophysical Research: Atmospheres*, *114*(D8).

Henderson, D. S., L'Ecuyer, T., Stephens, G., Partain, P., & Sekiguchi, M. (2013). A multisensor perspective on the radiative impacts of clouds and aerosols. *Journal of Applied Meteorology and Climatology*, *52*(4), 853–871.

Heus, T., & Jonker, H. J. (2008). Subsiding shells around shallow cumulus clouds. *Journal of the

Atmospheric Sciences, *65*(3), 1003–1018.

Heymsfield, G. M., Halverson, J. B., Simpson, J., Tian, L., & Bui, T. P. (2001). ER-2 Doppler radar investigations of the eyewall of Hurricane Bonnie during the Convection and Moisture Experiment-3. *Journal of Applied Meteorology*, *40*(8), 1310–1330.

Hobgood, J. S. (1986). A possible mechanism for the diurnal oscillations of tropical cyclones. *Journal of the atmospheric sciences*, *43*(23), 2901–2922.

Hodges, K. (1994). A general method for tracking analysis and its application to meteorological data. *Monthly Weather Review*, *122*(11), 2573–2586.

Hodges, K. (1995). Feature tracking on the unit sphere. *Monthly Weather Review*, *123*(12), 3458–3465.

Hodges, K. (1999). Adaptive constraints for feature tracking. *Monthly Weather Review*, *127*(6), 1362–1373.

Hodges, K., Cobb, A., & Vidale, P. L. (2017). How well are tropical cyclones represented in reanalysis datasets? *Journal of Climate*, *30*(14), 5243–5264.

Holland, G. J., & Merrill, R. T. (1984). On the dynamics of tropical cyclone structural changes. *Quarterly Journal of the Royal Meteorological Society*, *110*(465), 723–745.

Holloway, C. E., & Neelin, J. D. (2007). The convective cold top and quasi equilibrium. *Journal of the Atmospheric Sciences*, *64*(5), 1467–1487.

Horn, M., Walsh, K., Zhao, M., Camargo, S. J., Scoccimarro, E., Murakami, H., … others (2014). Tracking scheme dependence of simulated tropical cyclone response to idealized climate simulations. *Journal of climate*, *27*(24), 9197–9213.

Jensen, E., Ackerman, A., & Smith, J. (2007). Can overshooting convection dehydrate the tropical tropopause layer? *Journal of Geophysical Research: Atmospheres*, *112*(D11).

Jensen, E. J., Toon, O. B., Selkirk, H. B., Spinhirne, J. D., & Schoeberl, M. R. (1996). On the formation and persistence of subvisible cirrus clouds near the tropical tropopause. *Journal of Geophysical Research: Atmospheres*, *101*(D16), 21361–21375.

Johnson, R. H., & Kriete, D. C. (1982). Thermodynamic and circulation characteristics, of winter monsoon tropical mesoscale convection. *Monthly Weather Review*, *110*(12), 1898–1911.

Jonas, P. (1990). Observations of cumulus cloud entrainment. *Atmospheric research*, *25*(1-3), 105–127.

Jonker, H. J., Heus, T., & Sullivan, P. P. (2008). A refined view of vertical mass transport by cumulus convection. *Geophysical Research Letters*, *35*(7).

Jordan, C. (1960). Abnormally cold tropopause temperatures in the equatorial pacific. *Monthly Weather Review*, *88*, 151–154.

Kilroy, G., & Smith, R. K. (2013). A numerical study of rotating convection during tropical cyclogenesis. *Quarterly Journal of the Royal Meteorological Society*, *139*(674), 1255–1269.

Kim, J., Randel, W. J., & Birner, T. (2018). Convectively driven tropopause-level cooling and its influences on stratospheric moisture. *Journal of Geophysical Research: Atmospheres*, *123*(1), 590–606.

Knaff, J. A., Brown, D. P., Courtney, J., Gallina, G. M., & Beven, J. L. (2010). An evaluation of Dvorak technique–based tropical cyclone intensity estimates. *Weather and Forecasting*, *25*(5), 1362–1379.

Knaff, J. A., Longmore, S. P., DeMaria, R. T., & Molenar, D. A. (2015). Improved tropical-cyclone flight-level wind estimates using routine infrared satellite reconnaissance. *Journal of Applied Meteorology and Climatology*, *54*(2), 463–478.

Knaff, J. A., Longmore, S. P., & Molenar, D. A. (2014). An objective satellite-based tropical cyclone size climatology. *Journal of Climate*, *27*(1), 455–476.

Knaff, J. A., Slocum, C. J., & Musgrave, K. D. (2019). Quantification and exploration of diurnal oscillations in tropical cyclones. *Monthly Weather Review*, *147*(6), 2105–2121.

Knaff, J. A., Zehr, R. M., Goldberg, M. D., & Kidder, S. Q. (2000). An example of temperature structure differences in two cyclone systems derived from the Advanced Microwave Sounder Unit. *Weather and forecasting*, *15*(4), 476–483.

Komaromi, W. A., & Doyle, J. D. (2017). Tropical cyclone outflow and warm core structure as revealed by HS3 dropsonde data. *Monthly Weather Review*, *145*(4), 1339–1359.

Koteswaram, P. (1967). On the structure of hurricanes in the upper troposphere and lower stratosphere. *Mon. Wea. Rev*, *95*(8), 541–564.

Kuang, Z., & Bretherton, C. S. (2004). Convective influence on the heat balance of the tropical tropopause layer: A cloud-resolving model study. *Journal of the Atmospheric Sciences*, *61*(23), 2919–2927.

Kuo, Y.-H., Wee, T.-K., Sokolovskiy, S., Rocken, C., Schreiner, W., Hunt, D., & Anthes, R. (2004). Inversion and error estimation of GPS radio occultation data. *Journal of the Meteorological Society of Japan*, *82*(1B), 507–531.

Kursinski, E., Hajj, G., Bertiger, W., Leroy, S., et al. (1996). Initial results of radio occultation observations of Earth's atmosphere using the Global Positioning System. *Science*, *271*(5252), 1107.

Kursinski, E., Hajj, G., Schofield, J., Linfield, R., & Hardy, K. R. (1997). Observing Earth's atmosphere with radio occultation measurements using the Global Positioning System. *Journal of Geophysical Research: Atmospheres*, *102*(D19), 23429–23465.

Kursinski, E. R., Hajj, G. A., Leroy, S., & Herman, B. (2001). The GPS radio occultation technique. In *Applications of constellation observing system for meteorology, ionosphere and climate* (Vol. 1, p. 53).

Lajoie, F., & Butterworth, I. (1984). Oscillation of high-level cirrus and heavy precipitation around Australian region tropical cyclones. *Monthly weather review*, *112*(3), 535–544.

L'Ecuyer, T. S., Wood, N. B., Haladay, T., Stephens, G. L., & Stackhouse Jr, P. W. (2008). Impact of clouds on atmospheric heating based on the R04 CloudSat fluxes and heating rates data set. *Journal of Geophysical Research: Atmospheres*, *113*(D8).

Liu, C., & Zipser, E. J. (2008). Diurnal cycles of precipitation, clouds, and lightning in the tropics from 9 years of TRMM observations. *Geophysical Research Letters*, *35*(4).

Mace, G. G., Zhang, Q., Vaughan, M., Marchand, R., Stephens, G., Trepte, C., & Winker, D. (2009). A description of hydrometeor layer occurrence statistics derived from the first year of merged CloudSat and CALIPSO data. *Journal of Geophysical Research: Atmospheres*, *114*(D8).

Manganello, J. V., Hodges, K. I., Kinter III, J. L., Cash, B. A., Marx, L., Jung, T., … others (2012). Tropical cyclone climatology in a 10-km global atmospheric GCM: toward weather-resolving climate modeling. *Journal of Climate*, *25*(11), 3867–3893.

Michalke, A., & Timme, A. (1967). On the inviscid instability of certain two-dimensional vortex-type flows. *Journal of Fluid Mechanics*, *29*(4), 647–666.

Moeng, C., McWilliams, J., Rotunno, R., Sullivan, P., & Weil, J. (2004). Investigating 2d modeling of atmospheric convection in the pbl. *Journal of the atmospheric sciences*, *61*(8), 889–903.

Molinari, J., Duran, P., & Vollaro, D. (2014). Low Richardson number in the tropical cyclone outflow layer. *Journal of the Atmospheric Sciences*, *71*(9), 3164–3179.

Molod, A., Takacs, L., Suarez, M., & Bacmeister, J. (2015). Development of the GEOS-5 atmospheric general circulation model: Evolution from MERRA to MERRA2. *Geoscientific Model Development*, *8*(5), 1339.

Murakami, H. (2014). Tropical cyclones in reanalysis data sets. *Geophysical Research Letters*, *41*(6), 2133–2141.

Muramatsu, T. (1983). Diurnal variations of satellite-measured TBB areal distribution and eye diameter of mature typhoons. *Journal of the Meteorological Society of Japan. Ser. II*, *61*(1), 77–90.

Neumann, C. J. (1993). *Global guide to tropical cyclone forecasting, chapter 2*. Secretariat of the World Meteorological Organization.

Nicholls, M., & Montgomery, M. (2013). *An examination of two pathways to tropical cyclogenesis occurring in idealized simulations with a cloud-resolving numerical model* (Tech. Rep.). NAVAL POSTGRADUATE SCHOOL MONTEREY CA DEPT OF METEOROLOGY.

Ohno, T., & Satoh, M. (2015). On the warm core of a tropical cyclone formed near the tropopause. *Journal of the Atmospheric Sciences*, *72*(2), 551–571.

Paulik, L. C., & Birner, T. (2012). Quantifying the deep convective temperature signal within the tropical tropopause layer (ttl). *Atmospheric Chemistry and Physics*, *12*(24), 12183–12195.

Persing, J., Montgomery, M. T., McWilliams, J., & Smith, R. K. (2013). Asymmetric and axisymmetric dynamics of tropical cyclones. *Atmos. Chem. Phys*, *13*(12), 299–12.

Randel, W. J., Wu, F., & Rivera Ríos, W. (2003). Thermal variability of the tropical tropopause region derived from GPS/MET observations. *Journal of Geophysical Research: Atmospheres*, *108*(D1), ACL–7.

Ray, E. A., & Rosenlof, K. H. (2007). Hydration of the upper troposphere by tropical cyclones. *Journal of Geophysical Research: Atmospheres*, *112*(D12).

Reasor, P. D., Montgomery, M. T., & Grasso, L. D. (2004). A new look at the problem of tropical cyclones in vertical shear flow: Vortex resiliency. *Journal of the Atmospheric Sciences*, *61*(1), 3–22.

Reid, G. C., & Gage, K. S. (1985). Interannual variations in the height of the tropical tropopause. *Journal of Geophysical Research: Atmospheres*, *90*(D3), 5629–5635.

Reynolds, R. W., & Smith, T. M. (1995). A high-resolution global sea surface temperature climatology. *Journal of Climate*, *8*(6), 1571–1583.

Rivoire, L., Birner, T., & Knaff, J. A. (2016). Evolution of the upper-level thermal structure in tropical cyclones. *Geophysical Research Letters*, *43*(19), 10–530.

Rivoire, L., Birner, T., Knaff, J. A., & Tourville, N. D. (2020). Quantifying the radiative impact of clouds on tropopause layer cooling in tropical cyclones. *Journal of Climate*, *in review*.

Rogers, R., Reasor, P., & Lorsolo, S. (2013). Airborne Doppler observations of the inner-core structural differences between intensifying and steady-state tropical cyclones. *Monthly Weather Review*, *141*(9), 2970–2991.

Romps, D. M. (2010). A direct measure of entrainment. *Journal of the Atmospheric Sciences*, *67*(6), 1908–1927.

Romps, D. M., & Kuang, Z. (2009). Overshooting convection in tropical cyclones. *Geophysical*

Research Letters, *36*(9).

Rossow, W. B., & Schiffer, R. A. (1999). Advances in understanding clouds from isccp. *Bulletin of the American Meteorological Society*, *80*(11), 2261–2288.

Rotunno, R. (1979). A study in tornado-like vortex dynamics. *Journal of the Atmospheric Sciences*, *36*(1), 140–155.

Rotunno, R., & Emanuel, K. A. (1987). An air–sea interaction theory for tropical cyclones. Part II: Evolutionary study using a nonhydrostatic axisymmetric numerical model. *Journal of the Atmospheric Sciences*, *44*(3), 542–561.

Rotunno, R., Klemp, J. B., & Weisman, M. L. (1988). A theory for strong, long-lived squall lines. *Journal of the Atmospheric Sciences*, *45*(3), 463–485.

Sampson, C. R., & Schrader, A. J. (2000). The automated tropical cyclone forecasting system (version 3.2). *Bulletin of the American Meteorological Society*, *81*(6), 1231.

Sassen, K., & Wang, Z. (2008). Classifying clouds around the globe with the CloudSat radar: 1 year of results. *Geophysical research letters*, *35*(4).

Sassen, K., & Wang, Z. (2012). The clouds of the middle troposphere: Composition, radiative impact, and global distribution. *Surveys in Geophysics*, *33*(3-4), 677–691.

Sassen, K., Wang, Z., & Liu, D. (2008). Global distribution of cirrus clouds from CloudSat/Cloud-Aerosol lidar and infrared pathfinder satellite observations (CALIPSO) measurements. *Journal of Geophysical Research: Atmospheres*, *113*(D8).

Sassen, K., Wang, Z., & Liu, D. (2009). Cirrus clouds and deep convection in the tropics: Insights from CALIPSO and CloudSat. *Journal of Geophysical Research: Atmospheres*, *114*(D4).

Schubert, W. H., & McNoldy, B. D. (2010). Application of the concepts of Rossby length and Rossby depth to tropical cyclone dynamics. *Journal of Advances in Modeling Earth Systems*, *2*(3).

Schubert, W. H., Montgomery, M. T., Taft, R. K., Guinn, T. A., Fulton, S. R., Kossin, J. P., & Edwards, J. P. (1999). Polygonal eyewalls, asymmetric eye contraction, and potential vorticity mixing in hurricanes. *Journal of the atmospheric sciences*, *56*(9), 1197–1223.

Seidel, D. J., Ross, R., Angell, J. K., & Reid, G. C. (2001). Climatological characteristics of the tropical tropopause as revealed by radiosondes. *Journal of Geophysical Research*, *106*(D8), 7857–7878.

Shapiro, L. J., & Willoughby, H. E. (1982). The response of balanced hurricanes to local sources of heat and momentum. *Journal of the Atmospheric Sciences*, *39*(2), 378–394.

Sherwood, S. C., Minnis, P., & McGill, M. (2004). Deep convective cloud-top heights and their thermodynamic control during crystal-face. *Journal of Geophysical Research: Atmospheres*, *109*(D20).

Shu, H.-L., Zhang, Q.-H., & Xu, B. (2013). Diurnal variation of tropical cyclone rainfall in the western North Pacific in 2008–2010. *Atmospheric and Oceanic Science Letters*, *6*(2), 103–108.

Son, S.-W., Tandon, N. F., & Polvani, L. M. (2011). The fine-scale structure of the global tropopause derived from COSMIC GPS radio occultation measurements. *Journal of Geophysical Research: Atmospheres*, *116*(D20).

Stephens, G. L., Gabriel, P. M., & Partain, P. T. (2001). Parameterization of atmospheric radiative transfer. part I: Validity of simple models. *Journal of the Atmospheric Sciences*, *58*(22), 3391–3409.

Stephens, G. L., Vane, D. G., Boain, R. J., Mace, G. G., Sassen, K., Wang, Z., … others (2002). The CloudSat mission and the A-Train: A new dimension of space-based observations of clouds and precipitation. *Bulletin of the American Meteorological Society*, *83*(12), 1771–1790.

Steranka, J., Rodgers, E. B., & Gentry, R. C. (1984). The diurnal variation of Atlantic ocean tropical cyclone cloud distribution inferred from geostationary satellite infrared measurements. *Monthly Weather Review*, *112*(11), 2338–2344.

Steranka, J., Rodgers, E. B., & Gentry, R. C. (1986). The relationship between satellite measured convective bursts and tropical cyclone intensification. *Monthly weather review*, *114*(8), 1539–1546.

Stern, D. P., & Nolan, D. S. (2009). Reexamining the vertical structure of tangential winds in tropical cyclones: Observations and theory. *Journal of the Atmospheric Sciences*, *66*(12), 3579–3600.

Takahashi, H., & Luo, Z. J. (2014). Characterizing tropical overshooting deep convection from joint analysis of CloudSat and geostationary satellite observations. *Journal of Geophysical Research: Atmospheres*, *119*(1), 112–121.

Thuburn, J., & Craig, G. C. (2002). On the temperature structure of the tropical substratosphere. *Journal of Geophysical Research: Atmospheres*, *107*(D2), ACL–10.

Torn, R. D., & Snyder, C. (2012). Uncertainty of tropical cyclone best-track information. *Weather and Forecasting*, *27*(3), 715–729.

Tourville, N., Stephens, G., DeMaria, M., & Vane, D. (2015). Remote sensing of tropical cyclones: Observations from CloudSat and A-Train profilers. *Bulletin of the American Meteorological Society*, *96*(4), 609–622.

Townshend, J. R. (1992). Improved global data for land applications: A proposal for a new high resolution data set. report of the land cover working group of igbp-dis. *Global Change Report (Sweden)*.

Trepte, Q. Z., Minnis, P., Trepte, C., Sun-Mack, S., & Brown, R. (2010). Improved cloud detection in CERES edition 3 algorithm and comparison with the CALIPSO vertical feature mask. In *Proc. 13th conf. on atmospheric radiation and cloud physics.*

Vitart, F., Anderson, J., & Stern, W. (1997). Simulation of interannual variability of tropical storm frequency in an ensemble of GCM integrations. *Journal of Climate*, *10*(4), 745–760.

Walsh, K., Fiorino, M., Landsea, C., & McInnes, K. (2007). Objectively determined resolution-dependent threshold criteria for the detection of tropical cyclones in climate models and reanalyses. *Journal of climate*, *20*(10), 2307–2314.

Weatherford, C. L., & Gray, W. M. (1988). Typhoon structure as revealed by aircraft reconnaissance. Part II: Structural variability. *Monthly Weather Review*, *116*(5), 1044–1056.

Willoughby, H. (1979). Forced secondary circulations in hurricanes. *Journal of Geophysical Research: Oceans*, *84*(C6), 3173–3183.

Willoughby, H. (1998). Tropical cyclone eye thermodynamics. *Monthly Weather Review*, *126*(12), 3053–3067.

Yang, B., Wang, Y., & Wang, B. (2007). The effect of internally generated inner-core asymmetries on tropical cyclone potential intensity. *Journal of the atmospheric sciences*, *64*(4), 1165–1188.

Yang, Q., Fu, Q., & Hu, Y. (2010). Radiative impacts of clouds in the tropical tropopause layer. *Journal of Geophysical Research: Atmospheres*, *115*(D4).

Zagrodnik, J. P., & Jiang, H. (2014). Rainfall, convection, and latent heating distributions in rapidly intensifying tropical cyclones. *Journal of the Atmospheric Sciences*, *71*(8), 2789–2809.

Zhang, D.-L., & Chen, H. (2012). Importance of the upper-level warm core in the rapid intensification of a tropical cyclone. *Geophysical Research Letters*, *39*(2).

Zhang, Z., Yang, P., Kattawar, G., Riedi, J., Labonnote, L., Baum, B., … Huang, H.-L. (2009). Influence of ice particle model on satellite ice cloud retrieval: lessons learned from MODIS and POLDER cloud product comparison. *Atmospheric Chemistry and Physics*, *9*(18), 7115–7129.